Numerical modelling of non-destructive testing of buried waveguides

Matthieu Gallezot

To cite this version:

Matthieu Gallezot. Numerical modelling of non-destructive testing of buried waveguides. Acoustics [physics.class-ph]. École centrale de Nantes, 2018. English. NNT : 2018ECDN0040 . tel-01963534

HAL Id: tel-01963534

https://theses.hal.science/tel-01963534v1

Submitted on 21 Dec 2018

THESE DE DOCTORAT DE

L'ÉCOLE CENTRALE DE NANTES
COMUE UNIVERSITE BRETAGNE LOIRE

ECOLE DOCTORALE N° 602
Sciences pour l'Ingénieur
Spécialité : *Acoustique*

Par
Matthieu GALLEZOT

Simulation numérique du contrôle non-destructif des guides d'ondes enfouis

Thèse soutenue publiquement à Nantes, le 22 novembre 2018
Unité de recherche : Institut Français des Sciences et Technologies des Transports, de l'Aménagement et des Réseaux - Géotechnique, environnement, risques naturels et sciences de la terre – Géophysique et Evaluation Non Destructive

Rapporteurs avant soutenance :

Anne-Sophie Bonnet-Ben Dhia	Directrice de Recherche au Centre National de la Recherche Scientifique, Ecole Nationale Supérieure des Techniques Avancées ParisTech
Mohamed Ichchou	Professeur des Universités, Ecole Centrale de Lyon

Composition du Jury :

Président :	Marc Deschamps	Directeur de Recherche au Centre National de la Recherche Scientifique, Université de Bordeaux
Examinateurs :	Patrice Cartraud	Professeur des Universités, Ecole Centrale de Nantes
Directeur de thèse :	Laurent Laguerre	Directeur de Recherche, Institut Français des Sciences et Technologies des Transports, de l'Aménagement et des Réseaux
Encadrant :	Fabien Treyssède	Chargé de Recherche, Institut Français des Sciences et Technologies des Transports, de l'Aménagement et des Réseaux

Invité

Vincent Pagneux	Directeur de Recherche au Centre National de la Recherche Scientifique, Université du Maine

Remerciements

Je tiens à remercier en premier lieu Fabien et Laurent pour leur accompagnement bienveillant, leur disponibilité, leur saine exigence de rigueur et pour tous les moments d'échanges et de réflexions (non–)scientifiques. Le bon déroulement de cette thèse leur doit beaucoup.

J'aimerais également remercier Marc Deschamps, Éric Ducasse et Samuel Rodriguez de l'Institut de Mécanique et d'Ingénierie (I2M) de Bordeaux pour les échanges fructueux que nous avons eus autour de l'imagerie topologique. Marc Deschamps a également composé, avec Christophe Hazard, le comité de suivi de ma thèse. Cela s'est toujours traduit par des journées de travail dynamiques et enrichissantes. Je salue également Simon Félix et Arnaud Recoquillay pour l'intérêt qu'ils ont porté à mon travail, leur sympathie et les discussions que nous avons eues en différentes occasions.

Je suis extrêmement reconnaissant envers l'ensemble des membres du jury pour l'attention donnée à mon travail et aux questions qui y sont liées : Patrice Cartraud, Marc Deschamps, Vincent Pagneux ainsi que les rapporteur·e·s de ce (dense) manuscrit, Anne–Sophie Bonnet–Ben Dhia et Mohamed Ichchou.

J'ai eu le plaisir d'enseigner deux années durant au sein du département Matériaux de Polytech'Nantes. Cette expérience fut très enrichissante et formatrice. Je remercie Guy Louarn, directeur du département, pour sa confiance et sa disponibilité ; Stéphane Cuenot, Jérémy Freixas, Thomas Lepetit pour les nombreuses heures partagées de travaux pratiques ; Martine Bleis pour son efficace support administratif ; et l'ensemble des étudiant·e·s pour leur indispensable présence.

Je remercie également Odile Abraham, directrice du laboratoire GeoEND à l'Ifsttar, pour son accueil au sein de cette structure sans laquelle cette thèse n'aurait pas été possible. Une pensée spéciale est dédiée à l'ensemble des doctorant·e·s pour tous les moments que nous avons passés ensemble, notamment à Guangzhi pour le partage patient du bureau et à Céline, à l'initiative de la construction partagée d'un jeu de Mölkky qui a dynamisé nos pauses café.

Enfin dans un tout autre registre, je salue tou·te·s celles et ceux avec qui j'ai partagé des instants de vie au cours de ces trois années, que ce soit à la maison du 19 et dans son quartier, au cours de joyeuses sessions irlandaises de par le monde, à la NoE et dans ses environs légumiers et arboricoles, à Nantes, à Paris, dans la rue, dans le bocage et ailleurs. Beaucoup ne sont pas scientifiques, et j'ai bien conscience que ce manuscrit ne trouve pas chez elles une « expression normale dans le langage et la pensée ». J'espère que, tôt ou tard, des discussions animées viendront réparer ce manquement, pour, ainsi que nous y invite Hannah Arendt, « penser ce que nous faisons ».

Contents

Résumé étendu en français

Contexte

Cette thèse porte sur le développement de modèles numériques et d'une méthode d'imagerie pour le contrôle non destructif (CND) dans le génie civil. Nous considérons des structures allongées et partiellement ou totalement enfouies dans un milieu solide (roche, ciment...). Les câbles de pont ou les tirants d'ancrage sont des exemples typiques. Ces structures peuvent être le support d'une propagation d'ondes guidées. Néanmoins, l'utilisation de ces ondes pour le CND est complexe. Leur nature multimodale et dispersive complique l'interprétation des résultats. De plus, la distance d'auscultation est limitée par le rayonnement des ondes dans le milieu environnant (atténuation par fuites). Le développement de modèles numériques permet alors de mieux comprendre ces phénomènes, et de déterminer les conditions idéales de propagation pour le CND.

Constituées d'un cœur (la structure guidante) enfoui dans un milieu solide, ces structures peuvent être modélisées comme des guides d'ondes élastiques *ouverts*, c'est-à-dire dont la direction transverse à l'axe du guide est non bornée. Comparativement aux guides d'ondes dans le vide (les guides d'ondes *fermés*, de section bornée), la physique sous-jacente est profondément modifiée. Dans un guide fermé, les modes sont séparés entre modes propagatifs et modes non propagatifs (évanescents et inhomogènes). Dans un guide ouvert, les modes sont divisés en trois groupes : les modes piégés, les modes de rayonnement et les modes à fuite.

Les modes piégés se propagent suivant l'axe du guide, sans perte par fuite, et décroissent exponentiellement le long de la direction transverse. Ces modes sont donc confinés dans le cœur du guide ou à l'interface avec le milieu environnant. Leur existence dépend du contraste entre les matériaux constitutifs du guide [1]. Les modes de rayonnement sont des ondes stationnaires dans la direction transverse, qui peuvent être propagatives ou évanescentes suivant l'axe du guide [2, 3]. Enfin, les modes à fuite se propagent avec des pertes dans le milieu environnant. Ils décroissent donc exponentiellement le long de l'axe du guide. L'étude de ces modes fournit des informations indispensables pour le CND des guides ouverts, telles que l'atténuation et la vitesse de propagation axiales des paquets d'ondes [4]. Néanmoins, les modes à fuite ont la particularité de croître à l'infini le long de la direction transverse [5–7], ce qui pose des difficultés d'un point de vue mathématique.

Le recours à des méthodes numériques permet de calculer les modes de guides de géométrie quelconque, dont notamment des guides d'ondes 3Ds à section 2D non canonique. Pour les guides ouverts, la difficulté réside dans l'aspect non borné du problème. Une solution (parmi d'autres) — proposée d'abord pour les guides ouverts scalaires [8], puis développée pour le CND de guides ouverts élastiques (vectoriels) dans une thèse précédente à l'Ifsttar [9] — consiste en l'utilisation d'une couche parfaitement adaptée (PML) d'épaisseur finie dans la direction transverse afin d'atténuer la croissance des modes à fuite. La section du guide (orthogonale à la direction de propagation des ondes), désormais bornée, est alors discrétisée par éléments finis, tandis que la propagation des ondes est décrite analytiquement (méthode de type SAFE). Les modes sont finalement obtenus en résolvant un problème aux valeurs propres quadratiques.

Avec une PML, trois types de modes peuvent être obtenus : les modes piégés, les modes à fuite (dont la croissance transverse a été atténuée dans la PML) et les modes de PML (ou modes de Berenger). Ces derniers sont non intrinsèques à la physique : ils oscillent principalement dans la PML et dépendent de ses paramètres. Ils doivent être filtrés afin d'obtenir les courbes de dispersion des modes utiles au CND, c'est-à-dire celles des modes piégés et des modes à fuite.

Ayant calculé les modes, l'objectif principal de cette thèse est de construire par superposition modale des solutions aux problèmes d'émission, de propagation et de diffraction des modes. Pour cela, il est nécessaire de clarifier l'appartenance des modes à fuite à la base modale, ainsi que de déterminer l'influence de la contribution des modes de PML sur les solutions obtenues. Dans un premier temps, nous justifions que les trois types de modes calculés avec une PML forment une base modale (Chapitre 1). Puis, nous nous intéressons au calcul de la réponse forcée d'un guide ouvert élastique (Chapitre 2). Une méthode numérique est développée et validée. Le rôle de chaque type de mode est clarifié. Ensuite, le champ diffracté par un défaut est obtenu par une méthode dite hybride, couplant éléments finis et représentation modale (Chapitre 3). L'analyse du rôle de chaque type de mode est également poursuivie.

Enfin, dans le cadre du développement de nouveaux outils pour le CND, ces modèles sont utilisés pour tester une méthode d'imagerie appliquée aux guides d'ondes élastiques fermés ou ouverts (Chapitre 4). L'objectif est de localiser et de caractériser un ou plusieurs défauts dans le guide, à partir d'une mesure du champ réfléchi.

Contribution des modes à fuite à l'analyse modale de problèmes non bornés avec PML (Chapitre 1)

L'analyse modale permet une étude physique précise des ondes qui se propagent dans un guide. Elle consiste en une décomposition des solutions sur les modes du guide. Dans le cas des guides ouverts, la base modale est théoriquement bien connue dans la littérature en l'absence de PML. En revanche, si l'on modélise les guides ouverts avec une PML, il est nécessaire de mieux comprendre la contribution de chaque type de modes dans la base obtenue. Particulièrement, l'inclusion des modes à fuite et le rôle des modes de PML méritent d'être clarifiés. L'objectif est de justifier l'utilisation de ces modes pour le calcul numérique de la réponse forcée ou du champ diffracté dans les guides ouverts.

Théoriquement, la réponse forcée d'un guide ouvert (sans PML) peut être décomposée sur les modes piégés et de rayonnement. Le champ de déplacement s'écrit alors symboliquement [2, 3, 10] :

$$u(\mathbf{r},\omega) = \sum \text{piégés} + \int \text{rayonnement.} \tag{1}$$

Nous rappelons l'origine de cette solution pour l'équation de Helmholtz avec terme source. Dans le domaine des nombres d'ondes, la solution au problème est une fonction multivaluée dépendant du nombre d'onde transverse dans le milieu environnant. En effet, le nombre d'onde transverse est la racine carrée d'un nombre complexe, définie sur deux feuillets de Riemann séparés par une branche de coupure. Celle-ci sépare le feuillet de Riemann propre (auquel appartiennent les modes piégés, bornés transversalement) du feuillet de Riemann impropre (auquel appartiennent les modes à fuite, non bornés transversalement). La transformée de Fourier inverse est intégrée sur le feuillet de Riemann propre ce qui, après application du théorème des résidus et du lemme de Jordan, fait apparaître la somme discrète de modes piégés et l'intégrale de modes de rayonnement (voir Eq. (1)). Cette intégrale représente la contribution de la branche de coupure. Ce continuum de rayonnement, propre au caractère non borné du problème, est difficile à manipuler mathématiquement et physiquement. Il peut être approximé par une somme discrète sur les modes à fuite, par exemple en utilisant la méthode du col [10, 11]. Cette approximation n'est valide que dans une zone restreinte, proche du cœur du guide. Pour le problème élastodynamique, deux continua apparaissent [3, 5] car il y a alors deux nombres d'ondes transverses.

Le milieu environnant est ensuite modifié par l'application d'une PML, débutant à une distance transverse $r = d$ de l'axe de guide (axe en $r = 0$, z étant la direction de l'axe et r la direction transverse). Cette transformation se résume à un prolongement analytique des équations du problème dans l'espace de la coordonnée transverse $\tilde{r}(r)$, à valeurs complexes. Cette dernière est définie par :

$$\tilde{r}(r) = \int_0^r \gamma(\xi)\mathrm{d}\xi. \tag{2}$$

La fonction $\gamma(r)$ est une fonction à valeurs complexes dans la PML ($r > d$) permettant d'atténuer les ondes sortantes, telle que $\arg\gamma \in [0; \pi/2[$. Cette fonction caractérise le profil d'atténuation de la PML.

Nous montrons alors que la transformation du milieu environnant par une PML d'épaisseur infinie et de profil d'atténuation constant modifie la définition des feuillets de Riemman, du fait de la rotation d'angle $-\arg\gamma$ des branches de coupure. Cette rotation permet d'avoir accès à une partie du feuillet de Riemann impropre initial, contenant les modes à fuite. Ainsi, avec une PML d'épaisseur infinie, une somme discrète de modes à fuite apparaît naturellement dans la base modale. D'autre part, les modes piégés ne sont pas modifiés par l'introduction d'une PML. Par conséquent, on peut montrer que la réponse forcée d'un guide ouvert avec une PML infinie s'écrit symboliquement :

$$u(\mathbf{r}, \omega) = \sum \text{piégés} + \sum \text{fuites} + \int \text{rayonnement dans la PML.} \tag{3}$$

Cette solution est valide en dehors de la PML ($r < d$), c'est-à-dire principalement dans le cœur du guide.

Du point de vue de la modélisation numérique, il est nécessaire de tronquer la PML à une épaisseur finie ($d < r < h$) — voir Chapitre 2. Les continua de rayonnement liés aux branches de coupures sont alors transformés en sommes discrètes de modes de PML.

Une approche modale avec PML de la réponse forcée des guides d'ondes élastiques ouverts (Chapitre 2)

Suite au travail théorique précédent, nous passons au calcul numérique, par superposition modale, de la réponse forcée d'un guide élastique ouvert de section arbitraire, avec PML.

Afin de garantir l'unicité des résultats, une étape préalable importante consiste à obtenir une relation d'orthogonalité. Par ailleurs, bien qu'apparaissant théoriquement dans la base modale, les modes de PML obtenus numériquement sont non intrinsèques à la physique car ils dépendent totalement des paramètres de la PML ainsi que de la condition limite en fin de PML (condition de Dirichlet dans cette thèse). Il apparaît donc nécessaire d'étudier numériquement leur utilité, ainsi que leur influence sur la précision des décompositions modales numériques. Le rôle des modes à fuite nécessite également d'être clarifié.

Rappelons tout d'abord qu'en considérant une dépendance du champ de la forme $e^{\mathrm{j}(kz-\omega t)}$ (k : nombre d'onde axial suivant z ; ω : pulsation), la forme variationnelle des équations de l'élastodynamique (modifiées par la PML d'après l'Eq. (2)) peut être écrite sur la section du guide (méthode SAFE [12, 13]). Une discrétisation par éléments finis permet alors d'obtenir un système aux valeurs propres quadratiques du type suivant :

$$\left(\mathbf{K}_1 - \omega^2\mathbf{M} + \mathrm{j}k(\mathbf{K}_2 - \mathbf{K}_2^{\mathrm{T}}) + k^2\mathbf{K}_3\right)\hat{\mathbf{U}} = \hat{\mathbf{0}}. \tag{4}$$

Les matrices $\mathbf{K}_1$, $\mathbf{K}_3$ et $\mathbf{M}$ sont symétriques à valeurs complexes. $\hat{\mathbf{U}}(k,\omega)$ est le vecteur de déplacement à chaque degré de liberté (ddl). L'Eq. (4) est linéarisée et résolue pour chaque pulsation ω. Le spectre obtenu est composé de paires de modes opposés en valeurs propres, notées $(k_m, \mathbf{U}_m)$ and $(k_{-m}, \mathbf{U}_{-m})$, $(m = 1, \ldots, M)$, avec $k_{-m} = -k_m$, représentant M modes se propageant suivant les z positifs et M modes se propageant suivant les z négatifs.

En partant du problème linéarisé et en utilisant les propriétés des matrices, des vecteurs propres à gauche et à droite, nous montrons que la relation

$$\frac{\mathrm{j}\omega}{4}(\mathbf{U}_m^{\mathrm{T}}\mathbf{F}_{-n} - \mathbf{U}_{-n}^{\mathrm{T}}\mathbf{F}_m) = Q_{m,-m}\delta_{mn}, \tag{5}$$

est une relation générale de biorthogonalité sur l'ensemble de la section (c'est-à-dire incluant la PML). Dans l'Eq. (5), les vecteurs $\mathbf{F}_{\pm m}$ représentent les forces modales, directement obtenues à partir des matrices impliquées dans l'Eq. (4) et des vecteurs propres. Cette relation de biorthogonalité est valable quelle que soit la nature des modes (piégés, à fuite et de PML). Elle reste aussi valable pour des matériaux viscoélastiques ou anisotropes, et des guides d'ondes de géométrie quelconque.

À partir de l'Eq. (4), en incluant un terme source $\hat{\mathbf{F}}(k,\omega)$ à droite, l'application de la relation d'orthogonalité (5) et du théorème des résidus permet d'obtenir le champ se propageant dans le guide, tel que (ici pour une propagation suivant les z positifs) :

$$\mathbf{U}(z,\omega) = \sum_{m=1}^{M} \mathbf{E}_m\hat{\mathbf{F}}(k_m)\mathrm{e}^{\mathrm{j}k_m z}, \tag{6}$$

où $\mathbf{E}_m$ définit l'excitabilité modale. Cette grandeur représente l'amplitude du déplacement du mode m au ddl i pour une excitation unitaire au ddl j. Il s'agit d'une caractéristique importante du guide pour le CND. En effet, sa connaissance permet l'optimisation du type de capteurs à utiliser et de leur emplacement. Finalement, la réponse forcée temporelle est obtenue par transformée de Fourier inverse en temps de l'Eq. (6).

Afin de valider la méthode et de clarifier le rôle des modes de PML, le cas d'un milieu homogène excité par une force ponctuelle est d'abord étudié. Un milieu homogène peut être vu comme un cas limite de guide d'onde ouvert, constitué d'une seule couche donc sans contraste d'impédance. Dans ce cas, il n'y a ni modes piégés ni modes à fuite, mais seulement des modes de PML. La solution obtenue est comparée à une solution exacte temporelle de la littérature [14], en faisant varier deux paramètres : le nombre de modes retenus dans la décomposition modale, ainsi que l'épaisseur complexe de la PML. Les résultats montrent qu'une bonne précision peut être obtenue dans un intervalle restreint de distances à la source, sous réserve que la PML soit correctement paramétrée. Cela permet de valider la méthode proposée. D'autre part, cela démontre en particulier qu'il est possible de reconstruire la décroissance géométrique des ondes de volume à partir de modes de PML, qui décroissent exponentiellement par nature. Pour cela, il est notamment nécessaire d'avoir une épaisseur complexe de la PML suffisante (ceci permet de discrétiser suffisamment finement le continuum théorique). Ces résultats confirment les développements mathématiques de la Ref. [15] obtenus dans le cas d'un guide d'onde scalaire.

Plus proche d'une application réelle, le cas d'un guide circulaire en acier enfoui dans du ciment est ensuite considéré, également excité par une source ponctuelle. Très loin de la source, les résultats obtenus montrent que la contribution des modes de PML à la réponse forcée est prédominante. À cette distance, la majeure partie de l'énergie a fui du cœur du guide vers le milieu environnant. Le comportement du champ devient alors proche de celui des ondes de volume (sa décroissance est géométrique). Ce phénomène est appelé diffraction à long terme. Il faut noter que des méthodes alternatives à la PML, comme par exemple l'usage de couches absorbantes viscoélastiques, ne permettent pas de reconstituer ce phénomène [16].

Cependant, plus proche de la source, la réponse forcée est dominée par le comportement des modes à fuite (à décroissance exponentielle). Dans cet intervalle de distance (le plus intéressant pour le CND), les modes à fuite sont suffisants pour obtenir une bonne approximation de la solution et les modes de PML peuvent être négligés. Ceci permet de réduire l'épaisseur complexe de la PML et donc le coût du calcul.

Ceci est particulièrement intéressant pour le calcul de la réponse forcée pour de hautes fréquences ou pour des guides 3Ds (section 2D arbitraire). En effet, il est connu qu'à certaines hautes fréquences, l'énergie reste concentrée au cœur du guide, ce qui permet de réduire l'atténuation par fuites [17]. Dans la configuration étudiée, le mode à fuite longitudinal d'ordre 12 (noté L(0,12)) est le moins atténué. Ce mode est très attractif pour le CND puisqu'il peut se propager sur de plus grandes distances que les autres. La capacité du modèle proposé à obtenir la réponse forcée dans ces gammes de fréquences est alors démontrée à travers deux cas, une barre circulaire (guide 2D) et une barre carrée (guide 3D) enfouies, résolus par superposition sur les modes à fuite uniquement.

Modélisation numérique de la diffraction des ondes par des inhomogénéités locales dans les guides d'ondes élastiques ouverts (Chapitre 3)

Dans ce chapitre, nous développons une méthode numérique pour obtenir le champ diffracté par un défaut. D'un point de vue CND, cette méthode vise à caractériser la sensibilité des modes piégés ou à fuite pour un défaut donné. Nous cherchons donc à obtenir les coefficients de réflexion et de transmission des modes, incluant généralement des conversions modales au niveau du défaut.

L'étendue du défaut est limitée à une zone localisée du guide. Le principe utilisé est identique à celui des méthodes dites hybrides dans les guides d'ondes fermés (aussi appelées

FE-SAFE [18, 19]). Il s'agit de décrire un petit volume entourant le défaut par un modèle élément fini. Ce dernier est ensuite couplé à une représentation modale du champ se propageant dans les parties saines du guide, ce qui conduit à des conditions aux limites transparentes. Dans la lignée du travail précédemment exposé, nous nous basons sur une formulation modale du problème. Nous nous intéressons toujours particulièrement à l'influence des modes de PML sur la solution, cette dernière étant cette fois ci obtenue en champ proche (et non plus en champ lointain comme en réponse forcée). Le sens physique de la relation de biorthogonalité (5) est également discuté.

La méthode hybride obtenue combine trois équations (voir les Eqs. (7), (8) et (9) données ci-après). D'une part, il y a le système aux éléments finis du volume entourant le défaut, classiquement écrit :

$$\delta\mathbf{U}^{\mathrm{T}}(\mathbf{K}-\omega^2\mathbf{M})\mathbf{U}=\delta\mathbf{U}^{\mathrm{T}}\mathbf{F}. \tag{7}$$

D'autre part, des décompositions modales des champs de déplacements et de forces sont effectuées sur les frontières Σ du volume correspondant aux sections des guides (sains) connectés de part et d'autre du volume élément fini, telles que :

$$\mathbf{U}_\Sigma=\sum_{n=1}^{N}\alpha_{-n}\mathbf{U}_{-n}+\sum_{n=1}^{N}\alpha_n\mathbf{U}_n, \tag{8}$$

$$\mathbf{F}_\Sigma=\sum_{n=1}^{N}\alpha_{-n}\mathbf{F}_{-n}+\sum_{n=1}^{N}\alpha_n\mathbf{F}_n. \tag{9}$$

Les $\alpha_{\pm n}$ sont les coefficients modaux des modes incidents (connus, repérés par l'indice $-$) ou des modes diffractés (inconnus, repérés par l'indice $+$). Les déplacements et les forces modales sont obtenus par résolution du système (4). Le couplage des équations (7), (8), (9) mène au système suivant :

$$\mathbf{G}_{u_+}^{\mathrm{T}}(\mathbf{D}\mathbf{G}_{u_+}-\mathbf{G}_{f_+})\mathbf{U}_+=\mathbf{G}_{u_+}^{\mathrm{T}}(\mathbf{G}_{f_-}-\mathbf{D}\mathbf{G}_{u_-})\mathbf{U}_-. \tag{10}$$

Les matrices $\mathbf{G}$ contiennent les bases modales en déplacement (u) et en force (f) des modes incidents ou diffractés. $\mathbf{D}=\mathbf{K}-\omega^2\mathbf{M}$ est la matrice de raideur dynamique. $\mathbf{U}_-$ regroupe les grandeurs connues : le vecteur des forces volumiques internes et les coefficients des modes incidents. Le vecteur $\mathbf{U}_+$ contient les grandeurs inconnues : les déplacements aux ddls internes du volume élément fini et les coefficients des modes diffractés. Ce vecteur est obtenu en inversant le système linéaire matriciel (10) à chaque pulsation ω.

La méthode proposée est validée par comparaison avec l'un des rares cas déjà traités dans la littérature, à la fois par une approche élément fini et par une approche de type mode-matching. Il s'agit de la réflexion du mode longitudinal L(0,1) à la jonction entre un guide fermé et un guide ouvert [7]. Un bon accord est obtenu entre la méthode hybride et les résultats de référence. De nouveaux résultats sont également présentés pour la transmission du mode guidé L(0,1) vers le mode à fuite fondamental. Dans ce cas test, la contribution des modes de PML à la solution est faible et peut donc être négligée. Cette approximation engendrerait nécessairement des erreurs en champ lointain, dans la zone dite de diffraction à long terme, comme montré dans l'étude sur la réponse forcée (Chapitre 2).

La méthode est ensuite appliquée à l'étude de la diffraction par une entaille axisymétrique du mode à fuite L(0,1) (basse fréquence, très atténué) et du mode à fuite L(0,12) (haute fréquence, peu atténué). Les résultats obtenus en basse fréquence concordent avec un cas proche de la littérature [17], ce qui confirme la validité de la méthode proposée. Par ailleurs, nos résultats confirment que le mode L(0,12) se propage plus loin que les autres, et montrent que son coefficient de réflexion est élevé et qu'il est peu converti vers d'autres modes. Ceci corrobore l'intérêt des modes hautes fréquences pour le CND, notamment pour des défauts profonds.

Dans les guides ouverts, l'analyse des résultats s'avère plus difficile à certaines fréquences bien particulières auxquelles les modes interagissent entre eux, et pour lesquelles un phénomène de croisement des courbes de vitesse de phase apparaît. Ces observations illustrent la non-orthogonalité des puissances modales, démontrée à partir de la relation (5). En effet, la puissance totale dans un guide ouvert est la somme des puissances individuelles de chaque mode et des puissances croisées. Rappelons que dans le cas d'un guide fermé élastique (sans perte), les puissances croisées sont nulles. Dans le cas des guides ouverts (ou des guides fermés viscoélastiques), nous montrons que la puissance modale croisée, c'est-à-dire la puissance résultant du couplage de deux modes, peut être significative. Les coefficients modaux individuels sont alors susceptibles d'évoluer de manière contre-intuitive.

Dans ce cas test, nous montrons également que les modes de PML peuvent apporter une contribution non négligeable à la solution lorsque la distance entre le défaut et les frontières transparentes est réduite. Autrement dit, dans certains cas, les modes de PML ont une contribution importante à la solution en champ proche. Par conséquent en pratique, la validité des résultats obtenus avec la méthode hybride doit être soigneusement vérifiée en variant la distance entre le défaut et les frontières transparentes, ainsi que le nombre de modes retenus dans les décompositions modales aux frontières. Ceci est particulièrement critique pour les problèmes 3Ds, pour lesquels il est nécessaire de réduire le nombre de modes à calculer afin de maintenir un coût de calcul raisonnable. Les frontières transparentes doivent alors être positionnées suffisamment loin du défaut pour permettre de négliger les modes de PML (et donc éviter leur calcul). Pour clore ce chapitre, le cas d'un problème 3D est illustré dans une barre cylindrique par la diffraction du mode L(0,1) à fuite (basse fréquence) par un défaut non axisymétrique.

Imagerie par gradient de guides d'ondes (Chapitre 4)

La dernière partie de cette thèse s'inscrit dans le cadre des problèmes inverses en élastodynamique. L'objectif est de localiser et de caractériser un ou plusieurs défauts présents dans un guide ouvert à partir d'une mesure du champ diffracté. Ici, les informations recherchées sont la distance du défaut à la source, ainsi que son emplacement dans la section du guide. La forme exacte du défaut ou sa matière ne sont pas recherchées. Parmi les nombreuses méthodes existantes, nous choisissons d'utiliser la méthode de l'imagerie dite topologique [20–22] en domaine fréquentiel, encore très peu appliquée aux guides d'ondes.

Le point de départ de l'imagerie topologique est le problème de minimisation de la fonctionnelle de coût suivante :

$$j(\Omega) = \mathrm{J}(\mathbf{u}) = \frac{1}{2}\int_{\mathbb{R}^+}\int_{S_{\mathrm{obs}}} |\mathbf{u}(\mathbf{x},\Omega,\omega) - \mathbf{u}_{\mathrm{obs}}(\mathbf{x},\omega)|^2 \mathrm{d}S_{\mathrm{obs}}\mathrm{d}\omega. \tag{11}$$

$\mathbf{u}_{\mathrm{obs}}$ est le champ mesuré sur une surface d'observation S_{obs} dans le milieu réel incluant des défauts. $\mathbf{u}(\mathbf{x},\Omega,\omega)$ est le champ mesuré sur S_{obs} dans un milieu fictif Ω incluant une répartition arbitraire de défauts. La fonctionnelle $j(\Omega)$ traduit donc l'écart de topologie entre les deux milieux.

Ce problème de minimisation est reformulé comme un problème d'optimisation sous contrainte, d'abord dans un cadre général puis dans le cas particulier de l'imagerie topologique.

Cette approche fait naturellement apparaître une fonction appelée gradient topologique, et deux problèmes associés qui sont les problèmes direct et adjoint. Au final, la fonctionnelle s'écrit au premier ordre [20, 21] :

$$j(\Omega) = j(\Omega_0) + f(\epsilon)g(\mathbf{x}) + o(f(\epsilon)), \quad \forall \mathbf{x} \in \Omega_0, \epsilon \to 0^+, f(\epsilon) > 0, \tag{12}$$

où $j(\Omega_0)$ est la fonctionnelle pour un milieu de référence Ω_0, considéré comme sain (sans défaut) dans cette thèse. Le gradient topologique $g(\mathbf{x})$ caractérise la sensibilité de la fonctionnelle à l'introduction d'un défaut infinitésimal (de taille caractéristique $\epsilon \to 0^+$, centré en $\mathbf{x}$) dans le milieu de référence. Évalué en chaque point du milieu fictif sain, le gradient est censé prendre des valeurs importantes à l'emplacement des défauts présents dans le milieu réel. Le gradient topologique peut alors être utilisé comme une fonction d'imagerie, dont la représentation spatiale forme une image révélatrice de la position des défauts réels.

Concrètement, la première étape de l'imagerie topologique consiste à émettre des ondes, puis, à les mesurer dans le milieu réel. Ceci permet d'obtenir le champ $\mathbf{u}_{\text{obs}}$ sur la surface S_{obs}. Ensuite, deux problèmes sont simulés dans le milieu de référence. Dans le problème direct, la source expérimentale est simulée et le champ direct ($\mathbf{u}$) est calculé en tout point du milieu de référence (dont S_{obs}). Dans le problème adjoint, la source correspond au résidu ($\mathbf{u} - \mathbf{u}_{\text{obs}}$) mesuré sur S_{obs}, puis réémis après retournement temporel. Le champ adjoint ($\mathbf{v}$) est alors calculé en tout point du domaine de référence. Le gradient topologique est finalement obtenu à partir des champs directs et adjoints, à l'aide d'une formulation spécifique du type de défaut recherché. Pour résumer, l'image est obtenue à l'aide d'une mesure dans le milieu endommagé, et de deux simulations dans le milieu de référence. Ce processus est non itératif, puisque le calcul du gradient n'est réalisé qu'une fois, à partir de l'état (sain) de référence.

Dans un cadre expérimental, des versions simplifiées du gradient théorique sont généralement utilisées [20, 22, 23]. Les simplifications effectuées rendent le gradient similaire à un gradient révélant des variations de densité, si bien que ces formulations empiriques ne sont généralement plus spécifiques de la topologie du défaut recherché. À titre d'exemple, nous rappelons ici l'une de ces expressions :

$$g_e(\mathbf{x}) = |\int_{\mathbb{R}^+} \mathbf{u}(\mathbf{x}, \omega) \cdot \mathbf{v}(\mathbf{x}, \omega) \mathrm{d}\omega|, \forall \mathbf{x} \in \Omega_0. \tag{13}$$

Ainsi qu'expliqué dans la Ref. [23], l'Eq. (13) permet d'obtenir une image avec une seule tâche focale au niveau du défaut (enveloppe) sans augmenter le niveau de bruit. Cependant, la question du choix de la fonction d'imagerie reste ouverte.

L'application de l'imagerie topologique aux guides d'ondes ouverts soulève plusieurs questions. Tout d'abord, la capacité de la méthode à tirer parti d'un champ de nature complexe (champ dispersif, multimodal, atténué par fuite...) doit être étudiée. D'autre part, les guides d'ondes ouverts ne sont généralement que partiellement accessibles. Ceci restreint la mesure au champ réfléchi (pas d'accès au champ transmis), et à la surface du guide (pas de mesure dans la section). Il est donc nécessaire d'étudier le comportement de la méthode avec une mesure restreinte du champ.

Afin de mieux comprendre l'influence des divers paramètres et formulations de la méthode, nous étudions tout d'abord le cas d'un guide d'onde fermé, circulaire, et axisymétrique. Pour anticiper le cas du guide ouvert, la configuration de mesure est restreinte au champ réfléchi et à la surface du guide, sur laquelle un ensemble de transducteurs ponctuels est positionné. Grâce à la méthode numérique hybride développée et présentée dans le Chap. 3, la mesure du champ diffracté par un défaut dans un guide peut être simulée efficacement. De plus, grâce au formalisme modal, les champs direct et adjoint peuvent être obtenus très rapidement en tout point du domaine de référence via le calcul de la réponse forcée (présentée dans le Chap. 2).

Les résultats montrent qu'en émettant un champ monomodal, y compris dispersif, le défaut est localisé suivant l'axe du guide, mais pas dans la section. En effet, l'image obtenue peut être directement reliée à la déformée du mode considéré. La dispersion ne perturbe pas la localisation si elle est prise en compte en tant qu'information a priori dans les modèles. Il est notable qu'un seul transducteur soit suffisant pour obtenir l'image axiale.

Pour obtenir une meilleure localisation dans la direction transverse (section) du guide, il est nécessaire d'émettre plusieurs modes. Néanmoins dans ce cas, des artefacts apparaissent dans l'image. Nous montrons que ces artefacts sont liés à des conversions modales, dues à la fois à la source de l'état adjoint et au défaut. L'emplacement des artefacts dans l'image dépend de la distance entre le transducteur et le défaut. L'amplitude relative des artefacts peut donc être réduite en utilisant plusieurs transducteurs suffisamment espacés. Le nombre de transducteurs nécessaires à une localisation acceptable reste raisonnable, ce qui est encourageant pour de futures applications expérimentales. Nous montrons également que la combinaison d'un profil unidimensionnel axial, extrait d'une image monomodale, avec une image multimodale, permet de réduire facilement l'amplitude des artefacts de l'image.

La méthode est ensuite appliquée pour imager un défaut situé dans le cœur d'un guide ouvert. Le champ diffracté est mesuré à l'interface entre le cœur et le milieu environnant. Nous montrons que l'image est décentrée en amont du défaut, en raison de l'importante atténuation par fuites des ondes. Ceci empêche de localiser correctement le défaut. Grâce au formalisme modal utilisé pour le calcul des champs direct et adjoint, il est possible de supprimer très facilement l'atténuation des modes à fuite tout en préservant leur temps de vol. En effet, il suffit, pour cela, de ne considérer que la partie réelle du nombre d'onde dans les superpositions modales (voir par exemple l'Eq. (6)). Ceci permet de recentrer l'image sur le défaut.

Conclusion

Dans cette thèse, nous avons développé des méthodes numériques pour le calcul de la réponse forcée et du champ diffracté dans les guides d'ondes élastiques ouverts. Les résultats obtenus permettent une meilleure analyse physique du comportement des modes à fuite utilisés en CND. Nous avons montré que dans une région restreinte de l'espace (mais la plus intéressante pour le CND), les solutions peuvent être approximées par la contribution des modes à fuite seulement. En général, les modes de PML contribuent au champ très proche, ainsi qu'au phénomène de diffraction à long terme (champ très lointain). L'approximation des solutions par les modes à fuite présente un intérêt majeur pour les méthodes proposées, car elle permet de réduire l'épaisseur de la PML et le nombre de modes à calculer, et donc le coût des calculs. Enfin, ces travaux ont permis d'étendre le champ d'application des méthodes basées sur un formalisme modal à l'imagerie des guides d'ondes. À partir d'un seul calcul aux valeurs propres, les solutions de problèmes variés peuvent ainsi être obtenues rapidement.

Concernant l'imagerie, nous soulignons en perspective qu'il serait intéressant de simuler une configuration idéale de mesure, incluant le champ transmis ainsi que le champ dans la section du guide, et avec l'émission de modes supplémentaires. Ceci permettrait d'identifier l'image optimale atteignable en guide d'onde, et par suite de comprendre les différents facteurs de dégradations de l'image. Des expérimentations sur maquette en laboratoire sont également indispensables.

Introduction

Non-destructive evaluation (NDE) techniques allow characterizing a structure without causing any damages. They are used in production or maintenance stages in a lot of industries such as aeronautics, aerospace, transportation, energy, and civil engineering. Analysing the measurement results helps to detect, to locate and to characterize defects, and thereby to prevent structural failure.

This thesis focuses on ultrasonic NDE in *civil engineering*. Numerous structures of civil engineering are elongated, such as bars, cables, rails or pipes. A lot of them can be partially or quasi-fully embedded into a solid elastic medium (cement, rock...). Figure 1 shows examples of embedded rock bolt and tendons. The access to these structures is often restricted to their protruding part. NDE techniques based on guided ultrasonic waves are interesting, owing to the guided waves ability to propagate far from a single measurement position. Embedded structures can be considered as *open waveguides*, made of an elastic core (the guiding structure) surrounded by an infinite elastic medium, so that the transverse directions are unbounded.

In practice, the complexity of guided wave propagation makes NDE difficult. Guided waves are multimodal (several wave packets can propagate with different velocities) and dispersive (each modal velocity depends on the frequency). Furthermore, in open waveguides most of the waves suffer from radiation losses in the embedding medium (leakage attenuation). A good knowledge of axial attenuation, group, energy and phase velocities of the modes is hence necessary to correctly interpret the results of an NDE test case. These properties are usually displayed with respect to frequency to obtain the so-called dispersion curves. The analysis of the dispersion curves enables to identify the best combination of the less attenuated, the less dispersive and the fastest modes to facilitate NDE [24].


(a) (b)

Figure 1 – Examples of open waveguide-like structures in civil engineering: (a) Embedded rock bolt; (b) Embedded tendon.

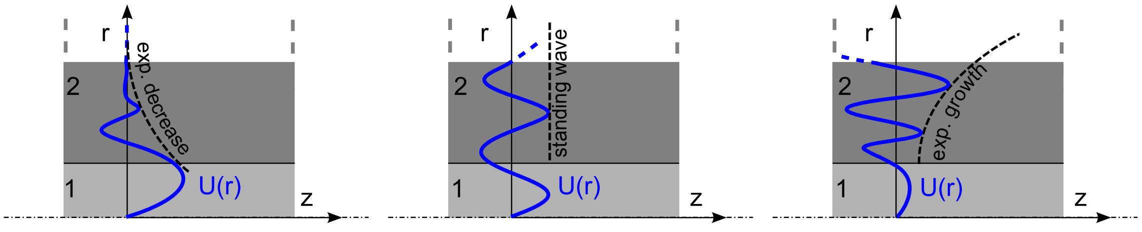

(a) (b) (c)

Figure 2 – Schematic displacement mode shapes $U(r)$ in an open waveguide (1: core, 2: infinite surrounding medium, z: axis of the waveguide, r: transverse direction). (a) Trapped mode; (b) Radiation mode; (c) Leaky mode.

The main part of the physical analysis of guided wave propagation then relies on a modal description of the waves, which is actually the best suited representation for a detailed understanding. In closed waveguides (*i.e.* waveguides in vacuum), modes can be separated into propagating modes (the modes of interest for NDE) and non-propagating modes. Nevertheless, in open waveguides the underlying physics is deeply modified. Indeed, three main kinds of modes are distinguished: trapped modes, radiation modes, and *leaky modes*.

Let us briefly described their characteristics. Figure 2 displays their schematic mode shapes for clarity. Trapped modes propagate without leakage attenuation along the waveguide axis and decay exponentially in the transverse direction (Fig. 2a). These waves are confined in the core of the waveguide or at the interface between the core and the embedding medium. Trapped modes exist only if the shear velocity is greater in the core, unless longitudinal and shear bulk waves couple into interface trapped waves, called Stoneley waves [1]. This is generally not the case in civil engineering structures. Thereby, trapped modes cannot be often used for NDE. Radiation modes are standing waves in the transverse direction, which are propagative or evanescent in the axis direction [2, 3] (Fig. 2b). Finally, leaky modes propagate with leakage attenuation along the waveguide axis (they decay exponentially in the axial direction). Strangely, at first sight, these modes grow exponentially in the transverse direction [2, 6, 7] (Fig. 2c). However, the dispersion curves of leaky modes can provide useful practical information for NDE, such as the axial attenuation and the travelling velocity of wave packets [4].

Several methods have been developed to compute the modes of open waveguides. Analytical methods (*e.g.* the Thomson-Haskell [25, 26], the stiffness matrix [27] or the global matrix [28] methods) are yet limited to canonical waveguide geometries. Numerical methods are well-suited for more complex geometries. These methods are based on a *waveguide formulation* of the problem, often known as the Semi-Analytical Finite Element (SAFE) method in closed waveguides [29, 30] (actually, the method has been applied under various names in the literature, as recalled in the introduction of Chap. 2). The idea is to discretize only the cross-section of the waveguide while describing analytically the direction of the wave propagation. In closed waveguides, this approach yields a linear eigenvalue problem. In open waveguides, it is necessary to couple the waveguide formulation with other techniques to cope with the unbounded nature of the problem and the growth of leaky modes in the transverse directions.

In a previous thesis work at Ifsttar [9], a *Perfectly Matched Layer (PML)* of finite thickness has been introduced to model the surrounding medium. The transverse growth of leaky modes can be cancelled out by the PML attenuation. Furthermore, the PML avoids most spurious reflections from the layer, which allows greatly reducing its thickness. A bounded cross-section of reasonable size is finally obtained. On this cross-section, the so-called *PML waveguide formulation* (or SAFE-PML) still yields a linear eigenvalue problem. It has been applied to compute the modes of two-dimensional waveguides (plates [12], pipes [31]) and three-dimensional waveguides (circular [13], square [32], helical [33]) embedded in solids or in water [34]. We mention here that various other methods have also been proposed in the literature, *e.g.* exact boundary conditions to avoid the discretization of the surrounding medium [35, 36] or absorbing layers [37]. These methods are thoroughly discussed in the introduction of Chap. 2.

With a PML waveguide formulation, three types of modes are computed: trapped modes, leaky modes, and *PML modes* (also called Berenger modes). PML modes are non-intrinsic to the physics. They oscillate mainly inside the PML and depend on its parameters. PML modes must be filtered out to post-process the dispersion curves of trapped modes and leaky modes only.

To enrich the numerical modelling of open waveguides, it appears necessary to consider the forced response and the diffraction problems. The first objective of this thesis is to provide modelling tools for a further understanding of the emission, the propagation and the diffraction of leaky modes for any geometry of waveguides. A particular attention has to be given to solutions at high-frequencies because leaky modes with a low attenuation can occur [4] (thus increasing the inspection range for NDE). A natural idea is to build a solution with modal superpositions, based on the modes already computed with the PML waveguide formulation. Several examples can be found in the closed waveguide literature, see *e.g.* Refs. [19, 30, 38, 39]. The extension of these methods to open waveguides is yet not straightforward, owing to the complexity of the modal basis.

We recall that theoretically any wave field propagating in an open waveguide is described by a superposition of a discrete set of trapped modes and two continuous sets of radiations modes [3, 5]. Leaky modes initially do not belong to the modal basis because of their growth in the transverse directions [3]. When a finite PML is introduced in the surrounding medium, it is hence necessary to understand the contribution of each type of modes to the solution. Particularly, the contribution of leaky modes to the solution has to be clarified. A second issue is the influence of PML modes on the solution. As recalled earlier, these modes are non-intrinsic to the physics, owing to their dependence on PML parameters. Nevertheless, they could provide a significant contribution to the solution, which must be investigated. Besides, it is also necessary to derive an orthogonality relationship, applicable for the PML waveguide formulation modes, to guarantee the uniqueness of the modal superpositions [40].

An additional objective of this thesis is to implement an imaging tool for open waveguides, which leads us to study *inverse problems* theory. The aim is to locate one or several defects embedded into the waveguide from a measure of the scattered field. More precisely, the desired outputs are the location of the defects along the waveguide axis and, if possible, along the transverse directions also.

In this work, the *topological imaging* method is applied [20, 21]. This method is based on the design of an imaging function (the so-called topological gradient), which gives the sensitivity of a misfit cost-functional to the inclusion of an infinitesimal cavity inside a reference medium. The spatial representation of this function naturally reveals the positions of defects, without any iteration. In practice, the image is obtained by measurements in the real medium and two simulations in the reference medium, corresponding to the so-called forward and adjoint fields.

Topological imaging has been barely applied to elastic waveguides and only using a monomodal wavefield [22]. Thereby, the first step is to investigate the behaviour of the method with a dispersive and multimodal wavefield. Furthermore, it is necessary to study the influence of the measurement configuration (number and location of transducers) on the quality of the image. Particularly in an open waveguide, the limited access to the structure restricts the measurements to the reflected field only.

The present manuscript is divided into four chapters.

Chapter 1. The aim is to bring insights into the modal basis of open waveguides obtained with a PML. The theoretical background (without PML) is given for the Helmholtz equation with a source in an unbounded domain. From the forced response in the wavenumber domain, it is recalled how the inverse transform makes the modal basis appear. A PML of infinite thickness is then introduced through an analytical continuation of the equations. The role in the solution of PML modes and leaky modes is explained. The results are finally extended to the elastodynamic case.

Chapter 2. The forced response of elastic open waveguides is numerically obtained with a modal approach based on PML. Modes are computed with a PML waveguide formulation. A general biorthogonality relationship is derived to obtain a unique modal expansion of the forced response. This relation also leads to an expression of the modal excitability of leaky modes. To validate the method, the forced response is computed in a homogeneous medium test case and compared to a transient analytical solution. This test case also enables to clarify the contribution of PML modes to the solution. Then transient signals are computed in a circular bar waveguide. The role of leaky modes is clarified. High-frequency signals of practical interest for NDE are obtained. Finally, a buried square bar is considered as an example of three-dimensional waveguide.

Chapter 3. A hybrid approach is proposed to compute the leaky mode scattering by local inhomogeneities in elastic open waveguides. The damaged zone of the waveguide and its vicinity are described by a finite-element method (with a PML). This method is then coupled on the cross-section boundaries to a modal representation of the field propagating along the waveguide axis in the undamaged parts, yielding transparent boundary conditions. The scattering at the junction between a closed and an open cylindrical waveguide is considered. The solution is compared to literature results. Then the scattering by an axisymmetrical notch is studied at low and high frequencies. Reflection and transmission coefficients of leaky modes are obtained. The influence of PML modes on the near-field solution is highlighted throughout these tests. Besides, it is shown that there is no power orthogonality in open waveguides. Finally, the generality of the proposed method is discussed through a three-dimensional test case considering an embedded bar with an oblique break.

Chapter 4. The topological imaging method is applied to waveguides. First, a general framework is recalled based on constrained optimization theory for inverse problems in elastodynamics. The specific case of topological imaging is subsequently treated. The methods presented in Chaps. 2 and 3 are used to simulate measurement in a damaged medium. The forward and adjoint fields are efficiently obtained from the forced response of the reference medium (*i.e.* without damage). The quality of defect imaging is then discussed in a closed waveguide for monomodal, dispersive and multimodal wave fields respectively. Several measurement configurations are considered. Various formulations of the imaging function are used and compared. Then, preliminary results are presented for an open waveguide.

In conclusion, outlooks are given for future works.

The work presented in this thesis has been partially published in the referred papers:

- M. Gallezot, F. Treyssède, and L. Laguerre, Contribution of leaky modes in the modal analysis of unbounded problems with perfectly matched layers, *Journal of the Acoustical Society of America* 141 (2017), EL16–EL21, DOI: 10.1121/1.4973313
- M. Gallezot, F. Treyssède, and L. Laguerre, A numerical method for the scattering by defects in axisymmetrical open elastic waveguides, *Procedia Engineering* 199 (2017), pp. 1527–1532
- M. Gallezot, F. Treyssède, and L. Laguerre, A modal approach based on perfectly matched layers for the forced response of elastic open waveguides, *Journal of Computational Physics* 356 (2018), pp. 391–409, DOI: 10.1016/j.jcp.2017.12.017
- M. Gallezot, F. Treyssède, and L. Laguerre, Numerical modelling of wave scattering by local inhomogeneities in elastic waveguides embedded into infinite media, *Journal of Sound and Vibration* (2018), DOI: 10.1016/j.jsv.2018.11.044

Chapter 1

Contribution of leaky modes in the modal analysis of unbounded problems with perfectly matched layers

Note : an important preliminary work has eventually lead to this concise chapter. For more details, the reader is invited to refer to working papers [45] and [46] (in French).

1.1 Introduction

Modal analysis is a powerful tool for treating bounded wave problems, for which modes provide a discrete basis that allows in-depth physical analysis. For unbounded problems, the modal basis is yet more complicated because it involves a continuous sum of modes (radiation modes) in addition to a discrete set (trapped modes, if any) [3]. This contribution of the continuum is usually quite difficult to calculate and interpret from a physical point of view. Based on steepest descent techniques, for example, it can be approximated by a discrete set of another class of modes, the so-called leaky modes [10]. These modes behave like attenuated modes and reveal some interesting physical features. For instance, they can give the leakage attenuation of wave packets in open waveguides, which is of particular interest in the field of nondestructive evaluation (NDE) [4]. However, leaky modes correspond to improper modes that spatially grow to infinity in the unbounded direction of the problem (they are not part of the modal basis). Their use in modal analysis hence requires special care.

As for numerical methods, perfectly matched layers (PMLs) have been widely employed to efficiently simulate infinite media. More particularly, they have been successfully applied to compute modes in open systems [12, 47]. It has been shown that PMLs allow getting both trapped and leaky modes as well as a third type of modes sometimes called PML modes [48]. PML modes mainly resonate inside the PML region (their fields strongly depend on PML parameters). However, the contribution of these different kinds of modes in a modal analysis may still be unclear. This chapter aims to bring insight into the modal basis computed with PMLs and to justify its use for the analysis of excitation problems (Chap. 2 of this thesis) and scattering problems (Chap. 3 of this thesis) using a modal approach. Without loss of generality, two-dimensional waveguides are considered. For simplicity, the analysis starts from the scalar wave equation and is then extended to elastodynamics, where two continua occur instead of one.

1.2 Background

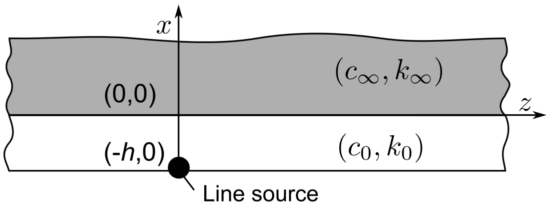

Figure 1.1 – Example of a two-dimensional bilayer open waveguide

This section briefly recalls some theoretical results [2, 3, 10] taking the example of a two-dimensional bilayer waveguide, homogeneous and infinite in the axial direction z as shown in Fig. 1.1. In the transverse direction, the bottom layer is labelled 0 and extends from $x{=}-h$ to $x{=}0$. The top layer is infinite and labelled ∞. The wave field solution to the problem satisfies the Helmholtz equation in both layers and is denoted in the angular frequency-wavenumber domain by $\psi(x,\beta,\omega)$, where β and ω are the axial wavenumber and the angular frequency. A convention in $\mathrm{e}^{\mathrm{j}(\beta z-\omega t)}$ is adopted for the harmonic dependence of wave fields. The transverse wavenumbers in the two layers are given by $\alpha_{0,\infty}^2{=}k_{0,\infty}^2-\beta^2$, with $k_{0,\infty}{=}\omega/c_{0,\infty}$. In this chapter, $'$ or Re and $''$ or Im will denote respectively the real part and the imaginary part of a complex number. As an example, let us assume that the waveguide in Fig. 1.1 is excited by an out-of-plane line source located at $(x,z)=(-h,0)$ through the Neumann boundary condition: $\mathrm{d}\psi(-h,z,\omega)/\mathrm{d}x = s(\omega)\delta(z)$.

The solution must also satisfy continuity conditions at the interface ($x{=}0$) and must be bounded and outwards at infinity [10] ($x\to\infty$). The spatial inverse Fourier transform of the solution leads to an expression of the following form:

$$\psi(x,z,\omega)=\begin{cases}\frac{s(\omega)}{2\pi}\int_{\mathbb{R}}\frac{\alpha_0\cos(\alpha_0 x)+\mathrm{j}C_m\alpha_\infty\sin(\alpha_0 x)}{\alpha_0[\alpha_0\sin(\alpha_0 h)+\mathrm{j}C_m\alpha_\infty\cos(\alpha_0 h)]}\mathrm{e}^{\mathrm{j}\beta z}\mathrm{d}\beta & \text{if } -h\le x\le 0,\\ \frac{s(\omega)}{2\pi}\int_{\mathbb{R}}\frac{1}{\alpha_0\sin(\alpha_0 h)+\mathrm{j}C_m\alpha_\infty\cos(\alpha_0 h)}\mathrm{e}^{\mathrm{j}\alpha_\infty x}\mathrm{e}^{\mathrm{j}\beta z}\mathrm{d}\beta & \text{if } x>0,\end{cases}\tag{1.1}$$

where C_m is a ratio of material properties which depends on the problem type (*i.e.* dielectric, acoustic or SH-elastic). First, a lossy outer medium is assumed (*i.e.* $k''_\infty{>}0$). The key point is the value of α_∞, which depends on the sign of the square root of $k_\infty^2-\beta^2$ and hence defines a two-sheeted Riemann surface [10]. Let us consider the two sheets defined by $\alpha''_\infty{>}0$ and $\alpha''_\infty{<}0$ respectively. The corresponding branch cut is given by $\alpha''_\infty{=}0$ and is a portion of hyperbola [3] in the (β',β'') plane beginning at branch point (k'_∞,k''_∞), as shown in Fig. 1.2a. The remaining portion of the hyperbola satisfies the equation $\alpha'_\infty{=}0$.

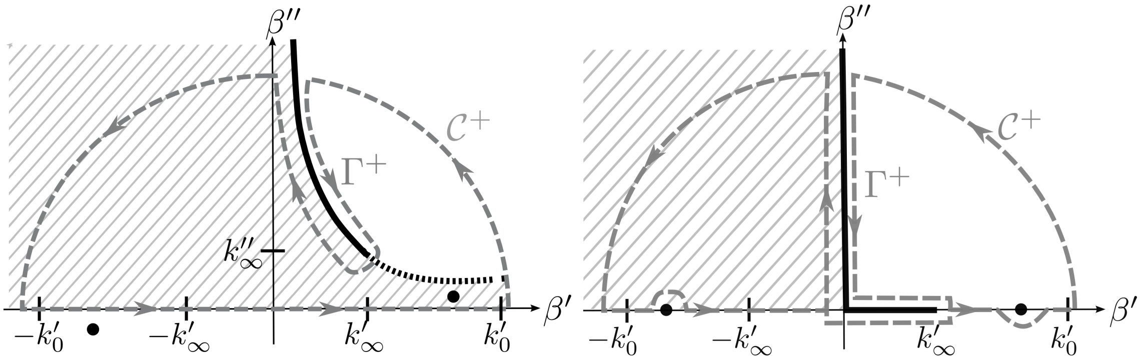

(a) (b)

Figure 1.2 – Representation of the proper sheet α''_∞>0 in the upper complex plane β''>0: (a) lossy medium, (b) lossless. Branch cut α''_∞=0 (thick line), curve α'_∞=0 (dotted line), trapped modes (●), integration contour (dashed line). Hatched region: α'_∞>0. White region: α'_∞<0.

The integrals in Eq. (1.1) can be evaluated thanks to Cauchy's residue theorem. The path $\mathbb{R}$ is conveniently closed by a semi-infinite circle along which the integrals vanish. This implies that the exponentials $\mathrm{e}^{\mathrm{j}\alpha_\infty x}$ and $\mathrm{e}^{\mathrm{j}\beta z}$ must tend to zero at infinity. For clarity, let us focus on the solution in the region z>0, where waves are positive-going and decreasing (β''>0). In this case, the integration must be carried out on the upper semi-circle $\mathcal{C}^+$, defined by β''>0 and located on the proper sheet, which is α''_∞>0 (the improper sheet being α''_∞<0). Furthermore, the branch cut is a discontinuity that cannot be crossed. It must be circumvented by the path Γ^+ (see Fig. 1.2a). Finally, on the contour $\mathbb{R}+\Gamma^+ +\mathcal{C}^+$, the application of the residue theorem leads to $\int_\mathbb{R}=2\pi\mathrm{j}\sum$ residues $-\int_{\Gamma^+}$. The residues are calculated from the poles (zeros of denominators of Eq. (1.1)) that lie on the proper Riemann sheet α''_∞>0, that is to say the trapped modes. Thus, two parts contribute to $\psi(x, z, \omega)$. The first one is a discrete sum of positive going trapped modes. The second part is a continuous sum and stands for the continuum of radiation modes.

Together, trapped modes and radiation modes form the modal basis of an open waveguide [3]:

$$\psi(x, z, \omega) = \sum \text{trapped} + \int_{\Gamma^+} \text{radiation modes.} \tag{1.2}$$

As mentioned previously, the continuum is difficult to handle. Its contribution can be approximated by a discrete sum of a third class of modes, the so-called leaky modes (*e.g.* using the steepest descent method [11]). It has to be emphasised that leaky modes are also poles of Eq. (1.1). However, they do not belong to the modal basis because they are improper poles that lie in the negative Riemann sheet [10] α''_∞<0. Hence, leaky modes grow to infinity in the transverse direction. They can approximate the wave field only in a strictly delimited spatial region [16]. From a physical point of view, leaky modes might be seen in the bottom layer as imperfect guided waves that suffer from leakage attenuation, while trapped modes are guided waves that propagate without leakage attenuation. Radiation modes form standing waves in the transverse direction and can be propagative or evanescent in the axial direction [2].

The lossless case (k''_∞=0), not considered so far, can be readily deduced asymptotically and is shown in Fig. 1.2b. If the medium is lossless, trapped modes have purely real wavenumbers [10] and exist only if k_∞<β<k_0.

Note that the problem given by Eq. (1.1) has been introduced in this section for illustrative purposes only. The main results of this chapter will apply to more complex open waveguides (*e.g.* multilayered or excited by other types of source), since the analysis in the remainder essentially lies in the definition of the branch cut of the square root, which is intrinsic to the half-space.

1.3 Modal basis with a PML

A PML is now applied in the infinite top layer. This amounts to perform an analytical extension [49] for $x>0$ with the change of variable $\tilde{x}=\int_0^x \gamma(\zeta)\mathrm{d}\zeta$, where $\gamma(x)$ is a complex function such that $\arg\gamma \in [0;\pi/2[$. For simplicity, let us consider a constant function inside the whole top layer ($\gamma(x)=\gamma$). In this case, $\tilde{x}=\gamma x$ in the top layer. It can be readily checked that solving the Helmholtz equation in both layers yields the same solution as Eq. (1.1) except that the term $\mathrm{e}^{\mathrm{j}\alpha_\infty x}$ is now replaced with $\mathrm{e}^{\mathrm{j}\tilde{\alpha}_\infty x}$, where $\tilde{\alpha}_\infty=\gamma\alpha_\infty$. The poles of the denominators (trapped and leaky modes) are left unchanged by the PML.

Following the same approach as in Sec. 1.2, the application of the residue theorem requires considering a new proper Riemann sheet, defined by $\tilde{\alpha}''_\infty>0$. Consequently, the branch cut is now given by $\tilde{\alpha}''_\infty=0$ and defines a new integration path denoted by $\tilde{\Gamma}^+$. To understand the effect of the PML on the modal basis, it is necessary to look further into the branch cut transformation induced by the PML, namely from Γ^+ to $\tilde{\Gamma}^+$.

The branch cut $\tilde{\alpha}''_\infty = 0 = \pm\mathrm{Im}\sqrt{\mathrm{Re}\,\tilde{\alpha}^2_\infty + \mathrm{j}\mathrm{Im}\,\tilde{\alpha}^2_\infty}$ in the (β',β'') plane can be unequivocally determined by the following conditions: $\mathrm{Im}\,\tilde{\alpha}^2_\infty = 0$ and $\mathrm{Re}\,\tilde{\alpha}^2_\infty > 0$ (see Ref. 1 pp. 180–181 for the case without PML). Then, from the expansion $\tilde{\alpha}^2_\infty = (\gamma'+\mathrm{j}\gamma'')(k'^2_\infty - k''^2_\infty - \beta'^2 + \beta''^2 + 2\mathrm{j}(k'_\infty k''_\infty - \beta'\beta''))$, the equation $\mathrm{Im}\,\tilde{\alpha}^2_\infty = 2\tilde{\alpha}'_\infty\tilde{\alpha}''_\infty = 0$ becomes:

$$A\beta'^2 + B\beta'\beta'' + C\beta''^2 + D = 0, \tag{1.3}$$

with $C=-A=\gamma'\gamma'', B=\gamma''^2-\gamma'^2, D=\gamma'\gamma''(k'^2_\infty - k''^2_\infty) + (\gamma'^2-\gamma''^2)k'_\infty k''_\infty$. Equation (1.3) represents a hyperbola in the frame (β',β''). The principal axes of this hyperbola make an angle θ with the axes of the frame given by the formula $\cot 2\theta=(A-C)/B$, which leads:

$$\theta = \frac{\pi}{4} - \arg\gamma. \tag{1.4}$$

From the study of the sign of $\mathrm{Re}\,\tilde{\alpha}^2_\infty$, it can be checked that the branch cut $\tilde{\alpha}''_\infty=0$ is on the upper part of the hyperbola and that the lowest part corresponds to the curve $\tilde{\alpha}'_\infty=0$. Both parts are delimited by the branch point (k'_∞, k''_∞), analogously to the case without PML.

Without PML, $\arg\gamma=0$ and $\theta=\frac{\pi}{4}$: the asymptotes of the hyperbola coincide with the real and imaginary axes (as already shown in Fig. 1.2a). With PML, the angle becomes $\frac{\pi}{4}-\arg\gamma$: the asymptotes are rotated by $-\arg\gamma$. Hence, the branch cut transformation from Γ^+ to $\tilde{\Gamma}^+$ is a rotation of an angle equal to $-\arg\gamma$ (see Fig. 1.3a). In the lossless case (Fig. 1.3b), note that the PML branch cut is still a hyperbola.

As shown hereafter, this branch cut rotation has an important consequence. With PML, the proper Riemann sheet satisfies $\tilde{\alpha}''_\infty>0$ (*i.e.* $0<\arg\tilde{\alpha}_\infty<\pi$), or equivalently by using the equality $\arg\tilde{\alpha}_\infty=\arg\gamma+\arg\alpha_\infty$:

$$-\arg\gamma < \arg\alpha_\infty < \pi - \arg\gamma. \tag{1.5}$$

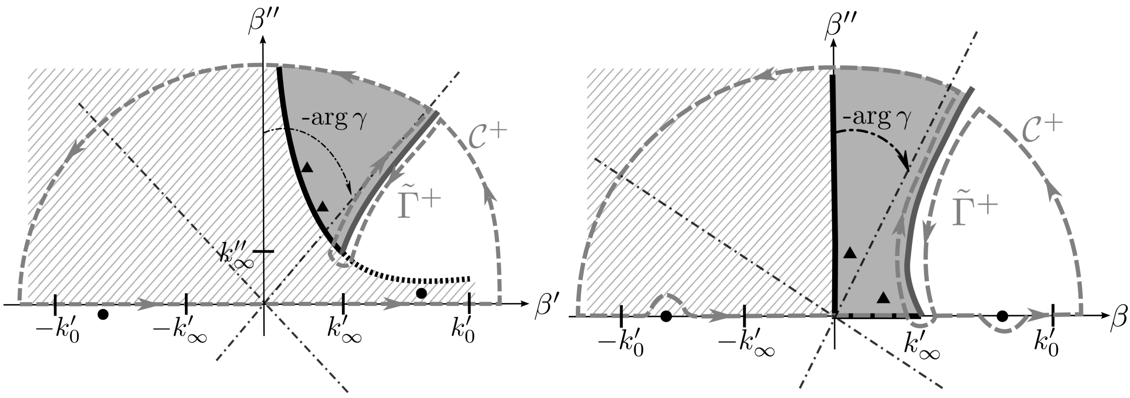

(a) (b)

Figure 1.3 – Representation of the proper sheet with PML $\tilde{\alpha}''_\infty>0$ in the upper complex plane $\beta''>0$: (a) lossy medium, (b) lossless. Same legend as in Fig. 1.2 and: PML branch cut $\tilde{\alpha}''_\infty=0$ (thick gray line) with its asymptotes (dashed dotted), leaky modes (▲), revealed part of the improper sheet $\alpha''_\infty<0$ (grey shaded region, satisfying $\alpha'_\infty>0$).

In particular, the PML gives access to the region $-\arg\gamma<\arg\alpha_\infty<0$ (shaded region in Fig. 1.3), which belongs to the initial improper sheet $\alpha''_\infty<0$ where leaky modes occur. In other words, the rotation induced by the PML allows revealing the contribution of the leaky modes satisfying $\arg\alpha_\infty>-\arg\gamma$. These revealed leaky modes are proper poles of the problem with PML. Note that Eq. (1.5) coincides with the condition found for a PML to cancel the transverse exponential growth of a leaky mode [12, 47].

To summarize, the integration contour with PML is $\mathbb{R}+\mathcal{C}^++\tilde{\Gamma}^+$ as shown in Fig. 1.3. Applying Cauchy's residue theorem on this contour yields:

$$\psi(x,z,\omega)=\sum\text{trapped}+\sum\text{revealed leaky}+\int_{\tilde{\Gamma}^+}\text{PML modes}. \tag{1.6}$$

The PML hence defines a new modal basis which properly includes some leaky modes. This modal basis still involves a continuum of modes, which mainly resonate inside the PML (PML modes). One must yet keep in mind that the field inside the PML is not physical: Eq. (1.6) coincides with the physical solution (1.2) only in the region out of the PML.

Inside the accessible region of the sheet $\alpha''_\infty<0$ (*i.e.* the shaded region in Fig. 1.3) the sign of α'_∞ is single-valued and can be determined as follows. In the case without PML, the hyperbola given by Eq. (1.3) delimits two regions in the complex plane, $\alpha'_\infty\alpha''_\infty>0$ (hatched region) and $\alpha'_\infty\alpha''_\infty<0$ (white region) — see Fig. 1.2. The former and the latter are hence such that $\alpha'_\infty>0$ and $\alpha'_\infty<0$ in the proper Riemann sheet (*i.e.* $\alpha''_\infty>0$), and conversely in the improper one ($\alpha''_\infty<0$). Consequently, the revealed part of the sheet $\alpha''_\infty<0$ is such that $\alpha'_\infty>0$: as expected leaky waves are outgoing in the transverse direction.

1.4 The elastodynamic problem

In the elastodynamic case, two transverse wavenumbers must be considered: one for the longitudinal transverse wavenumber, $\alpha_{l\infty}$, and one for the shear transverse wavenumber, $\alpha_{s\infty}$. These are defined from $\alpha^2_{l\infty}=k^2_{l\infty}-\beta^2$ and $\alpha^2_{s\infty}=k^2_{s\infty}-\beta^2$, with $k_{l\infty}=\omega/c_{l\infty}$ and

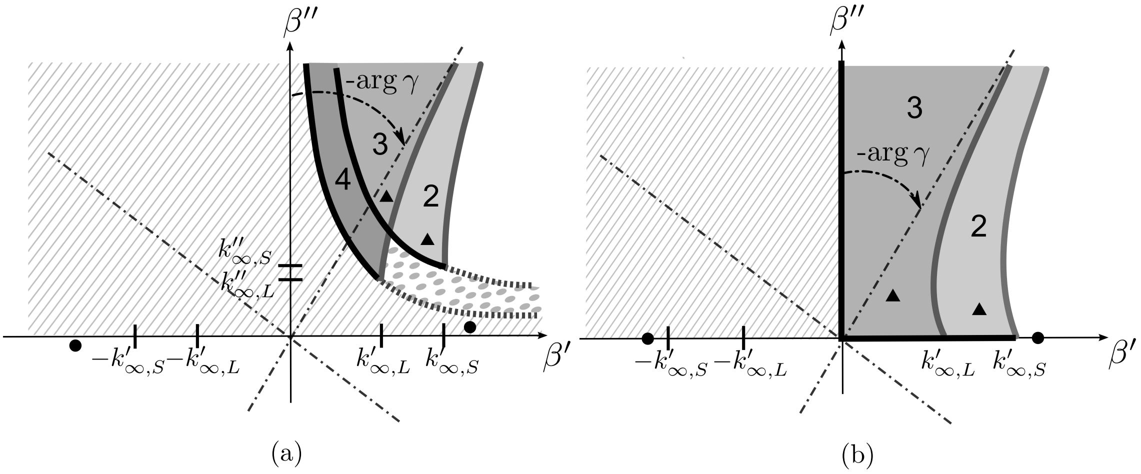

Figure 1.4 – Representation in the elastodynamic case of the proper sheet with PML ($\tilde{\alpha}''_{l\infty}$>0,$\tilde{\alpha}''_{s\infty}$>0): (a) lossy medium, (b) lossless. Same legend as in Fig. 1.3, except that sheet **1** ($\alpha''_{l\infty}$>0, $\alpha''_{s\infty}$>0) is now decomposed into: hatched ($\alpha'_{l\infty}$>0, $\alpha'_{s\infty}$>0), white ($\alpha'_{l\infty}$<0, $\alpha'_{s\infty}$<0) and pea ($\alpha'_{l\infty}$<0, $\alpha'_{s\infty}$>0) regions. Shaded regions: revealed parts of the initial improper sheets **2**, **3** and **4**.

$k_{s\infty}=\omega/c_{s\infty}$. As a consequence, two branch cuts now occur (one for each square root) [5]. Following the previous section, the branch cuts to consider correspond to zero imaginary parts, $\alpha''_{l\infty}$=0 and $\alpha''_{s\infty}$=0. This yields four Riemann sheets, labelled as **1** for ($\alpha''_{l\infty}$>0, $\alpha''_{s\infty}$>0), **2** for ($\alpha''_{l\infty}$>0, $\alpha''_{s\infty}$<0), **3** for ($\alpha''_{l\infty}$<0, $\alpha''_{s\infty}$<0) and **4** for ($\alpha''_{l\infty}$<0, $\alpha''_{s\infty}$>0).

Applying the residue theorem, the elastodynamic solution without PML can then be expressed as a discrete sum of trapped modes and two continuous sums of radiation modes, instead of one in the scalar case. Trapped modes lie on the proper sheet **1** (on the real axis in the lossless case). Extending the results of the previous section, the PML rotates both branch cuts by $-\arg\gamma$. As shown in Fig. 1.4a (lossy case), this rotation reveals parts of the initial improper sheets **2**, **3** and **4**, containing leaky modes. The solution then becomes expressed as a discrete sum of trapped modes, a discrete sum of revealed leaky modes and two continua of PML modes.

Similarly to Sec. 1.3, the sign of $\alpha'_{l\infty}$ and $\alpha'_{s\infty}$ can be determined in the accessible regions of sheets **2**, **3** and **4**. This yields the following results:

Region **2**: $\alpha'_{l\infty} < 0,\ \alpha'_{s\infty} > 0\ (\alpha''_{l\infty} > 0,\ \alpha''_{s\infty} < 0)$
Region **3**: $\alpha'_{l\infty} > 0,\ \alpha'_{s\infty} > 0\ (\alpha''_{l\infty} < 0,\ \alpha''_{s\infty} < 0)$
Region **4**: $\alpha'_{l\infty} > 0,\ \alpha'_{s\infty} > 0\ (\alpha''_{l\infty} < 0,\ \alpha''_{s\infty} > 0)$

Furthermore, the sheet **1** can be decomposed into three regions, as shown in Fig. 1.4a. Note that the transverse longitudinal wavenumbers of leaky modes revealed in sheet **2** have a positive imaginary part together with a negative real part. This partial wave hence behaves like a transverse backward wave decaying at infinity. This does not change the nature of the modes in Region **2**, which are of leaky type owing to the transverse behavior of the partial shear wave (forward and growing at infinity).

In the lossless case (Fig. 1.4b), the sheet **4** cannot be accessible by the PML. In Fig. 1.4a, the revealed region of sheet **4** is located between the two hyperbolas. In Fig. 1.4b, these hyperbolas collapse with the axes of the frame, and so does the revealed part of **4**. Nevertheless, it is pointed out that the contribution of this particular sheet is usually neglected with other approaches regardless PMLs [35, 50].

1.5 Discussion

In addition to trapped modes, a second class of proper modes is likely to occur depending on material properties [11]. These modes lie on the proper sheet but are complex even in the lossless case, as opposed to trapped ones. Hence, the discrete sum of trapped modes in Eqs. (1.2) and (1.6) should also include these complex proper modes (when they exist). Furthermore, trapped modes of backwards type may occur. Such modes have opposite sign of phase and group velocity and have not been represented in the figures of this chapter for simplicity (backwards modes lie on the negative real axis while propagating in the positive direction, and conversely).

Only infinite PMLs have been considered in the previous sections. Yet for numerical implementation, PMLs must be truncated at some finite distance. Both trapped and leaky modes can be accurately computed, even after PML truncation, provided that the PML is properly parametrized [12, 47]. However, the PML truncation transforms the continuous sum of PML modes into a discrete one [48]. At first sight, the role of this discrete sum in the convergence of solutions might be questionable owing to the fact that discrete PML modes strongly depend on the boundary conditions arbitrarily set at the end of the truncated PML. Nevertheless, it has been proved for homogeneous scalar problems that the continuum of PML modes can be truly approximated by a sum over discrete PML modes [15]. The convergence of the discrete sum towards the continuous sum can be achieved depending on the thickness of the PML, its attenuation, and the number of PML modes. Such a convergence cannot be necessarily achieved with absorbing layers of non-perfectly matched type [16].

To conclude, the PML technique may significantly simplify the modal analysis of unbounded problems: this tool, easy to implement from a computational point of view, allows revealing naturally the contribution of leaky modes. Furthermore, the discretized sum of PML modes can be included in the modal basis in order to improve the accuracy of numerical solutions, which may be necessary when the contribution of leaky modes is not sufficient for a desired accuracy. This fully justifies from a numerical point of view the use of the PML technique for the modal analysis of unbounded problems. Numerical results will be shown in Chap. 2. It must be yet recalled that the PML technique is known to fail in elastodynamics for some specific properties of anisotropy of the PML medium [51]. Such situations are beyond the scope of this thesis, in which isotropic materials are implicitly assumed inside the PML.

Chapter 2

A modal approach based on perfectly matched layers for the forced response of elastic open waveguides

2.1 Introduction

2.1.1 Context and state-of-the-art

Elastic guided waves are interesting for many applications involving elongated structures (*e.g.* non-destructive evaluation (NDE), structural health monitoring (SHM), exploration geophysics...), because of their ability to propagate over large distances. When the structure (the core) is embedded into a large solid matrix, it can be considered as an open waveguide (unbounded in the transverse direction). Such a configuration typically occurs in civil engineering and in geophysics for example. Contrary to waveguides in vacuum (closed waveguides), most of the waves in open waveguides are attenuated by leakage in the surrounding medium as they propagate. Moreover, the underlying physics is deeply transformed.

Indeed, in open waveguides, three main kinds of modes are distinguished: trapped modes, radiation modes, and leaky modes. Trapped modes propagate without leakage attenuation along the waveguide axis and decay exponentially in the transverse direction. These waves are confined in the core of the waveguide or at the interface. Their existence depends on material contrasts between the core and the surrounding medium [1]. Radiation modes are standing waves in the transverse direction, which are propagative or evanescent in the axis direction [2, 3]. Finally, leaky modes propagate with leakage attenuation along the waveguide axis. These modes dramatically grow exponentially in the transverse direction [2, 6, 7].

Modes are computed by considering the source-free problem. This can be done by analytical methods (*e.g.* the Thomson-Haskell [25, 26], the stiffness matrix [27] or the global matrix [28] methods), which are yet limited to canonical waveguide geometries. Numerical methods are well-suited for more complex geometries. The idea is then to discretize only the cross-section of the waveguide while describing analytically the direction of the wave propagation. In closed waveguides, this approach yields a linear eigenvalue problem. It has been applied under various names in the literature, such as the extended Ritz technique [52, 53] ; the thin layer method (TLM) for stratified waveguides in geophysics [54, 55] ; the strip-element method [56], the Semi-Analytical Finite Element method (SAFE) [29, 30] or more recently the Scaled Boundary Finite Element Method (SBFEM) [57, 58] in ultrasonics. In this chapter, this approach will be referred to as *waveguide formulation* to avoid the use of acronyms.

Extending the waveguide formulation to open waveguides is not straightforward because of the unbounded nature of the problem in the transverse direction. This difficulty is enhanced by the transverse growth of leaky modes. Therefore, the waveguide formulation must be coupled to other techniques to numerically compute the modes of open waveguides.

The first class of methods avoids the discretization of the embedding medium by using appropriate boundary conditions. The waveguide formulation has been combined with the boundary element method to model three-dimensional waveguides immersed in fluids [59, 60] or embedded in solids [35]. Similarly, exact boundary conditions have been proposed for two-dimensional waveguides (plates and cylinders) immersed in fluids [36]. All of these boundary conditions lead to a highly non-linear eigenproblem that is difficult to solve. The latter can be linearized in the case of two-dimensional plates immersed in perfect fluids [61, 62]. In the case of high-contrast solid waveguides, the waveguide formulation can also be coupled to an approximate condition (the so-called dashpot boundary condition) [63].

With this approximation, the eigenproblem remains linear.

The second class of methods requires a discretization of the surrounding medium, which must be truncated. The eigenproblem remains linear. To avoid spurious reflections due to truncation, the waveguide formulation have been combined with non-reflecting [64] and continued-fraction absorbing [65] boundary conditions in fluids, or paraxial approximation in solids [55, 66]. Absorbing layers of artificially growing damping can also be used to simulate fluid [67] or solid [37] infinite media. Another technique consists in using a Perfectly Matched Layer (PML) to model the infinite surrounding medium (solid or fluid) [12, 13, 32, 34, 68, 69]. Contrary to absorbing layers, the PML avoids most spurious reflections from the layer, which allows its thickness to be greatly reduced. Moreover, it have been shown that the computation of leaky modes with a PML is mathematically relevant (see Ref. [47] for scalar wave problems).

As far as the forced response problem is concerned, modal expansion methods have been widely applied in closed waveguides [40]. However, their application to open elastic waveguides is more intricate and has been barely considered in the literature. With a numerical approach, the particular case of two-dimensional plates immersed in fluids has recently been handled by a waveguide formulation with exact boundary conditions [62]. The case of a stratified plate over or between half-spaces has been treated using a PML in Ref. [69].

As recalled in Chap. 1, theoretically, the forced response of an open waveguide can be expanded on trapped modes and radiation modes [2, 3, 10], such that the displacement field can be symbolically written as:

$$u(\mathbf{r},\omega) = \sum \text{trapped} + \int \text{radiation modes}, \tag{2.1}$$

where, in addition to trapped modes, complex poles of backward type are also likely to occur depending on the problem type [11, 70]. Let us briefly recall the origin of Eq. (2.1) (the reader is invited to refer to Sec. 1.2 of Chap. 1 for more details). In the wavenumber domain, the solution of the problem is a multivalued function owing its dependence on the transverse wavenumber of the unbounded medium. The transverse wavenumber is indeed the square root of a complex number on a two-sheeted Riemann surface. To evaluate analytically the inverse spatial Fourier transform of the solution, a branch cut is defined separating the proper Riemann sheet (where trapped modes occur) from the improper Riemann sheet (where leaky modes occur). Hence, the inverse transform integration is performed only on the proper sheet and gives rise [see Eq. (2.1)] to the discrete sum of trapped modes and to the continuum of radiation modes, which represents the branch cut contribution. This continuum is characteristic of the unboundedness of the modal problem and is difficult to manipulate from a mathematical point of view. In elastodynamics, there are two continua instead of one because two transverse wavenumbers occur (longitudinal and shear waves) [5, 71]. The continua can actually be approximated with a convenient discrete set of leaky modes, *e.g.* using the steepest descent method [10, 11]. This approximation is valid in a zone restricted near the core, in which leaky modes can provide useful practical information such as axial attenuation and travelling velocity of waves packets [4].

In Ref. [41] (see Chap. 1 of this thesis), the authors have shown that when the surrounding medium is modified by an infinite PML, the forced response can theoretically be obtained with a modal expansion on trapped modes, revealed leaky modes and two continua of radiation modes related to the PML branch cuts. With numerical methods, the PML must yet be truncated to a finite thickness. The continua are then transformed into discrete sets of PML modes. It remains necessary to investigate the use of the so-obtained numerical modes to compute the forced response, based on an appropriate orthogonality relationship to guarantee the uniqueness of the solution. It is of particular interest to derive a general orthogonality relationship that remains applicable for a wide class of problems, including viscoelastic materials, full anisotropy and 3D waveguides of arbitrary cross-section. Moreover, it is necessary to clarify the contribution and the physical relevance of leaky and PML modes in the solution of the problem.

The aim of this chapter is to compute the forced response of elastic open waveguides with a modal approach based on a waveguide formulation combined with a PML. This approach will be termed PML waveguide formulation in this chapter. It is briefly recalled in Sec. 2.1.2. Then, the modal approach used to compute the forced response is presented in Sec. 2.2. A general biorthogonality relationship is derived for the modes of the PML waveguide formulation. A validation test case is presented by considering a fully homogenous medium in Sec. 2.3. Results are compared with an analytic solution, which allows understanding how the PML parameters act on PML modes together with the accuracy of the solution. Section 2.4 shows numerical results obtained for a circular bar waveguide (widely encountered in civil engineering). Time-domain results are obtained, which enables to clearly identify the distinctive role of PML modes and leaky modes and their ability to approximate the total field. An open square bar example is finally considered, in order to show the ability of the approach to handle three-dimensional waveguide problems.

2.1.2 PML waveguide formulation for mode computation

This section briefly recalls the PML waveguide formulation to compute the eigenmodes of an open waveguide [12, 13]. One considers an elastic open waveguide, where z is the propagation axis of the waveguide. The core of the waveguide has an arbitrary cross-section. It is embedded in an infinite medium. Small strains and displacements are assumed. A time-harmonic dependence $\mathrm{e}^{-\mathrm{j}\omega t}$ is chosen. The elastodynamic equilibrium equations are written as:

$$\tilde{\nabla}.\tilde{\sigma}(\tilde{\mathbf{u}}) + \tilde{\rho}\omega^2\tilde{\mathbf{u}} = \tilde{\mathbf{f}}, \tag{2.2}$$

where $\tilde{\mathbf{u}}$ is the displacement vector field. The tilde notation is explained in the following with the PML introduction. $\tilde{\sigma}(\tilde{\mathbf{u}})$ is the stress tensor. The stress-strain relation is $\tilde{\sigma}(\tilde{\mathbf{u}}) = \tilde{C} : \tilde{\epsilon}(\tilde{\mathbf{u}})$, where $\tilde{C}$ is the stiffness tensor (complex for viscoelastic materials). The strain-displacement relation is $\tilde{\epsilon}(\tilde{\mathbf{u}}) = (\nabla\tilde{\mathbf{u}} + (\nabla\tilde{\mathbf{u}})^{\mathrm{T}})/2$. The superscript T denotes the transpose. $\tilde{\mathbf{f}}$ is the vector of volumic forces.

For numerical purpose, the infinite surrounding medium is truncated by a finite PML of thickness h. A radial PML is introduced by analytic continuation [49] of the elastodynamic equations (2.2) into the complex transverse coordinate $\tilde{r}$:

$$\tilde{r}(r) = \int_0^r \gamma(\xi)\mathrm{d}\xi. \tag{2.3}$$

Note that a Cartesian PML could be used instead of a radial PML [13], as done in Sec. 2.4.5. The function $\gamma(r)$ is a user-defined complex-valued function for absorbing outgoing waves in the surrounding medium, such that:

- $\gamma(r) = 1$ outside the PML region ($r < d$),
- $\mathrm{Im}(\gamma(r)) > 0$ inside the PML region ($d < r < d + h$).

d is the position of the PML interface. A boundary condition is arbitrarily applied at the end of the PML. In this thesis, a Dirichlet condition is used. Eq. (2.2) must be transformed to go back to the real radial direction r. The change of variable $\tilde{r} \mapsto r$ for any function $\tilde{g}(\tilde{r})$ gives:

$$\tilde{g}(\tilde{r}) = g(r),\ \mathrm{d}\tilde{r} = \gamma(r)\mathrm{d}r,\ \frac{\partial \tilde{g}}{\partial \tilde{r}} = \frac{\partial g}{\partial r}\frac{1}{\gamma(r)}. \tag{2.4}$$

Following the waveguide formulation in closed waveguides [12, 13], the strain-displacement relation can be written as:

$$\boldsymbol{\epsilon} = (\mathbf{L}_S + \mathbf{L}_z \frac{\partial}{\partial z})\mathbf{u}, \tag{2.5}$$

where $\boldsymbol{\epsilon}$ is the strain vector and $\mathbf{u}$ the displacement vector. $\mathbf{L}_S$ is the operator containing all terms but derivatives with respect to the z-axis, and $\mathbf{L}_z$ is the operator of z-derivatives. The operator $\mathbf{L}_S$ includes derivatives with respect to r and hence it depends on $\gamma(r)$ and $\tilde{r}$ [13]. A FE discretization is then applied to the cross-section (spectral elements can be equally used [32]). The displacement on each element can be written $\mathbf{u}^e(x, y, z, \omega) = \mathbf{N}^e(x, y)\mathbf{U}^e(z, \omega)$, where $\mathbf{N}^e(x, y)$ is the matrix of two-dimensional interpolation functions and $\mathbf{U}^e(z, \omega)$ is the vector of nodal displacements. The derivation of the weak formulation of Eq. (2.2) yields the global matrix system:

$$(\mathbf{K}_1 - \omega^2\mathbf{M})\mathbf{U} + (\mathbf{K}_2 - \mathbf{K}_2^{\mathrm{T}})\mathbf{U}_{,z} - \mathbf{K}_3\mathbf{U}_{,zz} = \mathbf{F}, \tag{2.6}$$

with the element matrices:

$$\begin{aligned}
&\mathbf{K}_1^e = \int \mathbf{N}^{e\mathrm{T}}\mathbf{L}_S^{\mathrm{T}}\mathbf{C}\mathbf{L}_S\mathbf{N}^e\frac{\tilde{r}\gamma}{r}\mathrm{d}S,\ \mathbf{K}_2^e = \int \mathbf{N}^{e\mathrm{T}}\mathbf{L}_S^{\mathrm{T}}\mathbf{C}\mathbf{L}_z\mathbf{N}^e\frac{\tilde{r}\gamma}{r}\mathrm{d}S,\\
&\mathbf{K}_3^e = \int \mathbf{N}^{e\mathrm{T}}\mathbf{L}_z^{\mathrm{T}}\mathbf{C}\mathbf{L}_z\mathbf{N}^e\frac{\tilde{r}\gamma}{r}\mathrm{d}S,\ \mathbf{M}^e = \int \rho\mathbf{N}^{e\mathrm{T}}\mathbf{N}^e\frac{\tilde{r}\gamma}{r}\mathrm{d}S,\ \mathbf{F}^e = \int \mathbf{N}^{e\mathrm{T}}\mathbf{f}\frac{\tilde{r}\gamma}{r}\mathrm{d}S.
\end{aligned} \tag{2.7}$$

where $\mathbf{C}$ is the stiffness matrix defined from Voigt notation of the tensor C.

A spatial Fourier transform in the z-direction is applied to Eq. (2.6), which leads to the PML waveguide formulation [12, 13]:

$$\left(\mathbf{K}_1 - \omega^2\mathbf{M} + \mathrm{j}k(\mathbf{K}_2 - \mathbf{K}_2^{\mathrm{T}}) + k^2\mathbf{K}_3\right)\hat{\mathbf{U}} = \hat{\mathbf{F}}, \tag{2.8}$$

where $\hat{\mathbf{U}}(k, \omega)$ is the vector of nodal displacements, $\hat{\mathbf{F}}$ is the vector of nodal forces and k is the axial wavenumber with the following notation for any function $g(z)$:

$$\hat{g}(k) = \int_{-\infty}^{+\infty} g(z)\mathrm{e}^{-\mathrm{j}kz}\mathrm{d}z. \tag{2.9}$$

Further details of the derivation can be found in Refs. [12, 13]. For the chapter self-containedness, additional steps are given in Appendix 2.A for an axisymmetric open waveguide, which will be used for most of the numerical results presented in Secs. 2.3 and 2.4.

The source term in Eq. (2.8) is dropped (*i.e.* $\hat{\mathbf{F}} = 0$). The source-free problem gives a quadratic eigenvalue problem in terms of k. The eigenproblem is linearized (see Appendix 2.B) and solved for each angular frequency ω. The matrices $\mathbf{K}_1$, $\mathbf{K}_3$ and $\mathbf{M}$ are symmetric. From this property, it can be shown that the eigenspectrum is made of symmetric pairs of eigenvalues and eigenvectors, $(k_m, \mathbf{U}_m)$ and $(-k_m, \mathbf{U}_m^-)$, $(m = 1, \ldots, M)$, representing M positive-going modes and M negative-going modes respectively. In the following, the negative-going modes will be denoted $(k_{-m}, \mathbf{U}_{-m})$.

As recalled in Sec. 2.1.1, the PML waveguide formulation gives three kinds of eigenmodes: trapped modes (if any), leaky modes and the so-called PML modes. PML parameters have a strong influence on the accuracy of trapped and leaky modes. Theoretically (see *e.g.* Refs. [12, 13]), leaky modes are attenuated by the PML if:

$$\arg(k_{l/s}) > -\arg(\hat{\gamma}), \tag{2.10}$$

where $k_{l/s}$ is the longitudinal or shear transverse wavenumber and $\hat{\gamma}$ is the average value of $\gamma(r)$ inside the PML region. When the condition (2.10) is fulfilled, only small reflections occur at the end of a thick enough PML. As usual with PML, the attenuation rate should not be too high to be properly approximated by the FE discretization. Concerning trapped modes, the PML can accentuate their natural transverse decay if $\mathrm{Re}(\hat{\gamma}) > 1$ [12, 13]. As for PML modes, these modes mainly resonate inside the PML and fully depend on PML parameters.

2.2 Forced response of an elastic open waveguide

Any arbitrary field in a waveguide can be expanded on a unique set of modes, provided that these modes are orthogonal [40]. In elastic open waveguides, orthogonality relationships theoretically hold between trapped modes and radiation modes, see *e.g.* Ref. [3, 5]. However, the continua of radiation modes are difficult to manipulate. Conversely, leaky modes form a discrete set, which may approximate the radiation field [16, 72, 73] and which is easier to handle. However, they cannot satisfy orthogonality relationships [7, 72], as they theoretically grow to infinity in the transverse direction (as recalled in Eq. (2.1), leaky modes do not belong to the theoretical modal basis). In this section, a general orthogonality relationship is derived when a finite PML is introduced to close the open problem.

2.2.1 Effects of a PML on the modal basis

In a recent work (see Chap.1 of this thesis), the authors have studied the modal basis of an elastic open waveguide when the surrounding medium is replaced by an infinite PML. It has been shown that the introduction of an infinite PML of constant attenuation profile γ modifies the transverse wavenumbers and yields a rotation of branch cuts by an angle of $-\arg(\gamma)$. The rotation of the branch cuts induces a partial access to the initial improper sheets where leaky modes occur. Therefore with a PML, a discrete set of revealed leaky modes must be included in the modal basis. The set of trapped modes is left unchanged and the solution field with an infinite PML can hence be written:

$$\mathbf{u}(\mathbf{r},\omega) = \sum \text{trapped modes} + \sum \text{revealed leaky modes} + \int \text{PML branch cuts}. \tag{2.11}$$

The solution field described by Eq. (2.11) remains physically valid only in the region out of the PML ($r < d$).

With numerical methods, the PML must be truncated to a finite thickness. The continuous sums related to the PML branch cuts are then discretized [12, 13, 15]. These discretized sets are PML modes, non-intrinsic to the physics since they fully depend on the parameters of the truncated PML and on the boundary condition applied at the end of the PML. Therefore, the role of these sets in the convergence of the modal expansion might be questionable at first sight. This topic will be addressed in Sec. 2.3 through numerical results.

2.2.2 Derivation of a biorthogonality relationship

Let us start from the linear eigenvalue problem (see Appendix 2.B), written for a mode m:

$$(\mathbf{A} - k_m\mathbf{B})\mathbf{x}_m = \mathbf{0}, \tag{2.12}$$

with $\mathbf{x}_m^{\mathrm{T}} = [\mathbf{U}_m^{\mathrm{T}}\ k_m\mathbf{U}_m^{\mathrm{T}}]^{\mathrm{T}}$. $\mathbf{A}$ is not symmetric, and then left eigenvectors must be considered [74]. The left eigenvector $\mathbf{y}_n$ satisfies the eigensystem:

$$\mathbf{y}_n^{\mathrm{T}}(\mathbf{A} - k_n\mathbf{B}) = \mathbf{0}. \tag{2.13}$$

The left and right eigenvectors are related by the following general biorthogonality relationships:

$$\mathbf{y}_n^{\mathrm{T}}\mathbf{B}\mathbf{x}_m = b_m\delta_{mn}, \quad \mathbf{y}_n^{\mathrm{T}}\mathbf{A}\mathbf{x}_m = k_m b_m\delta_{mn}, \tag{2.14}$$

where b_m is a normalization factor and δ_{mn} is the Kronecker' symbol. $\mathbf{B}$ is symmetric, and from Eq. (2.13), the left eigenvector $\mathbf{y}_m$ satisfies:

$$(\mathbf{A}^{\mathrm{T}} - k_m\mathbf{B})\mathbf{y}_m = \mathbf{0}. \tag{2.15}$$

It can be checked that the above eigensystem is satisfied with:

$$\mathbf{y}_m^{\mathrm{T}} = [\mathbf{U}_{-m}^{\mathrm{T}}\ k_m\mathbf{U}_{-m}^{\mathrm{T}}]^{\mathrm{T}}. \tag{2.16}$$

The left eigenvectors can then be directly related to the right eigenvectors. This avoids to solve the left eigenproblem. Hence, from Eq. (2.40) the biorthogonality relationship $\mathbf{y}_n^{\mathrm{T}}\mathbf{B}\mathbf{x}_m = b_m\delta_{mn}$ can be expanded as:

$$\mathbf{U}_{-n}^{\mathrm{T}}(\mathbf{K}_1 - \omega^2\mathbf{M})\mathbf{U}_m + k_n k_m\mathbf{U}_{-n}^{\mathrm{T}}\mathbf{K}_3\mathbf{U}_m = b_m\delta_{mn}. \tag{2.17}$$

From Eq. (2.41) written for a given mode m, one gets $(\mathbf{K}_1 - \omega^2\mathbf{M})\mathbf{U}_m = -\mathrm{j}k_m(\mathbf{K}_2 - \mathbf{K}_2^{\mathrm{T}})\mathbf{U}_m - k_m^2\mathbf{K}_3\mathbf{U}_m$. Eq. (2.17) can then be rewritten as:

$$\mathrm{j}k_m\mathbf{U}_{-n}^{\mathrm{T}}(\mathbf{K}_2^{\mathrm{T}} + \mathrm{j}k_m\mathbf{K}_3)\mathbf{U}_m - \mathrm{j}k_m\mathbf{U}_{-n}^{\mathrm{T}}(\mathbf{K}_2 - \mathrm{j}k_n\mathbf{K}_3)\mathbf{U}_m = b_m\delta_{mn}. \tag{2.18}$$

In Eq. (2.18), one can identify the so-called modal forces [75]:

$$\mathbf{F}_m = (\mathbf{K}_2^{\mathrm{T}} + \mathrm{j}k_m\mathbf{K}_3)\mathbf{U}_m, \tag{2.19}$$

such that after rearrarengement, Eq. (2.18) yields:

$$\frac{\mathrm{j}\omega}{4}(\mathbf{U}_m^{\mathrm{T}}\mathbf{F}_{-n} - \mathbf{U}_{-n}^{\mathrm{T}}\mathbf{F}_m) = Q_{m,-m}\delta_{mn}, \tag{2.20}$$

with $Q_{m,-m} = -\omega b_m/4k_m$. Eq. (2.20) provides a general orthogonality relationship involving the whole cross-section of the waveguide (*i.e.* including the finite PML). It is applicable to any kind of modes without distinction (trapped, leaky and PML modes).

This orthogonality relationship is identical to the orthogonality relationship derived for lossy closed waveguides in [75]. It remains valid for 3D waveguides of arbitrary cross-section, as well as for fully anisotropic and viscoelastic materials (it is noteworthy that

Eq. (2.20) is also applicable with absorbing viscoelastic layers, see *e.g.* results in Ref. [75]). As shown in this reference, Eq. (2.20) can be readily expressed in an analytical form:

$$Q_{m,-n} = \frac{\mathrm{j}\omega}{4}\int_S (\mathbf{u}_m \cdot \mathbf{t}_{-n} - \mathbf{u}_{-n} \cdot \mathbf{t}_m)\mathrm{d}S = 0, \text{ if } m \neq n, \tag{2.21}$$

where for each mode, $\mathbf{t}_m$ is the traction vector applied on the section S. Actually, Eq. (2.21) corresponds to Auld's real orthogonality relationship [40], which could therefore be used for the analytical modelling of open waveguides truncated by a finite PML. Note that except for real wavenumber modes (perfectly guided modes or trapped modes), $Q_{m,-m}$ differs from the averaged power flow P_m [75]. The averaged power flow can yet be computed from the Poynting vector of each mode from Eq. (2.29).

As a side remark, a mathematically exact orthogonality relationship has been proposed in Ref. [72] for leaky modes in dielectric waveguides by deforming the radial coordinate into the complex plane. The approach of the present chapter, applied to elastodynamics, is quite similar.

2.2.3 Modal solution of the problem

Let us consider the excitation of the waveguide by a force. The linear formulation [see Eq. (2.39)] is premultiplied by $\mathbf{y}_n^{\mathrm{T}}$ and the vector $\mathbf{x}$ is decomposed on $2M$ modes as follows: $\mathbf{x} = \sum_{-M}^{M} \alpha_m \mathbf{x}_m$ $(m \neq 0)$. The system is then expanded and, thanks to the biorthogonality relation (2.20), it can be checked that the modal coefficients are given by $\alpha_m = -\omega \mathbf{U}_{-m}^{\mathrm{T}}\hat{\mathbf{F}}/[4Q_{m,-m}(k_m - k)]$. Hence, the displacement solution to the forced response problem is:

$$\hat{\mathbf{U}} = -\sum_{\substack{m=-M \\ m\neq 0}}^{+M} \frac{\omega \mathbf{U}_{-m}^{\mathrm{T}}\hat{\mathbf{F}}}{4Q_{m,-m}(k_m - k)}\mathbf{U}_m. \tag{2.22}$$

Then, the inverse Fourier transform $\mathbf{U}(z,\omega) = 1/(2\pi)\int_{\infty}^{+\infty}\hat{\mathbf{U}}(k,\omega)\mathrm{e}^{\mathrm{j}kz}\mathrm{d}k$ is used to go back to the real space (z,ω). With the help of Cauchy's residue theorem, it can be shown that the field outside the source region going towards the positive z direction is [75]:

$$\mathbf{U}(z,\omega) = \sum_{m=1}^{M} \mathbf{E}_m \hat{\mathbf{F}}(k_m)\mathrm{e}^{\mathrm{j}k_m z}, \tag{2.23}$$

where $\mathbf{E}_m$ is the generalized modal excitability matrix:

$$\mathbf{E}_m = \frac{\mathrm{j}\omega}{4Q_{m,-m}}\mathbf{U}_m\mathbf{U}_{-m}^{\mathrm{T}}. \tag{2.24}$$

$(\mathbf{E}_m)_{ij}$ is the displacement amplitude of mode m at degree of freedom (dof) i when excited by a unit force at dof j. If one is interested in the field going towards the negative z direction, then the summation in Eq. (2.23) must be performed on negative-going modes. The $+\mathrm{j}$ factor in Eq. (2.24) is replaced by $-\mathrm{j}$ and the subscripts m and $-m$ are switched.

Finally, the time-transient displacement is obtained by the inverse Fourier transform $1/(2\pi)\int_{\infty}^{+\infty}\mathbf{U}(z,\omega)\mathrm{e}^{-\mathrm{j}\omega t}\mathrm{d}\omega$.

2.2.4 Determination of the travelling direction

The solution given by Eq. (2.23) requires to determine the travelling direction of each mode. Modal characteristics can be computed straightforwardly from the eigensolutions $(k_m, \mathbf{U}_m)$ and the finite element matrices [13]. The phase velocity of a mode m is:

$$v_{p_m} = \frac{\omega}{\mathrm{Re}(k_m)}. \tag{2.25}$$

Its attenuation in $\mathrm{dB\,m^{-1}}$is:

$$\eta_m = 8.686\mathrm{Im}(k_m). \tag{2.26}$$

The group velocity $v_{g_m} = \partial\omega/\partial k_m$ is computed as follows:

$$v_{g_m} = \mathrm{Re}\left[\left(\frac{2\omega\mathbf{U}_{-m}^{\mathrm{T}}\mathbf{M}\mathbf{U}_m}{\mathbf{U}_{-m}^{\mathrm{T}}(\mathrm{j}(\mathbf{K}_2 - \mathbf{K}_2^{\mathrm{T}}) + 2k_m\mathbf{K}_3)\mathbf{U}_m}\right)^{-1}\right]. \tag{2.27}$$

The phase velocity does not necessarily give the travelling direction owing to the existence of backward modes, which have phase and group velocities of opposite sign [40]. The direction of propagation of the modes can be properly determined according to the following criterion:

- the sign of $\mathrm{Im}(k_m)$ if $\mathrm{Im}(k_m) \neq 0$, such that if $\mathrm{Im}(k_m) > 0$, the mode is a positive-going mode, and if $\mathrm{Im}(k_m) < 0$ the mode is negative-going,
- the sign of v_{g_m} if $k_m \in \mathbb{R}$ (that is for trapped modes, when they exist).

The case of trapped modes is somehow particular. The case of purely trapped modes never occurs in viscoelastic media since the wavenumbers always have a non zero imaginary part. In purely elastic waveguides, trapped waves exist only if the shear velocity is lower in the core than in the embedding medium, unless longitudinal and shear waves couple into interface trapped waves, called Stoneley waves [1].

2.2.5 Remarks on the energy velocity

In lossy waveguides, it has been shown that the group velocity can yield non-physical values [76], so that the energy velocity is usually preferred in closed waveguides. However, the energy velocity must be averaged on the whole cross-section, which is theoretically unbounded considering open waveguides.

For trapped modes, which are non-attenuated waves that exponentially decay in the transverse direction, the group velocity is equal to the energy velocity. Hence, the criterion proposed in Section 2.2.4 to determine their travelling direction is consistent (it does not matter whether the group velocity or the energy velocity is used).

For leaky modes, the energy velocity cannot be theoretically defined because these modes grow to infinity in the transverse directions. In practice, the energy velocity integration of leaky modes is usually restricted to the core, which can give a reasonable approximation of the velocity of wave packets [4, 76]. The energy velocity restricted to the core cross-section can be calculated as follows:

$$v_{e_m} = \frac{\mathrm{Re}(P_m)}{\mathrm{Re}(T_m) + \mathrm{Re}(V_m)}, \tag{2.28}$$

Material	ρ (kg m^{-3})	c_l (m s^{-1})	c_s (m s^{-1})	η_l (Np wavelength^{-1})	η_s (Np wavelength^{-1})
Cement grout	1600	2810	1700	0.043	0.1
Steel	7932	5960	3260	0.003	0.008

Table 2.1 – Material properties

where for each mode m, P_m is the normal component of the Poynting vector integrated on the core cross-section, T_m is the core cross-section and time-averaged kinetic energy, and V_m is the core cross-section and time-averaged potential energy. These quantities can be post-processed from [13]:

$$P_m = \frac{-\mathrm{j}\omega}{2}\overline{\mathbf{U}}_m^*(\overline{\mathbf{K}}_2^{\mathrm{T}} + \mathrm{j}k_m\overline{\mathbf{K}}_3)\overline{\mathbf{U}}_m, \tag{2.29}$$

$$T_m = \frac{\omega^2}{4}\overline{\mathbf{U}}_m^*\overline{\mathbf{M}}\overline{\mathbf{U}}_m, \tag{2.30}$$

$$V_m = \frac{1}{4}\overline{\mathbf{U}}_m^*(\overline{\mathbf{K}}_1 + \mathrm{j}k_m\overline{\mathbf{K}}_2 - \mathrm{j}k_m^*\overline{\mathbf{K}}_2^{\mathrm{T}} + k_m^*k_m\overline{\mathbf{K}}_3)\overline{\mathbf{U}}_m. \tag{2.31}$$

where the * superscript denotes conjugate transpose and the overbar stands for the dof restriction to the core cross-section.

It is noteworthy that the integration restriction to the core is quite arbitrary. Therefore, the so-defined energy velocity cannot be considered as a general indicator to determine the travelling direction of any type of modes (of PML modes, in particular). In the following of this chapter, the above-defined energy velocity will be only used for the post-processing of dispersion curves of leaky modes and their comparison with literature results.

2.3 The homogeneous test case

In this section, the forced response of a homogenous medium excited by a point load is computed by the numerical method and compared to an analytical solution. A homogeneous medium can be viewed as an open waveguide without a core. This test case is actually the worst scenario for the numerical modal approach since there is no contrast of impedance: only the discrete set of PML modes occurs (there is neither trapped nor leaky modes). As outlined in Section 2.2.1, the contribution of PML modes to the solution has to be clarified because these modes are not intrinsic to the physics (they mainly oscillate in the PML region, which mainly depends on user-defined parameters).

2.3.1 Description

Let us assume a homogeneous, isotropic and unbounded medium, made of cement grout material (see Fig. 2.1). Material properties are given in Table 2.1. In this section, the medium is pure elastic ($\eta_l = \eta_s = 0$). The medium is excited by a point force in the z-direction at the origin: $\mathbf{f} = F(t)\delta(\mathbf{x})\mathbf{e_z}$ ($\mathbf{f} = \frac{F(t)}{2\pi r}\delta(r)\delta(z)\mathbf{e_z}$ in cylindrical coordinates). The signal $F(t)$ is a sinus of centre frequency f_c = 60 kHz with an amplitude of 1 N, modulated over 5 cycles by a Hanning window.

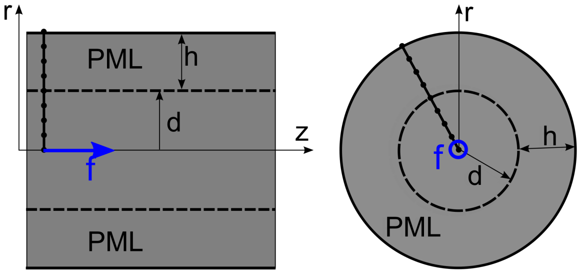

Figure 2.1 – Sketch of the excited homogeneous medium truncated by a finite PML.

The transient axial displacement along the z-axis (*i.e.* at $r = 0$) at a distance z to the source is given by the following analytical solution (see *e.g.* Ref. [14]):

$$u_z^{\mathrm{ref}}(z,t) = \frac{1}{2\pi\rho z^3}\int_{z/c_l}^{z/c_s} \tau F(t-\tau)\mathrm{d}\tau + \frac{1}{4\pi\rho c_l^2 z}F(t-\frac{z}{c_l}). \tag{2.32}$$

The first term of Eq. (2.32) is a near-field contribution. The second term is the far-field contribution of the P-wave (along the z-axis, there is no far-field contribution of the S-wave [14]).

The problem is solved with an axisymmetrical PML waveguide formulation (see Appendix 2.A). The PML starts at $r = d = 10$ mm. Following Refs. [12, 13], the attenuation function of the PML is chosen as parabolic and is given by:

$$\gamma(r) = \begin{cases} 1 & \text{if} \quad r \leq d, \\ 1 + 3(\hat{\gamma}-1)\left(\dfrac{r-d}{h}\right)^2 & \text{if} \quad r > d, \end{cases} \tag{2.33}$$

where $\hat{\gamma} = \frac{1}{h}\int_d^{d+h}\gamma(\xi)\mathrm{d}\xi$ is the average value of $\gamma(r)$ inside the PML region. $\hat{\gamma}$ and h are user-defined parameters. The solution is computed in the frequency range $[0, f_{\max}]$, with $f_{\max} = 120$ kHz, divided into 176 frequency steps. The cross-section is discretized with three-nodes line elements of length $\Delta r = 0.25d \approx \lambda_{min}/5$, where $\lambda_{\min} = c_s/f_{\max}$. The eigenproblem (2.42) is solved with the ARPACK library [77]. Based on an implicit restarted Arnoldi method, this library enables to compute a user-defined number of eigenvalues (denoted as $2M$) that are the closest in absolute value to a user-defined shift, set to 0 in this chapter (except in Sec. 2.4.5). The displacement at the FE node located at $r = 0$ is then computed from Eq. (2.23) and denoted as $u_z^{\mathrm{num}}(z,\omega)$. The modal expansion (2.23) contains PML modes only.

The accuracy of the numerical solution is assessed as a function of the distance z with the following relative error in the L2-norm:

$$e(z) = \sqrt{\frac{\int |u_z^{\mathrm{ref}}(z,\omega) - u_z^{\mathrm{num}}(z,\omega)|^2\mathrm{d}\omega}{\int |u_z^{\mathrm{ref}}(z,\omega)|^2\mathrm{d}\omega}}, \tag{2.34}$$

where $u_z^{\mathrm{ref}}(z,\omega)$ is obtained from the analytic Fourier transform of Eq. (2.32), given in Appendix 2.C (from Parseval's equality, the relative error has the same value both in frequency and time domains).

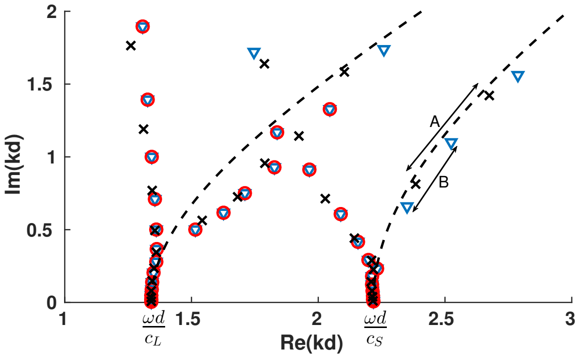

Figure 2.2 – Wavenumber spectrum of an elastic homogeneous medium computed with the PML waveguide formulation at $f = f_c$. PML parameters: $\hat{\gamma} = 4 + 4\text{j}$; blue triangle: $h = 4d$, $M = 50$; red circle: $h = 4d$, $M = 30$; black cross: $h = 3d$, $M = 50$. Dashed black line: theoretical branch cut rotated by $-\arg(d + h\hat{\gamma})$ with $h = 4d$.

2.3.2 Results

Figure 2.2 represents the discrete modal spectrum in the complex wavenumber kd-plane ($\text{Re}(kd) > 0, \text{Im}(kd) > 0$) at the centre frequency, computed for $\hat{\gamma} = 4 + 4\text{j}$ and the following three cases: $(h = 4d, M = 50)$, $(h = 4d, M = 30)$ and $(h = 3d, M = 50)$. This enables to study the influence of two key features on the relative error of the forced response:

- the complex thickness $d + \hat{\gamma}h$,
- the number of modes M retained in the modal expansion.

The number of dofs of the quadratic eigenvalue problem is equal to 68 dofs for $h = 3d$ and 84 dofs for $h = 4d$. These values must be multiplied by two for the linearized eigenvalue problem (see Appendix 2.B).

As observed in Fig. 2.2, the poles close to the real axis ($\text{Im}(kd) = 0$) lie along two hyperbolas, corresponding to the branch cuts rotated by the PML. As briefly recalled in Sec. 2.2.1, these branch cuts are rotated by an angle equal to $-\arg(\gamma)$ in the case of an infinite PML (for further details, see Chap. 1). For a PML of finite thickness, this angle becomes equal to $-\arg(d + h\hat{\gamma})$ as shown in Ref. [13]. Note that the deviation from the theoretical hyperbolas observed here for high order poles is explained by the FE approximation: this deviation can be moved further away from the real axis by reducing the size of elements (see Ref. [12]).

The relative error of the forced response is plotted in Fig. 2.3 as a function of the distance z. It can be observed that a good accuracy is reached for the three cases in the range $z \in [20d, 90d]$, with a relative error lower than 0.5%. This shows the ability of PML modes, when the PML is properly parametrized, to reconstruct the analytical solution. In particular, the geometrical decay of the field is well recovered by the superposition of PML modes, which are by nature exponentially decaying.

Further away from the source ($z > 90d$), it turns out that the error gets lower by increasing the complex thickness (compare red and blue results with the black ones). As shown in previous studies [12, 13], the discretization of the continua gets denser as the complex thickness increases. This effect can be observed in Fig. 2.2 (see *e.g.* the distance labelled

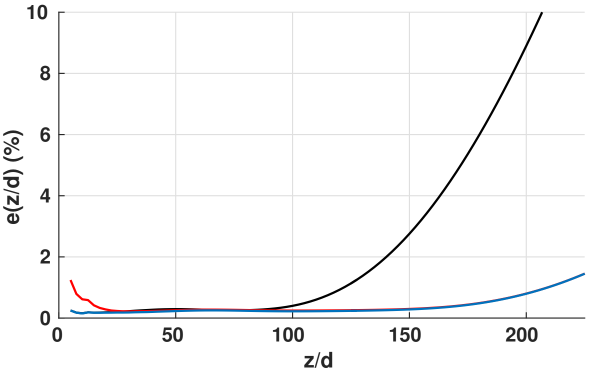

Figure 2.3 – Relative error as a function of the distance z between PML waveguide formulation and analytical solutions. Same parameters and color legend as in Fig. 2.2.

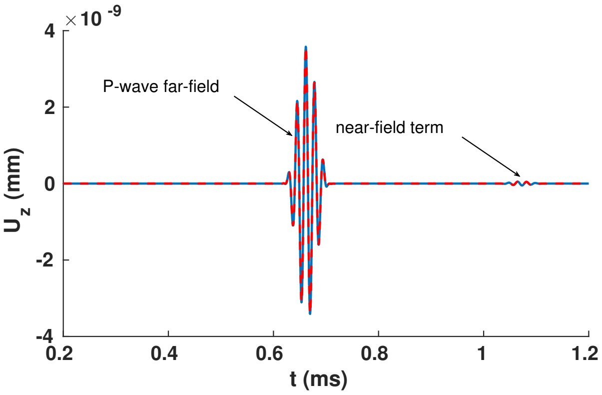

Figure 2.4 – Transient axial displacement calculated at a distance $z = 175d$ with the PML waveguide formulation (dashed red line) and the analytical solution (blue line). Parameters: cement grout, $\hat{\gamma} = 4 + 4\mathrm{j}$, $h = 4d$, $M = 50$.

A and B between two poles for two different complex thicknesses). Indeed, only modes with low $|\mathrm{Im}(kd)|$ can significantly contribute to the forced response at far distances. It is then necessary to have a denser spectrum to reassemble a geometrically decaying solution.

Yet in the near field ($z < 20d$), even highly attenuated PML modes (with high $|\mathrm{Im}(kd)|$) can significantly contribute to the solution. For a given modal density (*i.e.* a given complex thickness), the error can then be reduced by increasing the maximum imaginary part of the computed spectrum, that is to say, the number of modes M retained in the modal expansion (compare blue with red results). Conversely, for a fixed number of modes M, the error in the near field could also be reduced by decreasing the complex thickness.

It has to be mentioned that the numerical results of Fig. 2.3, obtained in this chapter for the elastodynamic problem, are consistent with the theoretical proof of convergence of the PML mode expansion derived in Ref. [15] for the Helmholtz equation.

As an example, Fig. 2.4 compares the transient numerical and analytical solutions calculated at the distance $z = 175d$. Good agreement is found, which confirms the ability of the numerical approach to accurately compute the forced response even in the fully homogeneous configuration (worst scenario). Note that the distance $z = 175d$ will be of interest when considering a core waveguide example as discussed later in Sec. 2.4.

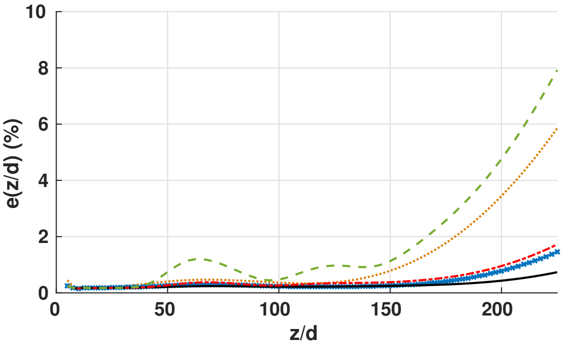

Figure 2.5 – Relative error as a function of distance between PML waveguide formulation and analytical solutions for a complex thickness $25\mathrm{e}^{\mathrm{j}\theta}$. Dotted orange line: $\theta = 20\,\mathrm{deg}$; crossed blue line: $\theta = 30\,\mathrm{deg}$; black line: $\theta = 45\,\mathrm{deg}$; dashed-dotted red line: $\theta = 60\,\mathrm{deg}$; dashed green line: $\theta = 70\,\mathrm{deg}$.

The argument of the complex thickness, denoted as θ ($\theta \in]0, \pi/2[$), also plays a role on the accuracy of the numerical results. Figure 2.5 shows the relative error for different values of θ by keeping constant the modulus of the complex thickness, set to $|d + h\hat{\gamma}| = 25$ ($h = 4d$, $M = 50$). This means that $\hat{\gamma}$ now varies as a function of θ, such that $\mathrm{Im}(\hat{\gamma})$ increases as θ increases and conversely.

Not too far from the source, the error remains low regardless of the value of θ (less than 1.2% for $z/d \in [0, 150d]$). For greater distances, the error increases with a rate depending on θ. The error remains small (below 2%) in a wide range of values ($\theta \in [30, 60]\,\mathrm{deg}$), with a minimum reached around $\theta = 45\,\mathrm{deg}$. Outside this range, the accuracy of the solution decreases because the PML attenuation is not strong enough. More precisely, when the argument is small (*e.g.* $\theta = 20\,\mathrm{deg}$), waves are reflected at the end of the PML ($\mathrm{Im}(\hat{\gamma})$ is too low), which deteriorates the solution. Equivalently, θ must not be too close to $\pi/2$ either (see *e.g.* $\theta = 70\,\mathrm{deg}$), otherwise the rotated branch cuts become too close to the real axis. In this case, the problem becomes equivalent to the computation of trapped modes (these modes occur along the real axis also), and as shown in Ref. [12], a proper transverse attenuation of such modes requires to increase $\mathrm{Re}(\hat{\gamma})$ instead of $\mathrm{Im}(\hat{\gamma})$.

2.4 Application

A steel core is now included in the homogeneous medium previously studied (see Fig. 2.6). First, the core has a circular cross-section. This configuration enables to highlight the contribution of leaky modes, compared to that of PML modes, as a function of the distance to the source. As before, this open waveguide is modelled with the axisymmetrical PML waveguide formulation. Then, a square cross-section is considered as an example of three-dimensional waveguide.

2.4.1 Circular bar test case description

The material properties are given in Table 2.1. The shear wave velocity in the core (steel) is greater than in the embedding medium (cement grout). For this configuration, there is no trapped modes [1, 4], so that only leaky modes and PML modes occur. The core

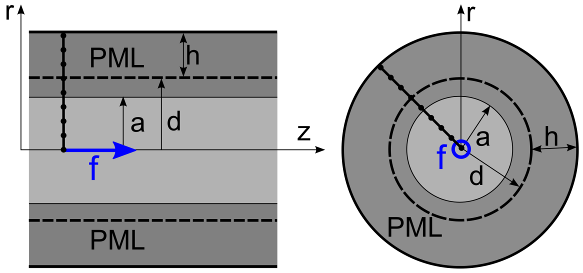

Figure 2.6 – Sketch of the excited steel circular bar embedded into cement grout truncated by a finite PML.

has a radius $a = 10$ mm. Both the elastic and viscoelastic cases will be considered. The embedding medium is truncated by a PML of thickness h starting at a distance $r = d$ with the same attenuation profile as Eq. (2.33). In order to avoid spurious eigenvalues and limit the transverse growth of leaky modes, it is preferable to set the PML close to the core [47] ($d - a$ should be small). The PML interface has been set to $d = a$.

2.4.1.1 Dispersion curves

For the visualisation of dispersion curves, only the modes intrinsic to the physics are of interest (leaky and trapped modes). It is then necessary to filter out PML modes. A filtering criterion has been proposed in previous studies [12, 13] to identify and remove PML modes. A slightly modified version is presented here. The proposed filtering criterion is based on the ratio of the imaginary part over the modulus of the kinetic energy, defined from Eq. (2.30) but integrating the whole cross-section (*i.e.* including the PML, so that the overbar has to be discarded in Eq. (2.30)). The modes are retained in the visualisation if they fulfil the following criterion:

$$1 - \frac{\mathrm{Im}(T_m)}{|T_m|} > \eta_{\min}, \tag{2.35}$$

where $0 < \eta_{\min} < 1$ is a user-defined parameter.

The filtered dispersion curves obtained for the viscoelastic case are shown in Fig. 2.7. The figure shows 12 modes, of leaky type, corresponding to longitudinal modes (these modes are usually labelled L(0,n) in the literature). Also shown are the results of Ref. [4], which confirms the ability of the PML waveguide formulation to accurately compute leaky modes [12, 13, 32].

2.4.1.2 Excitation parameters

The forced response of the open waveguide is computed with the same type of force as in Sec. 2.3, with an amplitude of 1N, considering the following two signals:

- $f_c = 60$ kHz with a 5 cycles Hanning window. At this frequency, only one leaky mode propagates (see point A in Fig. 2.7). This low-frequency excitation allows a direct comparison with the results of Sec. 2.3 and aims to clarify the influence of leaky modes on the solution compared to that of PML modes. The problem is solved on the frequency range $[f_{\min}, f_{\max}]$, with $f_{\min} = 12$ kHz and $f_{\max} = 120$ kHz, divided

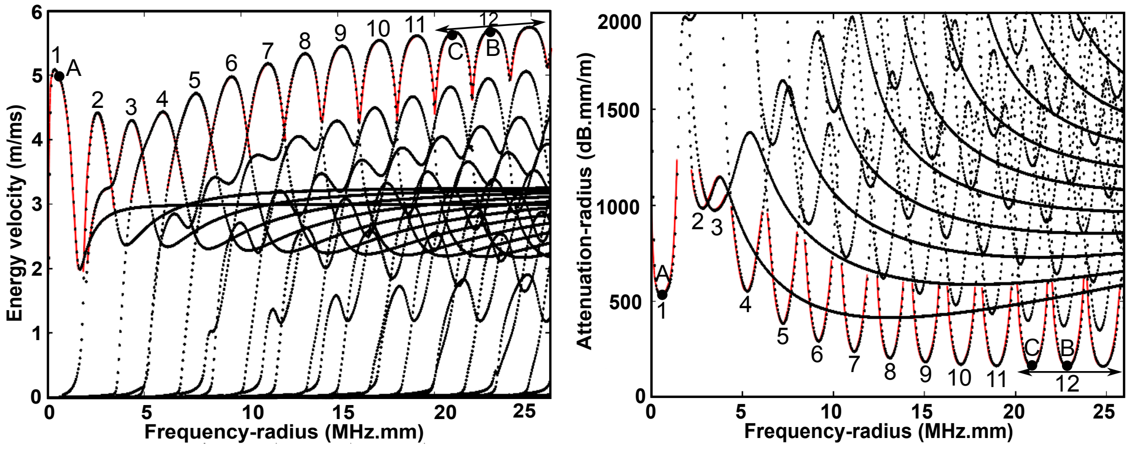

(a) (b)

Figure 2.7 – PML waveguide formulation results (black dots) and results of Ref. [4] (red line) for (a) the energy velocity and (b) the attenuation (steel circular bar embedded into cement grout, viscoelastic case). The PML parameters are: $h = a$, $\hat{\gamma} = 1 + 2\mathrm{j}$. Filtering criterion: $\eta_{\min} = 0.6$. Point A: f = 0.60 MHz mm ; Point B: f = 22.84 MHz mm ; Point C: f = 20.92 MHz mm.

into 323 frequency steps. The size of finite elements is set to $\Delta r = 0.25a$, yielding 84 dofs for the quadratic eigenvalue problem (84x2 for the linearized one).

- $f_c = 2.284$ MHz with a 10 cycles Hanning window. This high-frequency excitation involves several leaky modes and is of interest for NDE because the mode of lowest attenuation is excited (see point B in Fig. 2.7). For this high-frequency excitation, the problem is solved for $[f_{\min}, f_{\max}]$, with $f_{\min} = 1.14$ MHz and $f_{\max} = 3.42$ MHz, divided into 1823 steps. The size of finite elements is set to $\Delta r = 0.019a$, yielding 240 dofs for the quadratic eigenvalue problem (240x2 for the linearized one).

2.4.2 Low frequency response

For the low-frequency excitation ($f_c = 60$ kHz), the PML parameters are set according to the results of Sec. 2.3 in order to ensure a good accuracy of the PML mode contribution ($h = 4a$, $\hat{\gamma} = 4 + 4\mathrm{j}$). As in Sec. 2.3, the axial component u_z of the forced response is computed along the z-axis. 50 PML modes and 1 leaky mode are now included in the modal superposition.

Figure 2.8 shows the transient response at $z/a = 175$ both for the elastic and the viscoelastic cases. As expected, the amplitude of the response is reduced in the viscoelastic case (but the times of flight are nearly unchanged). Three wave packets can be observed. The first one is the contribution of the leaky mode. The second and third packets are the contribution of PML modes (it has been checked that these packets disappear if PML modes are not retained in the modal expansion). Interestingly, the second and third packets can be compared to the results of Fig. 2.4 obtained for the homogeneous test case (*i.e.* without steel core): it can be noticed that the times of flight coincide each other. Therefore, the contribution of PML modes observed in Fig. 2.8, inside the steel core, can be interpreted as the trace of the field radiated into the surrounding medium.

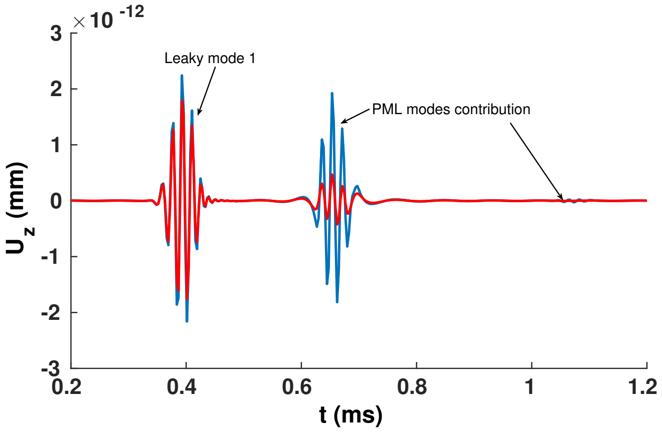

Figure 2.8 – Transient axial displacement $u_z(r = 0, z = 175a, t)$ in a steel-cement grout circular bar open waveguide, in the pure elastic case (blue line) and in the viscoelastic case (red line), for a low-frequency excitation ($f_c = 60$ kHz). PML parameters: $\hat{\gamma} = 4 + 4\text{j}$, $h = 4a$, $M = 51$.

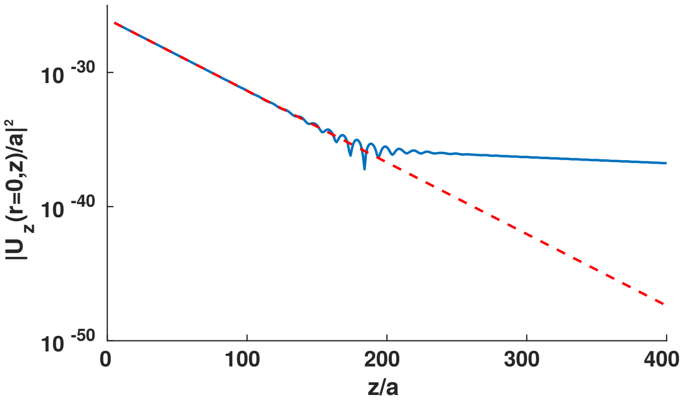

Figure 2.9 – Energy as a function of distance in a steel-cement grout circular bar open waveguide (elastic case). PML parameters: $\hat{\gamma} = 4 + 4\text{j}$, $h = 4a$. Blue line: modal superposition over 50 PML modes and 1 leaky mode ($M = 51$) ; dashed red line: contribution of the leaky mode only (exponential decay).

To confirm this interpretation, Fig. 2.9 plots the quantity proportional to the energy, $|u_z(r = 0, z)|^2$, as a function of the distance z computed at the centre frequency (elastic case). Up to a certain distance ($z/a = 170$), the leaky mode contribution prevails: the energy decreases exponentially. But further away from the source, the leaky mode contribution becomes negligible and the PML mode contribution prevails: the energy decreases with a geometrical decay. In between, there is a transition zone (around $z/a = 175$) where both types of modes contribute nearly equally as can be observed in Fig. 2.8.

Similar results have been obtained analytically in the case of optical scalar waveguides [16], showing that radiation modes first reassemble the leaky mode contribution (exponentially decaying) and then yields the long-term diffraction (geometrically decaying). Provided that the PML parameters are set properly, Fig. 2.8 and 2.9 show that the PML technique enables to compute the long-term diffraction phenomenon. This is not the case with absorbing viscoelastic layers [16].

2.4.3 High frequency response

The NDE of open waveguides requires that enough energy remains inside the core. At high frequencies, the energy can be concentrated into the core and the leakage attenuation reduced [4]. In Fig. 2.7, the lowest attenuation is reached for the 12th leaky mode, with a characteristic series of lobes above 20 MHz mm (the minimum attenuation is reached for the second lobe, at point B, and equals 159 dB mm m^{-1}). At higher frequencies, the attenuation of higher order modes increases because of greater losses due to viscoelasticity than to leakage [4]. Since it can propagate over greater distances than the others, the 12th mode is hence quite attractive.

In the context of NDE, only leaky modes are of interest. The contribution of PML modes (long-term diffraction, geometrically decaying) does not need to be considered because it occurs when a lot of energy has been already lost from the core (that is to say, when the problem can somehow no longer be considered as a waveguide problem). The computational cost can then be reduced here because, for the high-frequency excitation ($f_c = 2.284$ MHz), an acceptable convergence of leaky modes can actually be reached with a thin PML. After numerical tests, the PML thickness has been reduced to $h = 0.1a$ with $\hat{\gamma} = 1 + 2\mathrm{j}$.

Figure 2.10b shows the transient solution at $z/a = 175$. $M = 20$ leaky modes have been used to compute the forced response. Thanks to the modal approach used in this chapter, the contribution of each mode m to the total forced response at a given distance of propagation can be computed. This modal contribution is given by the vector $\mathbf{E}_m \hat{\mathbf{F}}(k_m) \mathrm{e}^{\mathrm{j}k_m z}$ (see Sec. 2.2.3). The so-obtained values are plotted in Fig. 2.10a for the dof corresponding to the axial displacement at $r = 0$, over the energy velocity curves. It shows that the first wave packet is mainly due to the 12th mode with a smaller contribution of the 11th mode. The wave packet of the second arrival is composed of weaker modal contributions, corresponding to parts of dispersion curves having higher attenuation and slower velocity. As expected, the energy is essentially contained in the first arrival because the centre frequency of the excitation coincides with the maximum energy velocity and the minimum attenuation of the 12th mode (point B in Fig. 2.7).

2.4.4 Excitability of leaky modes

In the analysis of elastic waveguides, the excitability of a given mode is an important feature, defined by the displacement-force ratio, which typically enables to optimise the type and location of sensors to be used [78]. The expression of excitability arises from the orthogonality of modes. Yet from a theoretical point of view and as mentioned earlier, leaky modes cannot satisfy an orthogonality relationship because the wave fields of such modes do not vanish at infinity in the transverse direction. To circumvent this problem, some authors have proposed to restrict the integration over the core [7].

However, the PML technique used in this chapter enables to calculate the excitability, as defined from Eq. (2.24), by integrating over the whole cross-section including the PML. Like the biorthogonality relation (2.20), the so-defined excitability is applicable to any type of modes, and in particular to leaky modes.

Figure 2.11 represents the modulus of the excitability over a wide frequency range for an axial point force applied at the centre of the core. For clarity of the figure, the excitability of each mode is shown only in a frequency range where their maximum energy velocity and their minimum attenuation occur (these regions are of low modal dispersion).

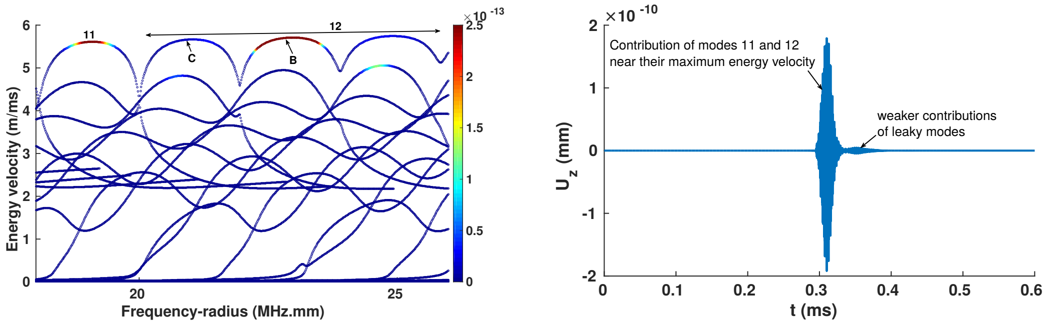

(a) (b)

Figure 2.10 – (a) Energy velocity curves with the modal contribution of axial displacement at r=0 and z=175a at each frequency (colormap) and (b) Transient axial displacement $u_z(r = 0, z = 175a, t)$ in a steel-cement grout circular bar open waveguide (viscoelastic case) for a high-frequency excitation ($f_c = 2.284$ MHz). PML parameters: $\hat{\gamma} = 1 + 2\text{j}$, $h = 0.1a$, $M = 20$.

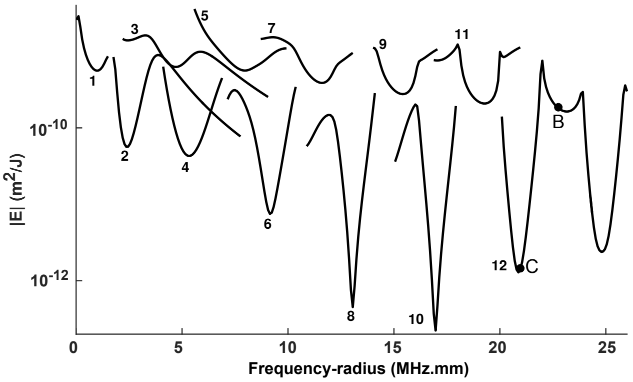

Figure 2.11 – Excitability in a steel-cement grout circular bar open waveguide (viscoelastic case) for a point-force excitation at the core centre oriented in the axial direction. PML parameters: $h = a$, $\hat{\gamma} = 1 + 2\text{j}$.

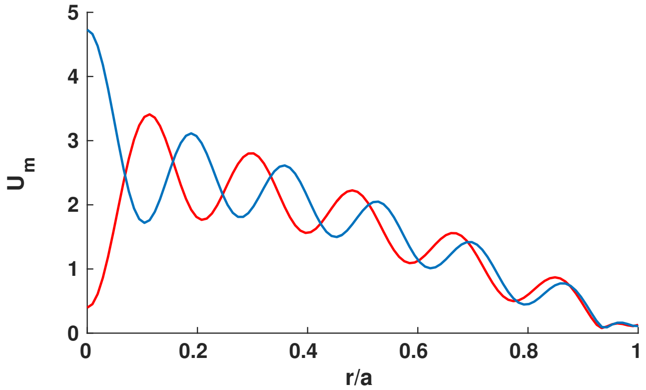

Figure 2.12 – Mode shape $\mathbf{U}_m$ in the z direction of the 12th leaky mode for the first lobe (point C, $f = 20.92$ MHz mm, red line) and for the second lobe (point B, $f = 22.84$ MHz mm, blue line) in a steel-cement grout circular bar open waveguide (viscoelastic case). PML parameters: $\hat{\gamma} = 1 + 2\text{j}$, $h = a$.

The excitability is found to be strong for odd modes (modes 1, 3, 5, 7, 9, 11) and weak for even modes up to the 12th mode. As previously mentioned, the 12th mode is somehow specific as it is composed of a series of lobes. These lobes also exhibit a strong variation of excitability (contrary to the energy velocity and the attenuation). For instance, the excitability of the second lobe (point B) is much higher than the excitability of the first lobe (point C), by an amount of $20 \log_{10} |E_B/E_C| = 42$ dB.

These differences of excitability can be explained by inspecting the mode shapes. As an example, Fig. 2.12 shows the mode shapes of the first two lobes of the 12th mode. The modal displacement of the first lobe is significantly lower at the centre of the core (*i.e.* where the point force is applied), hence reducing the excitability at this point.

2.4.5 A square bar example

A three-dimensional waveguide with a core cross-section of square shape is now considered. As previously mentioned, the theory of Sec. 2.2 remains fully applicable. However, the computational cost significantly increases because the cross-section is now two-dimensional (instead of one-dimensional in the previous test cases). Furthermore, the eigenspectrum contains flexural and torsional leaky modes (in addition to longitudinal modes) and much more PML modes as well. In the following, the forced response of the square bar is computed in a high-frequency range and compared to the circular case.

2.4.5.1 Square bar test case description

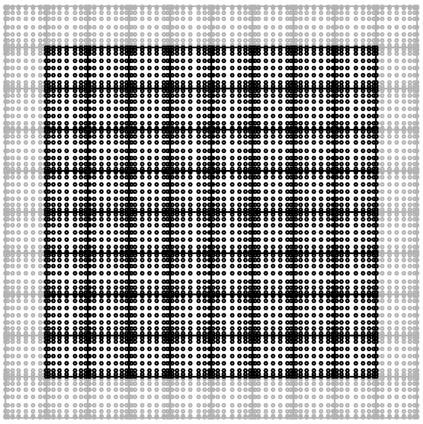

Figure 2.13 – Spectral element mesh (8th order elements) of a square bar (viscoelastic steel) embedded into viscoelastic cement grout. Black: square bar; gray: embedding medium (PML).

The dispersion curves of a square bar open waveguide have already been obtained with a Cartesian PML waveguide formulation discretized with spectral elements in Ref. [32]. The square bar is made of viscoelastic steel and is embedded into viscoelastic cement grout. Materials are given in Table 2.1. The half-width of the square is given by $a = 10$mm. The Cartesian PML is introduced by an analytic continuation of the elastodynamic equations (2.2) into the complex plane $(\tilde{x}, \tilde{y})$. As in the circular bar case, its attenuation is chosen

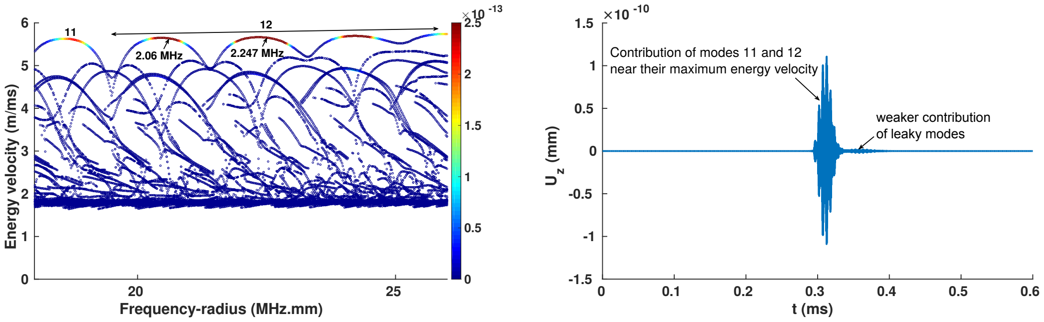

(a) (b)

Figure 2.14 – (a) Energy velocity curves with the modal contribution of axial displacement at r=0 and z=175a at each frequency (colormap) and (b) Transient axial displacement $u_z(r = 0, z = 175a, t)$ in a steel-cement grout square open waveguide (viscoelastic case) for a high-frequency excitation ($f_c = 2.247$ MHz). PML parameters: $\hat{\gamma}_x = \hat{\gamma}_y = 1 + 2\mathrm{j}$, $h_x = h_y = 0.25a$, $M = 50$.

parabolic. The PML parameters are then given in both directions x and y by the mean attenuations $\hat{\gamma}_x$ and $\hat{\gamma}_y$, the thickness h_x and h_y and the distances d_x and d_y. In the following, $d_x = d_y = a$. Details about the implementation of a Cartesian PML can be found in Ref. [13] and are not recalled in this chapter for conciseness. As for spectral elements discretization, the specific element matrices and details about the convergence of the method can be found in Ref. [32]. To reduce the number of computed modes, the eigensolver shift is set to $k_0 = \omega / c_{l0}$, where c_{l0} is the longitudinal bulk velocity in the core. This enables to compute mainly longitudinal modes, while avoiding the computation of PML modes or highly attenuated leaky modes of minor interest [32]. Note that opposite-going modes also have to be computed (using a $-k_0$ shift) to obtain the forced response.

The waveguide is excited by a unit force of 1 N applied at the centre of the square shape in z direction. The excitation signal is a 10 Hanning window with $f_c = 2.247$ MHz. At this frequency, the mode with the lowest attenuation is excited. The problem is then solved for $[f_{\min}, f_{\max}]$, with $f_{\min} = 1.797$ MHz and $f_{\max} = 2.697$ MHz, divided into 542 steps. The half-width of the square is meshed with 4 spectral elements of order 8 (see Fig. 2.13), yielding 20 451 dofs for the quadratic eigenvalue problem (20 451x2 for the linearized one).

2.4.5.2 High-frequency response

As shown in Ref. [32], low-leakage longitudinal modes also occurs in square bars at high frequencies. Herein, the lowest attenuation is reached for the second lobe of the 12th longitudinal mode at $f = 2.247$ MHz and equals $147\,\mathrm{dB\,mm\,m^{-1}}$. These values are in good agreement with the results of Ref. [32]. They have been obtained with the following PML parameters: $h_x = h_y = 0.25a$ and $\hat{\gamma}_x = \hat{\gamma}_y = 1 + 2\mathrm{j}$.

Figure 2.14b shows the transient axial displacement at $z/a = 175$ and the modal contribution are displayed in Fig. 2.14a. $M = 50$ modes have been used to compute the forced response. Because of the symmetry of the source, only longitudinal modes are excited. As in the circular case (Fig. 2.10b), two wave packets propagate in the square bar. The first wave packet is due to the arrivals of the 11th and 12th leaky modes, which are the fastest and the less attenuated ones. The second wave packet contains weaker modal

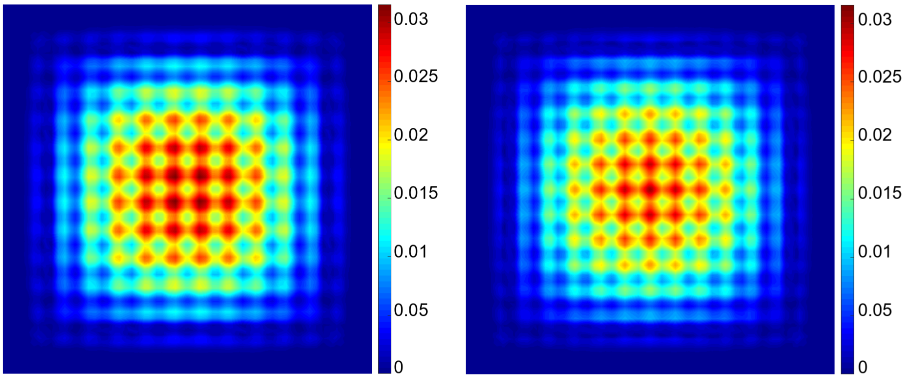

(a) (b)

Figure 2.15 – Mode shape $\mathbf{U}_m$ in the z direction of the 12th longitudinal leaky mode for (a) the first lobe ($f = 2.06$ MHz) (b) the second lobe ($f = 2.247$ MHz) in a steel-cement grout square open waveguide.

contributions of slower velocities.

Note that the wave packets are of slightly smaller amplitudes than in the circular bar. Although the attenuation of the modes is a bit smaller in the square bar, the energy spreads over a wider cross-section area. Moreover, the energy repartition among the modes is also modified. Contrary to the circular case, each lobe of the 12th mode significantly contributes to the response (see Fig. 2.14a). These differences can be explained by the mode shapes of the square bar. The latter are displayed in Fig. 2.15a and Fig. 2.15b for the first two lobes at their lowest attenuation. At the centre of the circular bar, the modal displacement is roughly ten times smaller for the first lobe than for the second lobe (Fig. 2.12). In the square bar, the modal displacement at the centre ($x = y = 0$) is only twice smaller for the first lobe than for the second lobe, hence increasing the modal contribution of the first lobe in the response.

2.5 Conclusion

A modal approach based on PML has been proposed to compute the forced response of elastic open waveguides. Solving the eigenproblem of the PML waveguide formulation leads to three discrete sets of modes: trapped modes, revealed leaky modes and PML modes. The latter comes from a continuous set of modes, discretized by the truncation of the PML, and fully depends on the PML parameters. A biorthogonality relationship has been derived, applicable to any types of modes, which enables to obtain the forced response with a unique modal superposition, as well as to define the excitability of leaky modes.

A numerical study in a homogeneous elastic medium has shown that, despite their dependence on PML parameters and their exponential decay, the contribution of the discrete set of PML modes enables to reassemble the exact solution (geometrically decaying).

In a waveguide, the PML modes enable to obtain the long-term diffraction phenomenon, which occurs at great distances to the source when most energy has leaked into the surrounding medium. However, leaky modes dominate over a wide range of distance inside the core. In this range, leaky modes are sufficient to obtain a good approximation of the solution. Furthermore, the leaky mode contribution remains accurate even with a small PML thickness, hence reducing the computational cost.

Appendices

2.A Axisymmetrical PML waveguide formulation

Let us go back to Eq. (2.2) written in the cylindrical coordinate system $(\tilde{r}, \theta, z)$. The waveguide is axisymmetric, and then the cross-section is reduced to the radial direction $\tilde{r}$. The core of the waveguide has a radius $\tilde{r} = a$, and is made of one or several layers. Only axisymmetric solutions are considered, so that $\partial(.)/\partial\theta = 0$ and $\tilde{u}_\theta = 0$. Hence the displacement field in Eq. (2.2) is expressed as $\tilde{\mathbf{u}} = [\tilde{u}_r \ \tilde{u}_z]^{\mathrm{T}}$, and only depends on the variables $\tilde{r}$ and z.

Based on Eq. (2.3), the change of variable (2.4) is applied to Eq. (2.2). In the strain-displacement relation (2.5), the operators $\mathbf{L}_S$ and $\mathbf{L}_z$ are given by:

$$\mathbf{L}_S = \left(\frac{1}{\gamma} \begin{bmatrix} 1 & 0 \\ 0 & 0 \\ 0 & 0 \\ 0 & 1 \end{bmatrix} \frac{\partial}{\partial r} + \begin{bmatrix} 0 & 0 \\ 1 & 0 \\ 0 & 0 \\ 0 & 0 \end{bmatrix} \frac{1}{\tilde{r}} \right), \ \mathbf{L}_z = \begin{bmatrix} 0 & 0 \\ 0 & 0 \\ 0 & 1 \\ 1 & 0 \end{bmatrix}. \tag{2.36}$$

Then, a one-dimensional finite element discretization is applied along the radial direction, yielding the following interpolation on each element:

$$\mathbf{u}^e(r, z, \omega) = \mathbf{N}^e(r)\mathbf{U}^e(z, \omega). \tag{2.37}$$

$\mathbf{N}^e(r)$ is the matrix of interpolation one-dimensional functions. $\mathbf{U}^e(z, \omega)$ is the vector of nodal displacements. The weak formulation is established by integrating by parts the second order derivatives with respect to r in Eq. (2.2). Regardless of the presence of a PML, detailed steps of the integration can be found in the literature (see [29] for instance) and are not repeated here. It yields Eq. (2.6), where the element matrices are given by Eq.(2.7) with $\mathrm{d}S = 2\pi r \mathrm{d}r$. Under the assumption used in this appendix, $\mathbf{C}$ is reduced to a four-by-four matrix. For instance, the matrix $\mathbf{C}$ for an isotropic material is:

$$\mathbf{C} = \begin{bmatrix} \lambda + 2\mu & \lambda & \lambda & 0 \\ \lambda & \lambda + 2\mu & \lambda & 0 \\ \lambda & \lambda & \lambda + 2\mu & 0 \\ 0 & 0 & 0 & \mu \end{bmatrix}. \tag{2.38}$$

2.B Linearization of the quadratic eigenvalue problem

The system (2.8) can be linearized [29, 74, 75], and yields for instance:

$$(\mathbf{A} - k\mathbf{B})\mathbf{x} = \mathbf{q}, \tag{2.39}$$

with:

$$\mathbf{A} = \begin{bmatrix} \mathbf{0} & \mathbf{K}_1 - \omega^2\mathbf{M} \\ \mathbf{K}_1 - \omega^2\mathbf{M} & \mathrm{j}(\mathbf{K}_2 - \mathbf{K}_2^{\mathrm{T}}) \end{bmatrix}, \mathbf{B} = \begin{bmatrix} \mathbf{K}_1 - \omega^2\mathbf{M} & \mathbf{0} \\ \mathbf{0} & -\mathbf{K}_3 \end{bmatrix}, \mathbf{x} = \begin{bmatrix} \hat{\mathbf{U}} \\ k\hat{\mathbf{U}} \end{bmatrix}, \mathbf{q} = \begin{bmatrix} \mathbf{0} \\ \hat{\mathbf{F}} \end{bmatrix}. \tag{2.40}$$

The free response problem is considered by dropping the source term:

$$\left(\mathbf{K}_1 - \omega^2\mathbf{M} + \mathrm{j}k(\mathbf{K}_2 - \mathbf{K}_2^{\mathrm{T}}) + k^2\mathbf{K}_3\right)\hat{\mathbf{U}} = \mathbf{0}, \tag{2.41}$$

and yields the generalized eigenvalue problem:

$$(\mathbf{A} - k\mathbf{B})\mathbf{x} = \mathbf{0}. \tag{2.42}$$

Because of the PML, the matrices are complex. **A** and **B** are not Hermitian.

2.C Fourier transform of Eq. (2.32)

This appendix gives the analytic Fourier transform $u_z^{\mathrm{ref}}(z,\omega) = \int_{-\infty}^{+\infty} u_z^{\mathrm{ref}}(z,t)\mathrm{e}^{+\mathrm{j}\omega t}\mathrm{d}t$ of Eq. (2.32).

First, the near-field term is written as a convolution product:

$$\int_{z/c_l}^{z/c_s} \tau F(t-\tau)\mathrm{d}\tau = a(t) * F(t), \tag{2.43}$$

with:

$$a(t) = \begin{cases} t & \text{if} \quad t \in [z/c_l; z/c_s], \\ 0 & \text{otherwise.} \end{cases} \tag{2.44}$$

The Fourier transform of $a(t) * F(t)$ is equal to $A(\omega)F(\omega)$, where $F(\omega)$ is the spectrum of the excitation force, and $A(\omega)$ is obtained from an integration by parts, yielding:

$$A(\omega) = \frac{1}{\omega^2}(\mathrm{e}^{\mathrm{j}\omega\frac{z}{c_s}} - \mathrm{e}^{\mathrm{j}\omega\frac{z}{c_l}}) + \frac{z}{\mathrm{j}\omega}(\frac{\mathrm{e}^{\mathrm{j}\omega\frac{z}{c_s}}}{c_s} - \frac{\mathrm{e}^{\mathrm{j}\omega\frac{z}{c_l}}}{c_l}). \tag{2.45}$$

Finally, the Fourier transform of Eq. (2.32) is:

$$u_z^{\mathrm{ref}}(z,\omega) = \frac{1}{2\pi\rho z^3}A(\omega)F(\omega) + \frac{1}{4\pi\rho c_l^2 z}F(\omega)\mathrm{e}^{\mathrm{j}\omega\frac{z}{c_l}}. \tag{2.46}$$

Chapter 3

Numerical modelling of wave scattering by local inhomogeneities in elastic waveguides embedded into infinite media

3.1 Introduction

As recalled earlier, elastic guided waves are often used for non-destructive evaluation (NDE) of elongated structures because they can propagate over a long distance while being sensitive to small damages. However, their scattering behaviour is difficult to interpret, because these waves are multi-modal and dispersive. Furthermore, when the structure is embedded into an infinite elastic medium (*open waveguide*), most of the waves are attenuated by radiation losses (leakage) into the surrounding medium, thus limiting the inspection range of NDE techniques.

In open waveguides, wave scattering by inhomogeneities has been studied experimentally for various structures such as steel bars [4] or seven-wires strands [79] embedded in cement grout, embedded rock bolts [80], reinforced bars [81] or pipes [82] in concrete. Yet, only a few numerical models have been developed, and they remain restricted to circular geometries (see Refs. [7, 42, 83]). Thus, this chapter aims to propose a numerical model suitable for open waveguides of arbitrary cross-section with local inhomogeneities.

The idea is to describe the inhomogeneous (damaged) zone of the waveguide and its vicinity with a finite-element model. The latter is then coupled to a modal representation of the field propagating in the undamaged parts of the waveguide, yielding transparent boundary conditions. This principle has been widely applied in closed waveguides (*i.e.* in vacuum), see Refs. [18, 19, 31, 39, 84–86] for instance. In this chapter, it will be referred to as *hybrid method*. Hybrid methods yield directly the reflection, transmission and conversion properties of the modes while remaining computationally fast. Furthermore, they are not badly affected by backward modes (with group and phase velocities of opposite signs), contrary to methods based on Perfectly Matched Layers (PML) truncating the undamaged parts along the waveguide axis [87].

Hybrid methods cannot be applied directly to open waveguides because the problem is unbounded in the transverse direction. The latter must be bounded for numerical purpose. Furthermore, the modal representation of waves strongly differs from closed waveguides.

In open waveguides, let us remember that three types of modes can be distinguished: trapped modes, radiation modes and leaky modes. Trapped modes propagate without leakage attenuation along the waveguide axis. They are confined in the core of the waveguide or at the interface with the surrounding medium. Out of the core, these modes decay exponentially along the transverse direction. The existence of trapped modes depends on the contrast of materials between the core and the surrounding medium [1]. Radiation modes are standing waves along the transverse direction, which are propagative or evanescent in the axis direction [2, 3, 10]. Leaky modes propagate with leakage attenuation along the waveguide axis. However, these modes grow exponentially in the transverse direction [2, 7, 10].

From a mathematical point of view, trapped modes are a discrete set of poles. Radiation modes are two continuous sets of modes (reduced to one in scalar waveguide), originating from branch cuts integration. Together, trapped modes and radiation modes form the modal basis of open waveguides: their superposition describes any wave field propagating in the waveguide [3, 5]. However, the continua of radiation modes are difficult to manipulate. They can be conveniently approximated by a discrete set of leaky modes in a zone restricted near the core [10, 16]. In that case, leaky modes can provide key information such as the axial attenuation or the travelling velocity of wave packets [4].

From a numerical point of view, modes can be efficiently computed by discretizing only the cross-section of the waveguide while describing analytically the direction of wave propagation. To model open waveguides, a solution consists in using a PML of finite thickness in the transverse direction [12, 13, 68, 69] . In this chapter, this method will be called *PML waveguide formulation*. Other techniques have been proposed (in Refs. [35, 37, 61, 63, 65] for instance) and will not be discussed here (the reader can refer to the introduction of Chap. 2 for details). The PML waveguide formulation avoids most spurious reflections from the absorbing layer, which allows reducing its thickness. Furthermore, the modes are the solution of a linear eigenvalue problem.

As shown in Ref. [47] for scalar waveguides, it is noteworthy that the computation of leaky modes with a PML is mathematically relevant. Besides, radiation modes turn out to lie on two branch cuts rotated by the argument of the PML complex thickness [12] and discretized by the PML truncation to a finite thickness. These modes are often called PML modes (or Berenger modes). Although PML modes are non-intrinsic to the physics (they resonate mainly inside the PML region), their modal superposition enables to accurately reconstruct the forced response of an elastic open waveguide [43] (see also Chap. 2 of this thesis). Nevertheless, their contribution remains unclear as far as scattering problems are considered.

This chapter proposes to use a PML in the transverse direction to truncate the surrounding medium in the finite element model of the inhomogeneous waveguide. This model is coupled to a modal representation based on the PML waveguide formulation, thus providing a hybrid method for open waveguides. Section 3.2 details the numerical method for three-dimensional waveguides of arbitrary cross-section and discusses the modal orthogonality properties specific to the PML formulation. In Sec. 3.3, numerical results are presented for three cases. First, the reflection at the junction between a closed and an open cylindrical waveguide is considered as a validation test case (Sec. 3.3.1). Results are also given for transmission. Then, the scattering of leaky modes by an axisymmetric notch is studied in low-frequency and high-frequency regimes (Sec. 3.3.2). The latter is of particular interest for NDE applications. The contribution of each type of modes to the scattered field is discussed. A particular attention is given to the PML mode contribution. Finally, the reflection of leaky modes by an oblique break is considered as an example of three-dimensional modelling.

3.2 Numerical method

3.2.1 Weak form with a transverse PML

Let us consider an elastic open waveguide made of a core of arbitrary cross-section embedded into an infinite elastic medium. z is the propagation axis of the waveguide. The waveguide contains a local inhomogeneity, such as a notch or a cross-section change for example. The domain $\tilde{V}$ is thus defined as a small part of the waveguide enclosing this inhomogeneity — see Figs. 3.1a and 3.6a for instance.

Small strains and displacements are assumed. A time-harmonic dependence $\mathrm{e}^{-\mathrm{j}\omega t}$ is chosen. In $\tilde{V}$, the weak formulation of elastodynamics is given by:

$$\int_{\tilde{V}} \delta\tilde{\boldsymbol{\epsilon}}^{\mathrm{T}}\tilde{\boldsymbol{\sigma}}\mathrm{d}\tilde{V} - \omega^2 \int_{\tilde{V}} \tilde{\rho}\delta\tilde{\mathbf{u}}^{\mathrm{T}}\tilde{\mathbf{u}}\mathrm{d}\tilde{V} = \int_{\tilde{V}} \delta\tilde{\mathbf{u}}^{\mathrm{T}}\tilde{\mathbf{f}}\mathrm{d}\tilde{V} + \int_{\partial\tilde{V}} \delta\tilde{\mathbf{u}}^{\mathrm{T}}\tilde{\mathbf{t}}\mathrm{d}\partial\tilde{V}, \tag{3.1}$$

where $\tilde{\boldsymbol{\epsilon}}$ and $\tilde{\boldsymbol{\sigma}}$ are the strain and stress vectors, $\tilde{\mathbf{u}}$ is the displacement vector, $\tilde{\mathbf{f}}$ is the vector of volumic forces inside $\tilde{V}$ and $\tilde{\mathbf{t}}$ is the traction vector applied on the surface $\partial\tilde{V}$. The subscript T denotes the matrix transpose. The stress-strain relation is given by $\tilde{\boldsymbol{\sigma}} = \tilde{\mathbf{C}}\tilde{\boldsymbol{\epsilon}}$, where $\tilde{\mathbf{C}}$ is the matrix of material properties (complex-valued for viscoelastic materials).

For numerical purpose, the infinite surrounding medium is truncated by a finite PML of thickness h. A radial PML is considered in this chapter (a Cartesian PML could be used instead, see *e.g.* Ref. [13]). It is introduced by the analytic continuation [49] of the weak form (3.1) into the complex transverse coordinate $\tilde{r}$:

$$\tilde{r}(r) = \int_0^r \gamma(\xi)\mathrm{d}\xi. \tag{3.2}$$

$\gamma(r)$ is a user-defined complex-valued function for attenuating outgoing waves in the surrounding medium, such that:

- $\gamma(r) = 1$ outside the PML region ($r < d$),
- $\mathrm{Im}\big(\gamma(r)\big) > 0$ inside the PML region ($d < r < d + h$).

d is the position of the PML interface. An arbitrary boundary condition is applied at the end of the PML. In this thesis, a Dirichlet condition is chosen.

Finally, Eq. (3.1) must be transformed to go back to the real radial direction r. The change of variable $\tilde{r} \mapsto r$ for any function $\tilde{g}(\tilde{r})$ yields:

$$\tilde{g}(\tilde{r}) = g(r),\ \mathrm{d}\tilde{r} = \gamma(r)\mathrm{d}r,\ \frac{\partial \tilde{g}}{\partial \tilde{r}} = \frac{\partial g}{\partial r}\frac{1}{\gamma(r)},\ \mathrm{d}\tilde{V} = \frac{\tilde{r}(r)\gamma(r)}{r}\mathrm{d}V. \tag{3.3}$$

3.2.2 Hybrid FE-modal approach

A hybrid method is now proposed for the analysis of mode scattering by local inhomogeneities in elastic open waveguides.

The hybrid approach starts from the weak formulation (3.1) after applying the change of variable (3.3). The strain-displacement relation can be written as $\boldsymbol{\epsilon} = \mathbf{L}\mathbf{u}$, where $\mathbf{L}$ is the operator including all spatial derivatives. A FE discretization can then be applied on the volume V. The displacement on each element is given by $\mathbf{u}^e(x, y, z, \omega) = \mathbf{N}_V^e(x, y, z)\mathbf{U}^e(\omega)$ where $\mathbf{N}_V^e(x, y, z)$ is the matrix of three-dimensional interpolation functions and $\mathbf{U}^e(\omega)$ is the vector of nodal displacements. Finally, the FE discretization leads to:

$$\delta\mathbf{U}^{\mathrm{T}}(\mathbf{K} - \omega^2\mathbf{M})\mathbf{U} = \delta\mathbf{U}^{\mathrm{T}}\mathbf{F}, \tag{3.4}$$

where $\mathbf{U}$ is the vector of displacements for all degrees of freedom (dofs) of V, $\mathbf{F}$ is the vector of forces, and $\mathbf{K}$ and $\mathbf{M}$ are the stiffness and mass matrices. The element matrices are given by:

$$\mathbf{K}^e = \int \mathbf{N}_V^{e\,\mathrm{T}}\mathbf{L}^{\mathrm{T}}\mathbf{C}\mathbf{L}\mathbf{N}_V^e\frac{\tilde{r}\gamma}{r}\mathrm{d}V,\ \mathbf{M}^e = \int \rho\mathbf{N}_V^{e\,\mathrm{T}}\mathbf{N}_V^e\frac{\tilde{r}\gamma}{r}\mathrm{d}V. \tag{3.5}$$

These matrices are complex-valued owing to the introduction of the PML.

$\mathbf{U}$ and $\mathbf{F}$ can be partitioned into the dofs belonging to the cross-section boundaries $\Sigma = \bigcup\limits_i \Sigma_i$ (orthogonal to the waveguide axis z, see Figs. 3.1a and 3.6a) and the remaining (*i.e.*

internal) dofs, such that:

$$\mathbf{U} = \begin{bmatrix} \mathbf{U}_\Sigma \\ \mathbf{U}_I \end{bmatrix}, \ \mathbf{F} = \begin{bmatrix} \mathbf{F}_\Sigma \\ \mathbf{F}_I \end{bmatrix}, \tag{3.6}$$

where $I = V \setminus \Sigma$.

The main idea of the hybrid approach is to connect V to semi-infinite homogeneous (*i.e.* inhomogeneity-free) waveguides through the boundaries Σ, thanks to transparent boundary conditions. To do so, $\mathbf{U}_\Sigma$ and $\mathbf{F}_\Sigma$ are expanded on the wave modes of the homogeneous open waveguides as follows:

$$\mathbf{U}_\Sigma = \sum_{n=1}^{N} \alpha_{-n}\mathbf{U}_{-n} + \sum_{n=1}^{N} \alpha_n \mathbf{U}_n, \tag{3.7}$$

$$\mathbf{F}_\Sigma = \sum_{n=1}^{N} \alpha_{-n}\mathbf{F}_{-n} + \sum_{n=1}^{N} \alpha_n \mathbf{F}_n. \tag{3.8}$$

$\mathbf{U}_{\pm n}$ and $\mathbf{F}_{\pm n}$ are the vectors of modal displacements and modal forces for a given mode n. These eigenvectors are computed with the PML waveguide formulation (briefly recalled in Sec. 3.2.3). The $\alpha_{\pm n}$ are the modal coefficients. The subscript $-$ denotes ingoing (incident) modes. The subscript $+$ denotes outgoing (scattered) modes. N denotes the number of modes retained in the modal expansions.

It is convenient to gather known and unknown quantities into two different vectors $\mathbf{U}_-$ and $\mathbf{U}_+$ respectively defined as follows:

$$\mathbf{U}_- = \begin{bmatrix} \boldsymbol{\alpha}_- \\ \mathbf{F}_I \end{bmatrix}, \mathbf{U}_+ = \begin{bmatrix} \boldsymbol{\alpha}_+ \\ \mathbf{U}_I \end{bmatrix}. \tag{3.9}$$

$\boldsymbol{\alpha}_\pm$ are the column vectors of modal coefficients, *i.e.* $\boldsymbol{\alpha}_\pm = [\alpha_{\pm 1} \ \alpha_{\pm 2} \ \ldots \ \alpha_{\pm N}]^{\mathrm{T}}$. Combining Eq. (3.9) with Eqs. (3.7) and (3.8) gives:

$$\mathbf{U} = \mathbf{G}_{u_-}\mathbf{U}_- + \mathbf{G}_{u_+}\mathbf{U}_+, \ \mathbf{F} = \mathbf{G}_{f_-}\mathbf{U}_- + \mathbf{G}_{f_+}\mathbf{U}_+, \tag{3.10}$$

with the following matrices:

$$\mathbf{G}_{u_-} = \begin{bmatrix} \mathbf{B}_{u_-} & \mathbf{0} \\ \mathbf{0} & \mathbf{0} \end{bmatrix}, \mathbf{G}_{u_+} = \begin{bmatrix} \mathbf{B}_{u_+} & \mathbf{0} \\ \mathbf{0} & \mathbf{I} \end{bmatrix}, \mathbf{G}_{f_-} = \begin{bmatrix} \mathbf{B}_{f_-} & \mathbf{0} \\ \mathbf{0} & \mathbf{I} \end{bmatrix}, \mathbf{G}_{f_+} = \begin{bmatrix} \mathbf{B}_{f_+} & \mathbf{0} \\ \mathbf{0} & \mathbf{0} \end{bmatrix}, \tag{3.11}$$

where $\mathbf{B}_{u_\pm} = [\mathbf{U}_{\pm 1} \ \mathbf{U}_{\pm 2} \ \ldots \ \mathbf{U}_{\pm N}]$ and $\mathbf{B}_{f_\pm} = [\mathbf{F}_{\pm 1} \ \mathbf{F}_{\pm 2} \ \ldots \ \mathbf{F}_{\pm N}]$ are the basis of modal displacements and modal forces.

Using Eqs. (3.4) and (3.10) for any arbitrary field $\delta\mathbf{U}^{\mathrm{T}} = \left[\delta\boldsymbol{\alpha}_+^{\mathrm{T}} \ \delta\mathbf{U}_I^{\mathrm{T}}\right]^{\mathrm{T}}$, one finally gets the following linear matrix system:

$$\mathbf{G}_{u_+}^{\mathrm{T}}(\mathbf{D}\mathbf{G}_{u_+} - \mathbf{G}_{f_+})\mathbf{U}_+ = \mathbf{G}_{u_+}^{\mathrm{T}}(\mathbf{G}_{f_-} - \mathbf{D}\mathbf{G}_{u_-})\mathbf{U}_-, \tag{3.12}$$

where $\mathbf{D} = \mathbf{K} - \omega^2\mathbf{M}$ is the dynamic stiffness matrix. The system (3.12) is solved for each angular frequency ω.

3.2.3 PML waveguide formulation for mode computation

Eigenvectors used in the modal expansions (3.7) and (3.8) can be obtained with the so-called PML waveguide formulation. The derivation of the PML waveguide formulation starts from the weak form (3.1) after the change of variable (3.3), written on each cross-section Σ_i, dropping the source-term, and assuming an $\mathrm{e}^{\mathrm{j}kz}$ dependence for $\mathbf{u}$ ($\mathrm{e}^{-\mathrm{j}kz}$ for $\delta\mathbf{u}$). k is the axial wavenumber. Hence, the strain-displacement relation can be written as:

$$\boldsymbol{\epsilon} = (\mathbf{L}_S + \mathrm{j}k\mathbf{L}_z)\mathbf{u}, \tag{3.13}$$

where $\mathbf{L}_S$ is the operator including all terms but derivatives with respect to the z-axis, and $\mathbf{L}_z$ is the operator of z-derivatives.

A FE discretization is then applied on the cross-section. The displacement on each element can be written $\mathbf{u}^e(x, y, \omega) = \mathbf{N}^e_\Sigma(x, y)\boldsymbol{\Phi}^e(\omega)$, where $\mathbf{N}^e_\Sigma(x, y)$ is the matrix of two-dimensional interpolation functions and $\boldsymbol{\Phi}^e(\omega)$ is the vector of nodal displacements. The following quadratic eigenvalue problem is finally obtained [13, 43]:

$$\left(\mathbf{K}_1 - \omega^2\mathbf{M}_S + \mathrm{j}k(\mathbf{K}_2 - \mathbf{K}_2^{\mathrm{T}}) + k^2\mathbf{K}_3\right)\boldsymbol{\Phi} = \mathbf{0}, \tag{3.14}$$

where the element matrices are given by:

$$\begin{aligned}
\mathbf{K}^e_1 &= \int \mathbf{N}^{e\,\mathrm{T}}_\Sigma\mathbf{L}_S^{\mathrm{T}}\mathbf{C}\mathbf{L}_S\mathbf{N}^e_\Sigma\frac{\tilde{r}\gamma}{r}\mathrm{d}S,\ \mathbf{K}^e_2 = \int \mathbf{N}^{e\,\mathrm{T}}_\Sigma\mathbf{L}_S^{\mathrm{T}}\mathbf{C}\mathbf{L}_z\mathbf{N}^e_\Sigma\frac{\tilde{r}\gamma}{r}\mathrm{d}S,\\
\mathbf{K}^e_3 &= \int \mathbf{N}^{e\,\mathrm{T}}_\Sigma\mathbf{L}_z^{\mathrm{T}}\mathbf{C}\mathbf{L}_z\mathbf{N}^e_\Sigma\frac{\tilde{r}\gamma}{r}\mathrm{d}S,\ \mathbf{M}^e_S = \int \rho\mathbf{N}^{e\,\mathrm{T}}_\Sigma\mathbf{N}^e_\Sigma\frac{\tilde{r}\gamma}{r}\mathrm{d}S.
\end{aligned} \tag{3.15}$$

$\boldsymbol{\Phi}$ is the vector of nodal displacements on the cross-section. More details can be found *e.g.* in Refs. [12, 13], as well as in Appendix 3.A in the specific case of an axisymmetric circular open waveguide, which will be used to obtain the numerical results presented in Sec. 3.3.1 and 3.3.2.

The eigenproblem (3.14) must be linearized to make its resolution easier with standard eigensolvers [74]. The following linearized form is adopted:

$$(\mathbf{A} - k\mathbf{B})\mathbf{x} = \mathbf{0}, \tag{3.16}$$

with

$$\mathbf{A} = \begin{bmatrix} \mathbf{0} & \mathbf{I} \\ \mathbf{K}_1 - \omega^2\mathbf{M}_S & \mathrm{j}(\mathbf{K}_2 - \mathbf{K}_2^{\mathrm{T}}) \end{bmatrix}, \mathbf{B} = \begin{bmatrix} \mathbf{I} & \mathbf{0} \\ \mathbf{0} & -\mathbf{K}_3 \end{bmatrix}, \mathbf{x} = \begin{bmatrix} \boldsymbol{\Phi} \\ k\boldsymbol{\Phi} \end{bmatrix}. \tag{3.17}$$

Equation (3.16) is solved for each angular frequency ω. Due to the symmetry of matrices $\mathbf{K}_1$, $\mathbf{K}_3$ and $\mathbf{M}_S$, the eigenspectrum is composed of pairs of eigensolutions, denoted $\{k_n, \mathbf{U}_n\}$ and $\{k_{-n}, \mathbf{U}_{-n}\}$ with $k_{-n} = -k_n$ for $(n = 1, \ldots, N)$, representing N outgoing modes and N ingoing modes respectively [12, 13].

The modal forces $\mathbf{F}_n$ used in the modal expansion (3.8) are defined from [39, 75]:

$$\int_{\Sigma_i} \delta\mathbf{u}^{\mathrm{T}}\mathbf{t}_n = \delta\boldsymbol{\Phi}^{\mathrm{T}}\mathbf{F}_n, \tag{3.18}$$

where for the mode n, $\mathbf{t}_n$ is the vector of the traction applied on the cross-section Σ_i with an outward unit normal. It can be checked that $\mathbf{t}_n = \mathbf{L}_z^{\mathrm{T}}\boldsymbol{\sigma}_n = \mathbf{L}_z^{\mathrm{T}}\mathbf{C}(\mathbf{L}_S + \mathrm{j}k\mathbf{L}_z)\mathbf{u}_n$, so that the modal forces are explicitly given by [39, 75]:

$$\mathbf{F}_{\pm n} = (\mathbf{K}_2^{\mathrm{T}} + \mathrm{j}k_{\pm n}\mathbf{K}_3)\mathbf{U}_{\pm n}. \tag{3.19}$$

3.2.4 Mode properties

3.2.4.1 Modal characteristics

As recalled in Chap. 2, modal characteristics can be readily computed from the eigensolutions of Eq. (3.14) and the finite element matrices (3.15) [13]. For a given mode n, its phase velocity is:

$$v_{p_n} = \frac{\omega}{\mathrm{Re}(k_n)}. \tag{3.20}$$

Its attenuation in $\mathrm{dB\,m^{-1}}$ is:

$$\eta_n = 8,686\mathrm{Im}(k_n). \tag{3.21}$$

The group velocity $v_{g_n} = \partial\omega/\partial k_n$ is computed as follows [13]:

$$v_{g_n} = \mathrm{Re}\left[\left(\frac{2\omega\mathbf{U}_{-n}^{\mathrm{T}}\mathbf{M}\mathbf{U}_n}{\mathbf{U}_{-n}^{\mathrm{T}}(\mathrm{j}(\mathbf{K}_2 - \mathbf{K}_2^{\mathrm{T}}) + 2k_n\mathbf{K}_3)\mathbf{U}_n}\right)^{-1}\right]. \tag{3.22}$$

In open waveguides, the energy velocity can be defined by [76]:

$$\overline{v}_{e_n} = \frac{\mathrm{Re}(\overline{P}_n)}{\mathrm{Re}(\overline{T}_n) + \mathrm{Re}(\overline{V}_n)}, \tag{3.23}$$

where for each mode n, $\overline{P}_n$ is the normal component of the Poynting vector integrated on the core cross-section, $\overline{T}_n$ is the core cross-section and time-averaged kinetic energy, and $\overline{V}_n$ is the core cross-section and time-averaged potential energy. These quantities can be post-processed from [13]:

$$\overline{P}_n = \frac{-\mathrm{j}\omega}{2}\overline{\mathbf{U}}_n^*, (\overline{\mathbf{K}}_2^{\mathrm{T}} + \mathrm{j}k_n\overline{\mathbf{K}}_3)\overline{\mathbf{U}}_n, \tag{3.24}$$

$$\overline{T}_n = \frac{\omega^2}{4}\overline{\mathbf{U}}_n^*\overline{\mathbf{M}\mathbf{U}}_n, \tag{3.25}$$

$$\overline{V}_n = \frac{1}{4}\overline{\mathbf{U}}_n^*(\overline{\mathbf{K}}_1 + \mathrm{j}k_n\overline{\mathbf{K}}_2 - \mathrm{j}k_n^*\overline{\mathbf{K}}_2^{\mathrm{T}} + k_n^*k_n\overline{\mathbf{K}}_3)\overline{\mathbf{U}}_n. \tag{3.26}$$

where the * superscript denotes conjugate transpose and the overbar stands for the restriction to the dofs of the core of the cross-section. Note that the integration is usually restricted to the core cross-section in open waveguides because of the growth of leaky modes in the transverse directions. This restriction is quite arbitrary but gives a reasonable approximation of the travelling velocities of wave packets [4, 76]. In this chapter, the calculation of $\overline{P}_n$ and $\overline{v}_{e_n}$ will only be used for post-processing steps (*i.e.* for dispersion curves and normalization of the scattering coefficients).

3.2.4.2 Determination of the travelling direction

The hybrid method presented in Sec. 3.2.2 requires determining the travelling direction of the modes. In elastic waveguides, the phase velocity does not necessarily give the travelling direction because of the existence of backward modes, which have phase and group velocities of opposite signs [40, 70]. The travelling direction of the modes is determined according to the following criterion [43] (see also Chap. 2 of this thesis):

- the sign of $\mathrm{Im}(k_n)$ if $\mathrm{Im}(k_n) \neq 0$, such that if $\mathrm{Im}(k_n) > 0$, the mode is a positive-going mode (towards $z > 0$), and if $\mathrm{Im}(k_n) < 0$ the mode is negative-going (towards $z < 0$).
- the sign of v_{g_n} if $k_n \in \mathbb{R}$.

The criterion is valid both for closed and open elastic waveguides. In closed waveguides, the case $k_n \in \mathbb{R}$ corresponds to propagating modes. In open waveguides, modes with real wavenumbers are somehow particular because they correspond to trapped modes. Trapped modes exist only when the shear velocity is greater in the embedding medium than in the core (except if longitudinal and shear waves couple into Stoneley waves [1]). Besides in viscoelastic media, modes with real wavenumbers never occur, because the wavenumbers are then always complex-valued.

3.2.4.3 Post-processing of scattering coefficients

In this chapter, reflection and transmission coefficients are defined by considering an incident mode $-n$ through the section Σ_1. The scattered modal coefficients α_{+n} are directly obtained by solving (3.12). Owing to leakage losses, their values depend on the positions z_i of the cross-sections Σ_i. With the hybrid method, these positions are user-defined parameters and are hence arbitrary.

To circumvent this problem, a reference position is chosen to post-process the scattering coefficients. In this chapter, this reference position is set to the inhomogeneity position, *i.e.* $z = z_{\text{ref}}$ — see Figs. 3.1a and 3.6a for instance. As done for viscoelastic problems in closed waveguides [88, 89], this amounts to retropropagate the modal coefficients to the inhomogeneity position. Hence, the reflection coefficient of a mode m is defined on Σ_1 by:

$$R_{m,n} = \frac{|\alpha_{+m} \mathrm{e}^{+\mathrm{j}k_{+m}(z_{\text{ref}}-z_1)}|\sqrt{|\mathrm{Re}(\overline{P}_{+m})|}}{|\alpha_{-n} \mathrm{e}^{+\mathrm{j}k_{-n}(z_{\text{ref}}-z_1)}|\sqrt{|\mathrm{Re}(\overline{P}_{-n})|}}. \tag{3.27}$$

Similarly, the transmission coefficient of a mode m is defined on Σ_2 by:

$$T_{m,n} = \frac{|\alpha_{+m} \mathrm{e}^{+\mathrm{j}k_{+m}(z_{\text{ref}}-z_2)}|\sqrt{|\mathrm{Re}(\overline{P}_{+m})|}}{|\alpha_{-n} \mathrm{e}^{+\mathrm{j}k_{-n}(z_{\text{ref}}-z_1)}|\sqrt{|\mathrm{Re}(\overline{P}_{-n})|}}. \tag{3.28}$$

Such definitions enables to have scattering coefficients which are independent on the position of the cross-section Σ_i. Note that the coefficients are also normalized by the modal power computed with Eq. (3.24).

3.2.5 Modal orthogonality in open waveguides

In a waveguide, any arbitrary field can be expanded on a unique set of modes if they are orthogonal [40]. In open waveguides, orthogonality theoretically holds between trapped modes and radiation modes when integrated on the infinite cross-section [3, 5]. If the integration is restricted to the core cross-section, trapped and radiation modes are no longer orthogonal. On the other hand, leaky modes may approximate the contribution of radiation modes [10, 16], but they cannot satisfy the orthogonality relationship since they grow to infinity in the transverse direction.

When the transverse problem is bounded by a finite PML, the authors have recently shown [43] (see also Chap. 2 of this thesis) that the following orthogonality relationship holds:

$$Q_{m,-n} = \frac{\mathrm{j}\omega}{4}(\mathbf{U}_m^{\mathrm{T}}\mathbf{F}_{-n} - \mathbf{U}_{-n}^{\mathrm{T}}\mathbf{F}_m) = Q_{m,-m}\delta_{mn}. \tag{3.29}$$

This orthogonality relationship involves the whole cross-section of the waveguide (*i.e.* including the finite PML) and is applicable to any kind of modes without distinction (trapped, leaky and PML modes). It also remains valid for fully anisotropic or viscoelastic materials. Equation (3.29) guarantees the uniqueness of modal expansions (3.7) and (3.8). Actually, it is a discrete form of the so-called Auld's real orthogonality relationship [40], as already shown for closed viscoelastic waveguides [75].

It has to be emphasized that Eq. (3.29) is generally not a power orthogonality relationship. To prove this, let us start with the total time-averaged power flow across the whole cross-section, given by [39]:

$$\Pi_T = \mathrm{Re}(-\frac{\mathrm{j}\omega}{2}\mathbf{U}_\Sigma^*\mathbf{F}_\Sigma). \tag{3.30}$$

Expanding the fields $\mathbf{U}_\Sigma$ and $\mathbf{F}_\Sigma$ on the modes yields (details are given in Appendix 3.B):

$$\Pi_T = \sum_{m=-N}^{N} |\alpha_m|^2 \mathrm{Re}(P_m) + \sum_{m=-N}^{N}\sum_{n\neq m} \alpha_n^*\alpha_m P_{m,n}, \tag{3.31}$$

where $P_{m,n} = \frac{\mathrm{j}\omega}{4}(\mathbf{F}_n^*\mathbf{U}_m - \mathbf{U}_n^*\mathbf{F}_m)$ is the modal cross-power of modes m and n. For $m = n$, one has $P_{m,m} = \mathrm{Re}(P_m)$, where $\mathrm{Re}(P_m) = \frac{\omega}{2}\mathrm{Im}(\mathbf{U}_m^*\mathbf{F}_m)$ is the modal power of the mode m. Note that P_m is computed from the same equation as Eq. (3.24) but by removing the overbar in order to consider the whole cross-section.

There is so-called *power orthogonality* if the total power in the waveguide is the sum of the power propagated by each mode, that is if $P_{m,n} = 0$ for all $m \neq n$ [40, 90]. However, the modal cross power $P_{m,n}$ is in general non-zero, except if the so-called Auld's complex biorthogonality relationship [40] is satisfied, that is to say, for real wavenumber modes only: in that case, $\mathbf{U}_{-n}^{\mathrm{T}} = \mathbf{U}_n^*$ and $\mathbf{F}_{-n}^{\mathrm{T}} = \mathbf{F}_n^*$ such that Eq. (3.29) becomes $Q_{m,-n} = P_{m,n} = \mathrm{Re}(P_m)\delta_{mn}$ [75].

As a consequence, there is no power orthogonality ($Q_{m,-n} \neq P_{m,n}$) in open waveguides involving leaky modes or in lossy closed waveguides (wavenumbers are complex). The modal cross power should thus be considered. This has been studied in electromagnetic open waveguides, see *e.g.* Ref [2, 10, 72, 91, 92]. As for scattering analysis, this phenomenon is likely to complicate the interpretation of results in terms of modes. This will be illustrated in Sec. 3.3.2.3.

3.3 Results

3.3.1 The junction test case

As a first test case, the reflection of the fundamental longitudinal guided mode L(0,1) at the junction between a closed and an open cylindrical waveguide is computed with the hybrid method and compared to literature results. Results are also presented for the transmission coefficient and the role of PML modes in the solution of the scattering problem is investigated.

Material	ρ ($\mathrm{kg\,m^{-3}}$)	c_l ($\mathrm{m\,s^{-1}}$)	c_s ($\mathrm{m\,s^{-1}}$)	η_l (Np wavelength^{-1})	η_s (Np wavelength^{-1})
Steel	7932	5960	3260	0.003	0.008
Epoxy	1170	2610	1000	0	0
Cement grout	1600	2810	1700	0.043	0.1

Table 3.1 – Material properties

3.3.1.1 Description

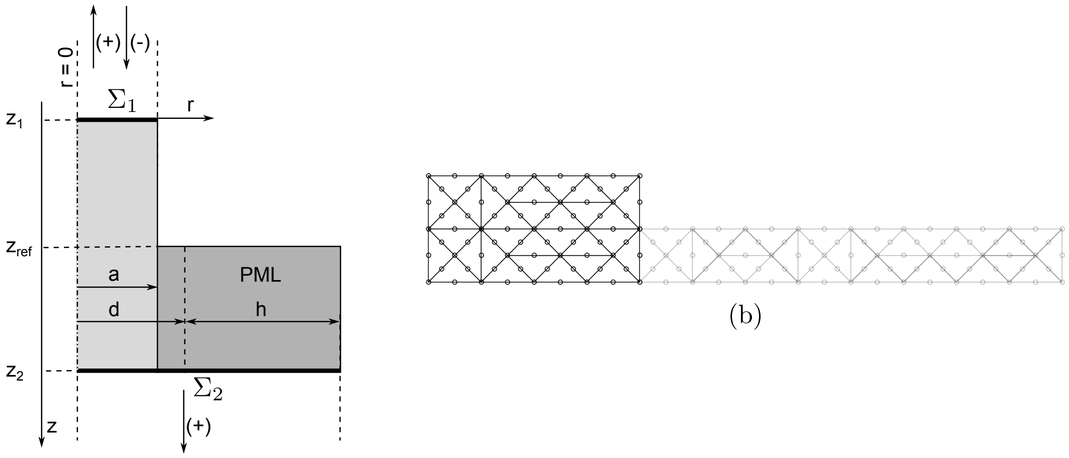

(a)

(b)

Figure 3.1 – Junction test case. (a) Sketch of the computational domain V; (b) Finite element mesh (black: physical domain, grey: PML domain, PML parameters: $d = a$, $h = 2a$).

One considers a cylindrical steel waveguide of radius $a = 1$ mm partly embedded in an infinite epoxy medium. Materials properties are given in Table 3.1 (in the following, pure elastic materials are considered, *i.e.* the longitudinal and shear bulk wave attenuations η_l and η_s are equal to 0 Np/wavelength).

In Ref. [7], the reflection of the L(0,1) guided mode at the junction has been studied both with a mode-matching method and with a transient finite-element model. Herein, the scattering problem is solved with the axisymmetrical formulation of the hybrid method. The computational domain V is depicted in Fig. 3.1a. The inlet and outlet cross-sections boundaries Σ_1 and Σ_2 are set at equal distances $|z_i - z_{\mathrm{ref}}| = 0.25a$ from the junction. A free surface condition is applied on the outer surface of the closed waveguide region ($z < z_{\mathrm{ref}}, r = a$) and on the inlet of the epoxy layer ($z = z_{\mathrm{ref}}, a < r < a + h$). The epoxy layer is bounded by a transverse PML. Following Ref. [13], the attenuation of the PML is chosen as parabolic and is given by:

$$\gamma(r) = \begin{cases} 1 & \text{if} \quad r \leq d, \\ 1 + 3(\hat{\gamma} - 1)\left(\dfrac{r-d}{h}\right)^2 & \text{if} \quad r > d, \end{cases} \tag{3.32}$$

where $\hat{\gamma} = \frac{1}{h}\int_d^{d+h} \gamma(\xi) d\xi$ is the average value of $\gamma(r)$ inside the PML region. $\hat{\gamma}$ and h are user-defined parameters. To avoid spurious eigenvalues and to enhance the attenuation of leaky modes, it is preferable to set the PML close to the core [47]. In the following, the

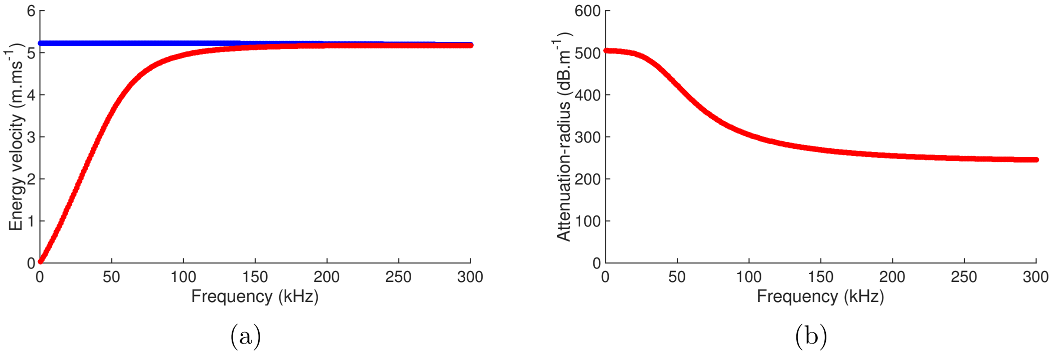

(a) (b)

Figure 3.2 – PML waveguide formulation results for (a) the energy velocity of the L(0,1) guided mode (blue dots) and the L(0,1) leaky mode (red dots) and (b) the attenuation of the L(0,1) leaky mode. PML parameters are: $d = a$, $h = 2a$, $\hat{\gamma} = 8 + 16\mathrm{j}$. Filtering criterion: $\eta_{\min} = 0.5$.

distance is set to $d = a$ and the PML thickness is set to $h = 2a$. Note that in order to accurately compute leaky modes at the lowest frequencies (large wavelengths), the PML must have a relatively large complex thickness $d + \hat{\gamma}h$. After numerical tests, the value of $\hat{\gamma}$ has been set to $\hat{\gamma} = 8+16\mathrm{j}$. Despite this large complex thickness, the computational cost remains low because a coarse mesh is sufficient to obtain acceptable results in the frequency range of interest. The dispersion curves of the fundamental L(0,1) mode computed at both the inlet ant outlet cross-sections are given in Fig. 3.2 (PML modes have been filtered out from the visualization following the criterion of Appendix 3.C).

The domain V is meshed with 6-nodes triangle elements, yielding a total of 338 dofs (see Fig. 3.1b) with 18 dofs on the cross-section Σ_1 and 52 dofs on the cross-section Σ_2. The latter values must be multiplied by two for the linearized eigenvalue problem (see Sec. 3.2.3). The eigenproblem (3.16) is solved with the ARPACK library [77]. Based on an implicit restarted Arnoldi method, this library enables to obtain a user-defined number of eigenvalues (denoted as $2N$), corresponding to the closest in absolute value to a user-defined shift (set to 0 in this chapter). For this test case, $N = 20$ modes are initially computed on each cross-section. The number of modes finally retained in the modal expansions is denoted $N_{\Sigma_i} (i = 1, 2)$.

3.3.1.2 Numerical results

Figure 3.3 shows the wavenumber spectrum computed on the cross-section Σ_2 (open waveguide), in the complex plane ($\mathrm{Re}(ka) > 0$, $\mathrm{Im}(ka) > 0$) and at $f = 300$ kHz. The spectrum includes the L(0,1) leaky mode and 19 PML modes. As expected, PML modes close to the real axis ($\mathrm{Im}(ka) = 0$) lie along two hyperbolas corresponding to branch cuts rotated with an angle $-\arg(d + h\hat{\gamma})$, and starting at branchpoints $\omega a/c_{l,s}$ ($c_{l,s}$ being the bulk velocities in the epoxy layer). A deviation from the hyperbolas can be observed far from the real axis. This deviation can be reduced by using a finer FE mesh [12]. Further details on the behaviour of PML modes can be found in Refs. [13, 43]. As far as the cross-section Σ_1 is concerned (closed waveguide), the wavenumber spectrum includes the L(0,1) guided mode (real wavenumber) and 19 complex inhomogeneous or evanescent modes (spectrum not shown for conciseness).

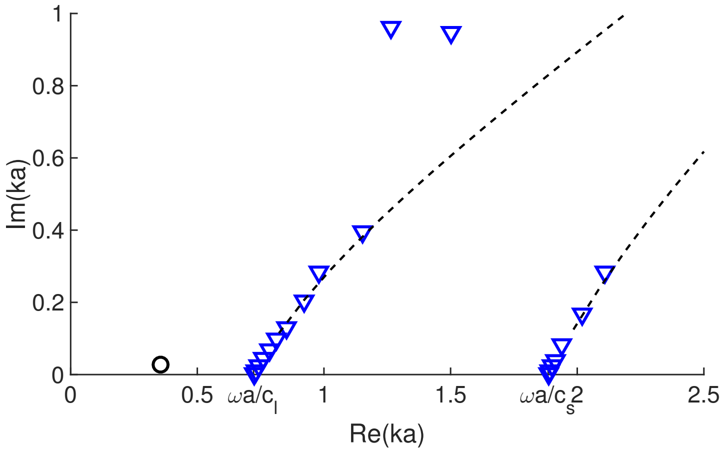

Figure 3.3 – Wavenumber spectrum ($N = 20$) of an elastic steel waveguide embedded into epoxy computed with the PML waveguide formulation (cross-section Σ_2), at $f = 300$ kHz. Black circle: leaky mode, blue triangles: PML modes, dashed black lines: theoretical branch cuts with a finite PML rotated by $-\arg(d + h\hat{\gamma})$. PML parameters: $d = a, h = 2a, \hat{\gamma} = 8 + 16\text{j}$.

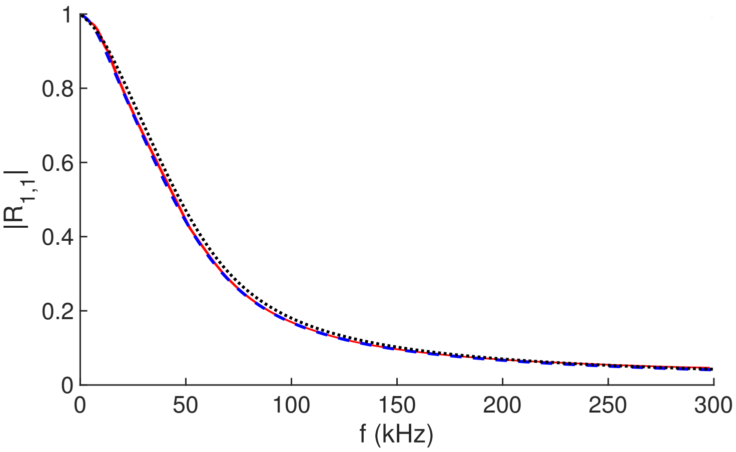

Figure 3.4 – Reflection coefficient of the L(0,1) mode by the junction. Red curve: results of Ref. [7]. Blue dashed curve: hybrid approach with $N_{\Sigma_1} = 1$, $N_{\Sigma_2} = 20$. Black dotted curve: hybrid approach with $N_{\Sigma_1} = 1$, $N_{\Sigma_2} = 1$. PML parameters: $d = a$, $h = 2a$, $\hat{\gamma} = 8 + 16\text{j}$.

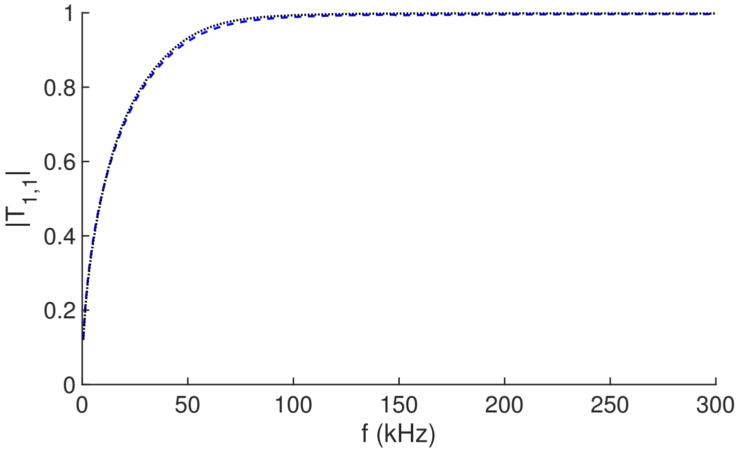

Figure 3.5 – Transmission coefficient of the L(0,1) leaky mode by the junction. Blue dashed curve: hybrid approach with $N_{\Sigma_1} = 1$, $N_{\Sigma_2} = 20$. Black dotted curve: hybrid approach with $N_{\Sigma_1} = 1$, $N_{\Sigma_2} = 1$. PML parameters: $d = a$, $h = 2a$, $\hat{\gamma} = 8 + 16\mathrm{j}$.

First, all the modes computed on Σ_2 are retained in the modal expansion ($N_{\Sigma_2} = N = 20$). On Σ_1, it has been checked that the inclusion of evanescent or inhomogeneous modes has a negligible influence on the results (in agreement with Ref. [7]). Hence, only the L(0,1) guided mode is retained in the modal expansions ($N_{\Sigma_1} = 1$). The reflection coefficient is shown in Fig. 3.4. A very good agreement is obtained with Ref. [7]. Comparisons have been also made with other results of Ref. [7] for various radii and material properties and have shown a similar accuracy of results (not shown). The transmission coefficient of the L(0,1) mode has also been computed with the hybrid method (Fig. 3.5). As it can be observed, the transmission curve exhibits an opposite behaviour compared to the reflection curve and quickly tends to one as the frequency increases.

Second, only the leaky mode is retained in the modal expansion on Σ_2 ($N_{\Sigma_2} = 1$). As shown in Fig. 3.3, some PML modes close to the branch points have a quite low attenuation (given by $\mathrm{Im}(ka)$), smaller than the attenuation of the L(0,1) leaky mode. Hence, their contribution to the solution could *a priori* be significant. Yet, the contribution of PML modes turns out to be weak and a good approximation of the scattering by the junction is still obtained with the leaky mode only (see Figs. 3.4 and 3.5). Actually, PML modes oscillate mainly inside the PML layer, which significantly reduces their contribution to the solution inside the core.

It is noteworthy that, in the very far-field, the contribution of PML modes can become predominant over leaky modes due to long-term diffraction (long-term diffraction decays geometrically, as opposed to leaky modes which decay exponentially). This has been demonstrated for the forced response of waveguides in Refs. [15, 43] (see also Chap. 2 of this thesis). In our scattering problem, this could be also observed if an artificially large distance from the junction were chosen. Nevertheless, the goal of hybrid methods is to reduce the FE mesh close to the vicinity of the inhomogeneity. Therefore in practice, the distance $|z_i - z_{\mathrm{ref}}|$ is expected to remain low enough to prevent the influence of long-term diffraction.

As will be shown for the next test case, including PML modes can yet be necessary to accurately reconstruct the scattered solution in the very near field, *i.e.* when the cross-section boundaries are set very close to the inhomogeneity.

3.3.2 Scattering by an axisymmetric notch

A cylindrical open waveguide damaged by a notch in the core is now considered. For simplicity, one assumes an axisymmetric notch. The scattering analysis is performed both in a low and a high-frequency regime. The contribution of PML modes to the solution is discussed in the near field. This test case also enables to consider a configuration with large modal cross-powers, highlighting their influence on the modal scattering coefficients.

3.3.2.1 Description

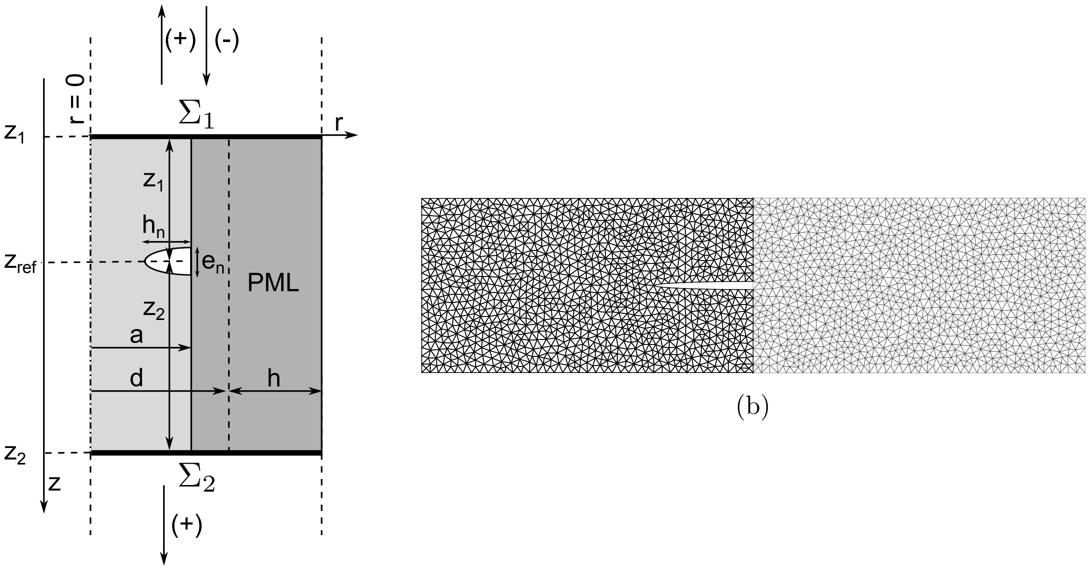

(a)

(b)

Figure 3.6 – Notch test case. (a) Scheme of the computational domain V; (b) Finite element mesh for $|z_i - z_{\text{ref}}| = 0.25a$. Black: physical domain; grey: PML domain. PML parameters: $d = h = a$. Notch: $e_n/a = 0.025$, $h_n/a = 0.3$.

Let us consider a cylindrical waveguide made of viscoelastic steel and embedded into an infinite cement grout medium. Materials properties are given in Table 3.1. The core of the waveguide has a radius $a = 10$ mm and is damaged by a notch described by a semi ellipse centered at $(r = a, z = z_{\text{ref}})$, of depth h_n along r and width e_n along z (see Fig. 3.6a). The width of the notch is set to $e_n/a = 0.025$ and the depth h_n/a is a varying parameter.

As before, the scattering problem is solved with an axisymmetrical formulation of the hybrid method. The computational domain is depicted in Fig. 3.6a. The embedding medium is truncated with a PML of same attenuation profile than in Eq. (3.32).

Dispersion curves of the waveguide are shown in Fig. 3.7 for 12 modes corresponding to leaky longitudinal modes, conventionally labelled as L(0,n). PML modes have been filtered out from the visualization following the criterion of Appendix 3.C. Because of material properties, no trapped modes can propagate. The results of Ref. [4] calculated by a global matrix approach are also shown, which confirms the accuracy of leaky mode computation with the PML waveguide formulation. The following PML parameters have been used: $h = a$, $d = a$, $\hat{\gamma} = 1 + 2\mathrm{j}$.

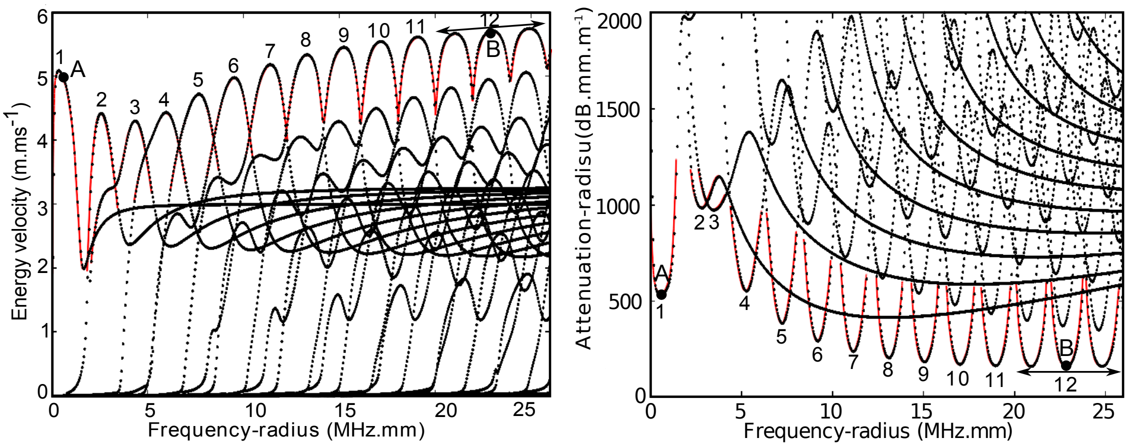

(a) (b)

Figure 3.7 – PML waveguide formulation results (black dots) and results of Ref. [4] (red line) for (a) the energy velocity $\overline{v}_e$ and (b) the attenuation (steel cylinder embedded into cement grout, viscoelastic case). PML parameters are: $h = a$, $d = a$, $\hat{\gamma} = 1 + 2\mathrm{j}$. Filtering criterion: $\eta_{\min} = 0.6$. Point A: f = 0.6 MHz mm. Point B: f = 22.89 MHz mm.

In open waveguides at high frequencies, the energy can be concentrated into the core, thus reducing the leakage attenuation [4]. Herein, the minimal attenuation is equal to 159 dB mm m^{-1} and is reached for the 12th mode (L(0,12)) at point B (f = 22.89 MHz mm) — see Fig. 3.7b. The attenuation of higher order modes is greater because of the predominance of viscoelasticity over leakage for higher frequencies. Since the 12th mode propagates over greater distances than the others, it is quite attractive for NDE applications. Hence, it is interesting to get a better understanding of its interaction with inhomogeneities.

In the following, the scattering of the 12th leaky mode by a notch of varying depth h_n is studied. The problem is solved over the second lobe (between 21.64 MHz mm and 24.12 MHz mm) and particularly at point B. For the sake of comparison, the reflection and transmission of the 1st leaky mode (L(0,1)) at $f = 0.6$ MHz mm (point A in Fig. 3.7) is also computed. Both reflection and transmission coefficients are post-processed at the position z_{ref} according to Eqs. (3.27) and (3.28).

The inlet and outlet cross-sections boundaries, Σ_1 and Σ_2, are set at distances $|z_i - z_{\mathrm{ref}}| = a$ for the low-frequency regime (point A) and $|z_i - z_{\mathrm{ref}}| = 0.25a$ for the high-frequency regime. The domain is meshed with 6-nodes triangle elements, yielding about 53000 dofs and 18000 dofs respectively, with 324 dofs on both cross-sections — see Fig. 3.6b. It has been checked that the contribution of PML modes was negligible. Therefore, only leaky modes are retained yielding $N_{\Sigma_1} = N_{\Sigma_2} = 13$ at point A and $N_{\Sigma_1} = N_{\Sigma_2} = 40$ at point B. Results are presented in Sec. 3.3.2.2 and 3.3.2.3. To highlight the contribution of PML modes in the very near-field of the notch, another configuration is considered at point A by reducing the cross-section distance to $|z_i - z_{\mathrm{ref}}| = 0.25a$. Results are presented in Sec. 3.3.2.4.

3.3.2.2 Results

Reflection and transmission coefficients are displayed in Fig. 3.8 for various notch depths, at point A for the 1st leaky mode and at point B for the 12th leaky mode. The coefficients exhibit the same general trend at both frequencies. The reflection coefficient increases when the notch depth increases, and conversely for the transmission coefficient. Note that the reflection coefficient at point A for a notch of depth $h_n/a > 0.9a$ is greater than one (this phenomenon is discussed further). It is noteworthy that our results are very close to those of Ref. [17], obtained with the L(0,1) mode in the low-frequency regime with a transient finite-element model, for an elastic steel core embedded into grout and damaged by a rectangular notch. This similarity confirms the reliability of the proposed hybrid method for the scattering analysis of open waveguides.

The differences in the scattering behaviour between low and high frequencies, as observed in Fig. 3.8, can be related to the distribution of the mode energy over the cross-section. For small depth notches, the reflection of the 12th leaky mode is lower than for the 1st one because its energy is more concentrated at the centre of the core of the waveguide. On the other hand, it can be observed that some energy of the 1st leaky mode is still transmitted for a full-depth notch ($|T_{1,1}| = 0.18$), indicating an energy transfer between both sides of the notch through the embedding medium (also in agreement with Ref. [17]). This is not the case for the 12th leaky mode, which transmission coefficient is negligible. The scattered fields computed at both frequencies are shown in Fig. 3.9. Differences of energy distribution over the cross-section can be clearly observed.

Figure 3.10 displays the reflection and transmission coefficients of several leaky modes at high frequencies around point B. Despite a high number of propagating modes, mode conversion is negligible except for a limited number of modes, namely the L(0,13) and mostly the L(0,14) leaky mode. Yet, it must be kept in mind that the scattering coefficients shown have been retropropagated at the inhomogeneity position. The propagation far from the inhomogeneity will favour the less attenuated mode, *i.e.* the 12th leaky mode here. In addition, the 12th leaky mode benefits from a high reflection coefficient, particularly for deep notches (see Fig. 3.8), which confirms the high reflection capability of high order low-leakage modes sometimes mentioned in the literature [93].

In Fig. 3.10, it should be noted that the reflection and transmission coefficients vary in a counter-intuitive way. Indeed, instead of having opposite behaviour as normally expected, both coefficients curves sharply peak around 22 MHz mm and 24 MHz mm. Furthermore, the transmission coefficient of the 12th mode takes values greater than one (as already observed in Fig. 3.8 for the reflection of the 1st leaky mode at point A). Actually, these results cannot be analyzed without further considerations on the modal cross power, as discussed in the next section.

3.3.2.3 Considerations on the modal cross power

Reflection and transmission coefficients are defined for each mode separately, and thus do not account for the modal cross power. The transmitted cross powers $P_{12,13}$ and $P_{12,14}$ are displayed in Fig. 3.11 at high frequencies (results are similar in reflection). Their values are negligible (particularly at point B) except around 22 MHz mm and 24 MHz mm, *i.e.* at frequencies corresponding to the peaks previously observed in Fig. 3.10.

As shown in Fig. 3.12, one can observe that this phenomenon takes place at frequencies where mode crossing of phase velocity curves occurs. As noticed in Ref. [4] at high frequencies, the phase velocity curve of the 12th mode crosses those of the 13th and 14th modes. At these crossing frequencies, the modes have the same values of $\mathrm{Re}(ka)$ and similar mode shapes, which explains their strong interaction.

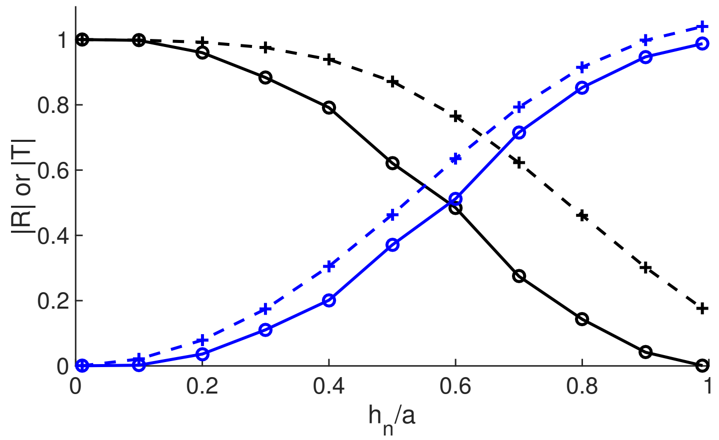

Figure 3.8 – Scattering by a notch of varying depth. Dashed cross lines: $|R_{1,1}|$ (blue) and $|T_{1,1}|$ (black) at point A ($f = 0.6$ MHz mm), with $|z_i - z_{\text{ref}}| = a$ and $N_{\Sigma_1} = N_{\Sigma_2} = 13$. Solid lines: $|R_{12,12}|$ (blue) and $|T_{12,12}|$ (black) at point B ($f = 22.89$ MHz mm) with $|z_i - z_{\text{ref}}| = 0.25a$ and $N_{\Sigma_1} = N_{\Sigma_2} = 40$. PML parameters: $d = h = a$, $\hat{\gamma} = 1 + 2\text{j}$.

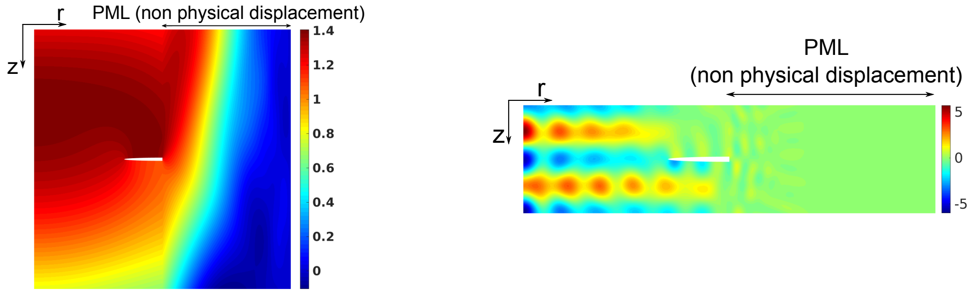

(a)

(b)

Figure 3.9 – Scattered field $\text{Re}(\mathbf{U}_z/a)$ by a notch of depth $h_n/a = 0.3$ at (a) point A ($f = 0.6$ MHz mm), (b) point B ($f = 22.89$ MHz mm) (same parameters as in Fig. 3.8).

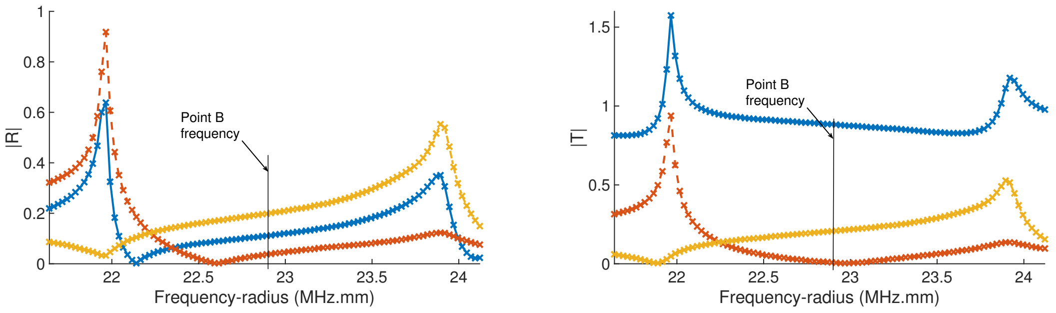

(a)

(b)

Figure 3.10 – (a) Reflection and (b) transmission coefficients of the 12th, 13th and 14th leaky modes around point B. Blue line: $|R_{12,12}|$, $|T_{12,12}|$, red dashed line: $|R_{13,12}|$, $|T_{13,12}|$, yellow dashed dotted line: $|R_{14,12}|$, $|T_{14,12}|$. Parameters: $d = h = a$, $\hat{\gamma} = 1+2\text{j}$, $h_n/a = 0.3$.

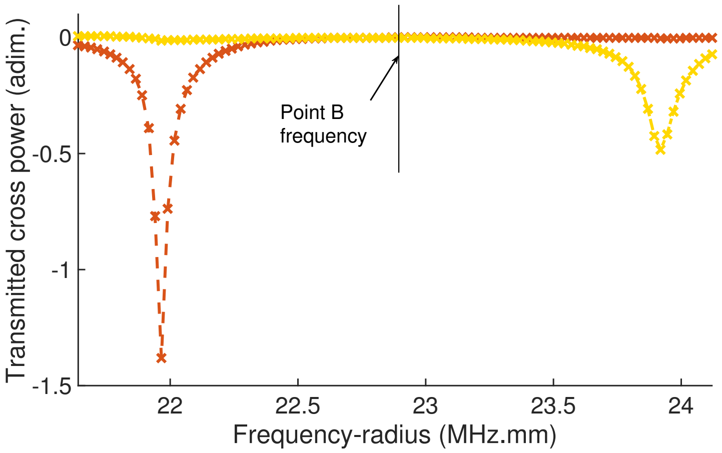

Figure 3.11 – Transmitted cross power $P_{12,13}$(red dashed line) and $P_{12,14}$ (yellow dashed dotted line). PML parameters: $d = h = a$, $\hat{\gamma} = 1 + 2\mathrm{j}$. Notch: $e_n/a = 0.025$, $h_n/a = 0.3$.

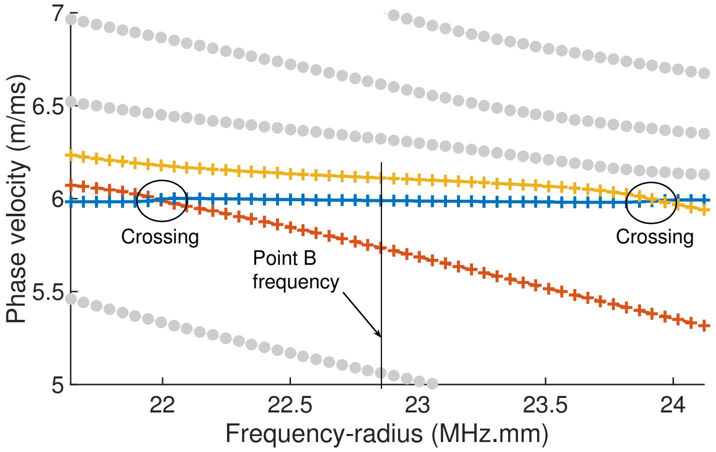

Figure 3.12 – Crossing of phase velocity curves. Blue line: 12th leaky mode, red dashed line: 13th leaky mode, yellow dashed dotted line: 14th leaky mode. PML parameters: $d = h = a$, $\hat{\gamma} = 1 + 2\mathrm{j}$.

Note that such a mode crossing behaviour can also be observed in viscoelastic waveguides, as mentioned *e.g.* in Refs. [94, 95]. Hence, a similar phenomenon is likely to occur in the scattering analysis of closed but lossy waveguides (as already discussed in Sec. 3.2.5, the lack of power orthogonality also concerns viscoelastic waveguides).

These results show that when there is no power orthogonality relationship between modes, an interpretation of results based solely on the individual scattering coefficients can be misleading. The post-processing of modal cross powers enables to identify the occurrence of strong interaction between modes (with no additional computational cost).

3.3.2.4 Influence of PML modes on the solution in the very near-field

Figure 3.13 shows the wavenumber spectrum computed at point A ($f = 0.6$ MHz mm) in the complex half-plane $\mathrm{Re}(ka) > 0$. The spectrum contains 13 leaky modes, including the

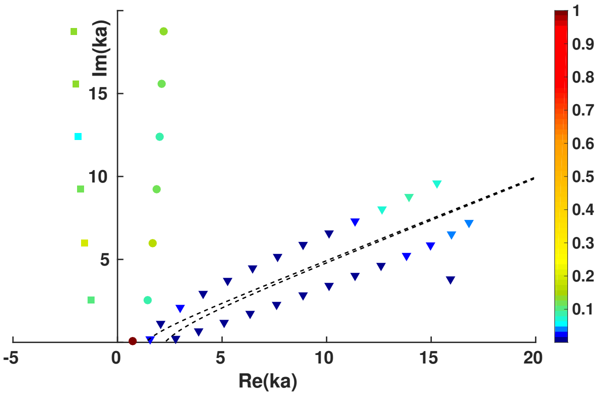

Figure 3.13 – Wavenumber spectrum ($N_{\Sigma_2} = 40$) of a viscoelastic steel waveguide embedded into viscoelastic cement grout computed with the PML waveguide formulation at point A ($f = 0.6\,\mathrm{MHz\,mm}$). Circles: forward leaky modes, squares: backward leaky modes, triangles: PML modes. Colormap: modal coefficients of transmitted modes retropropagated at $z = z_{\mathrm{ref}}$ for $h_n/a = 0.8$, normalized by the maximum value. PML parameters: $d = h = a, \hat{\gamma} = 1 + 2\mathrm{j}$.

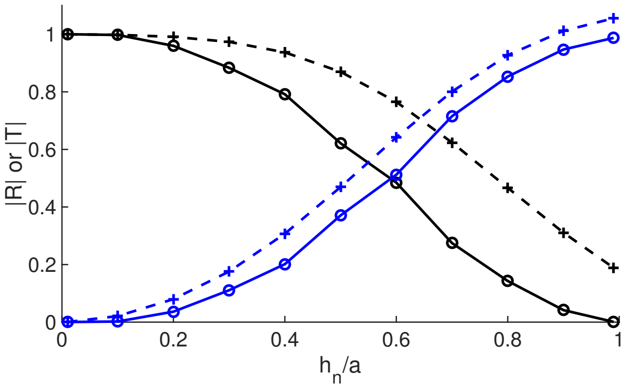

Figure 3.14 – Scattering by a notch of varying depth at $f = 0.6$ MHz.mm (point A) with $|z_i - z_{\mathrm{ref}}| = 0.25a$. Dashed cross lines: $|R_{1,1}|$ (blue) and $|T_{1,1}|$ (black) with $N_{\Sigma_1} = N_{\Sigma_2} = 13$ (leaky modes only). Solid lines: $|R_{1,1}|$ (blue) and $|T_{1,1}|$ (black) with $N_{\Sigma_1} = N_{\Sigma_2} = 40$. PML parameters: $d = h = a$, $\hat{\gamma} = 1 + 2\mathrm{j}$.

fundamental L(0,1) leaky mode, and 27 PML modes. Let us reduce the distance $|z_i - z_{\mathrm{ref}}|$ to $0.25a$ in order to reveal the contribution of PML modes on the solution in the very near-field of the notch. Reflection and transmission coefficients are displayed in Fig. 3.14. They have been obtained by retaining either all the modes ($N_{\Sigma_1} = N_{\Sigma_2} = 40$), either leaky modes only ($N_{\Sigma_1} = N_{\Sigma_2} = 13$). It can be observed that the contribution of PML modes is necessary to accurately recover the results of Fig. 3.8 (particularly for the reflection coefficient).

The colormap of Fig. 3.13 displays the modulus of the modal coefficients of the transmitted modes retropropagated at $z = z_{\mathrm{ref}}$, *i.e.* $|\alpha_{+m}\mathrm{e}^{+\mathrm{j}k_{+m}(z_{\mathrm{ref}}-z_2)}| \times \sqrt{|\mathrm{Re}(\overline{P}_{+m})|}$, for $h_n/a = 0.8$ (similar colormaps can be obtained for other notch depths or in reflection). It shows that among PML modes, the modes with the highest attenuations ($\mathrm{Im}(ka)$) bear the highest modal contributions to the solution, which is a characteristic near-field behaviour.

Therefore, the contribution of PML modes enables to improve the accuracy of results in the very near field. Their influence decreases as the distance to the notch increases, so that PML modes can eventually be neglected (as confirmed by Fig. 3.8).

Figure 3.13 also shows that another class of modes corresponding to high-attenuation leaky modes can significantly contribute to the near field. Similarly to PML modes, these modes enable to reconstruct the wave fields near the inhomogeneity and have been included in the modal expansions. The sign of the real part of the wavenumber of high-attenuation leaky modes can be either positive or negative. The latter case ($\mathrm{Re}(ka) < 0$) corresponds to backward leaky modes [11, 70]. As opposed to forward leaky modes, backward leaky modes decrease along the transverse direction (from a mathematical point of view, these modes are proper complex poles of the problem).

3.3.3 Reflection by an oblique break

The open waveguide, similar to the one considered in the previous sections, is now damaged by an oblique complete break of the core. The width of the break is set to $e_n/a = 0.25$ and its angle of inclination varies. Contrary to the previous cases, the scattering problem must now be solved with the three-dimensional formulation of the hybrid method. The computational domain is depicted in Fig. 3.15a. Because of the symmetry of the problem, only half of the waveguide can be considered. The embedding medium is truncated with a PML of parabolic attenuation profile according to Eq. (3.32).

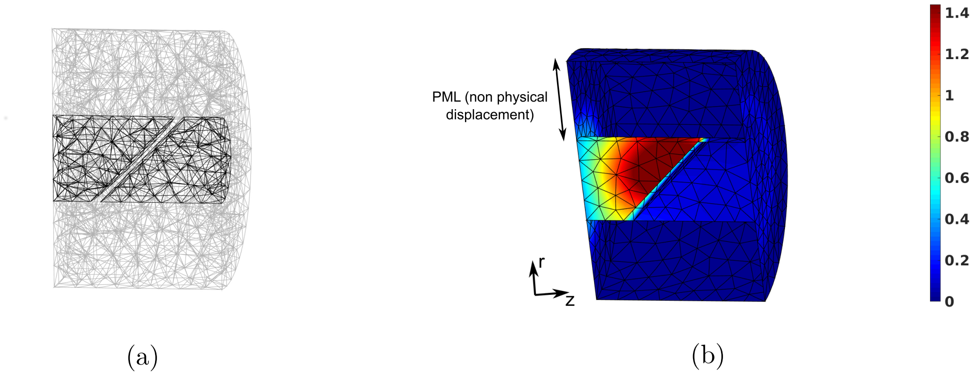

(a) (b)

Figure 3.15 – Oblique break of the core with an inclination of 45°. (a) Finite element mesh for $|z_i - z_{\mathrm{ref}}| = 2a$ (black: physical domain, grey: PML domain); (b) Scattered field $|\mathbf{U}_z/a|$ at $f = 0.6$ MHz mm. PML parameters: $d = a$, $h = 2a$, $\hat{\gamma} = 2 + 4\mathrm{j}$.

The problem is solved around point A between 0.4 MHz mm and 0.8 MHz mm, which includes the fundamental longitudinal leaky mode L(0,1) and the fundamental flexural leaky mode F(1,1). The behaviour of the F(1,1) mode is more complex than the L(0,1) mode and the following PML parameters have been chosen in order to obtain acceptable results: $d = a$, $h = 2a$, $\hat{\gamma} = 2 + 4\mathrm{j}$. In the following, the scattering of both modes is studied for an incident L(0,1) leaky mode.

In order to limit the contribution of PML modes, the inlet and the outlet cross-sections boundaries, Σ_1 and Σ_2, are set at distances $|z_i - z_{\mathrm{ref}}| = 2a$ (*i.e.* not too close to the break). The domain is meshed with 10-nodes tetrahedral elements, yielding roughly 15 000 dofs with 1290 dofs on each cross-section. The number of modes retained in the modal expansions has been set to $N_{\Sigma_1} = N_{\Sigma_2} = 100$. Numerical tests have shown that the contribution

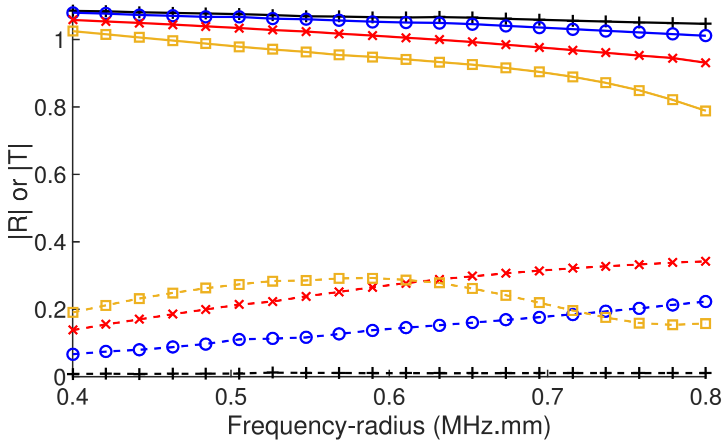

Figure 3.16 – Scattering by an oblique break of the core for different inclination angles (three-dimensional problem). $|R_{\mathrm{L}(0,1),\mathrm{L}(0,1)}|$: 0° (dark cross line), 15° (blue circle line), 30° (red cross line), 45° (yellow square line). $|R_{\mathrm{F}(1,1),\mathrm{L}(0,1)}|$: 0° (dark cross dashed line), 15° (blue circle dashed line), 30° (red cross dashed line), 45° (yellow square dashed line).

of higher order modes on the results was negligible (as explained previously, more modes would have been necessary with cross-section boundaries closer to the inhomogeneity).

Figure 3.16 displays the reflection coefficients of both modes for four angles of inclination (0°, 15°, 30° and 45°). The transmission coefficients, not shown here for conciseness, remain rather low.

For a break perpendicular to the waveguide axis (angle of 0°), the reflection coefficient of the L(0,1) leaky mode favourably matches with the axisymmetric notch test case (see Fig. 3.8 for $h_n/a = 1$). Note that the value of the F(1,1) reflection coefficient is weak but non-null. According to the geometry, modal conversion into the flexural mode should not occur for an angle of 0°. This can be attributed to the moderate accuracy of flexural mode computation in the three-dimensional model (with additional computational cost, this could be improved either by mesh refinement or by setting a thicker PML).

When the angle increases from 0 to 30°, the reflection coefficient of the L(0,1) mode monotonically decreases while the reflection coefficient of the F(1,1) mode monotonically increases. As expected, the modal conversion from the longitudinal mode into the flexural mode becomes important as the angle increases. At 45°, the behaviour of the flexural mode is no longer monotonic and varies with the frequency. As an example, the corresponding scattered field is depicted in Fig. 3.15b for $f = 0.6$ MHz mm.

3.4 Conclusion

A PML-based hybrid method has been proposed for the numerical modelling of wave scattering by inhomogeneities in open waveguides. The modal representation of the fields propagating in the undamaged part of the waveguide involves three types of modes: trapped modes, leaky modes and PML modes.

Comparisons with literature results have shown that the numerical method enables to obtain a good approximation of the scattering behaviour in open waveguides.

Based on the modal biorthogonality property, it has been shown that the modal cross power does not vanish in general in open waveguides. In particular, the modal cross-power can be significant when mode-crossing phenomena occur. This is likely to complicate the analysis of scattering phenomena.

A particular attention has been given to the influence of PML modes on the solution, and particularly on the scattering behaviour of leaky modes. In the very far-field, only the contribution of PML modes can accurately reconstruct the long-term diffraction of the field. Yet such a configuration is of less interest in the context of hybrid methods, the aim of which is to reduce the computation to the near-field of the inhomogeneity.

In the very near field, it has been shown that the contribution of PML modes can be not negligible and that leaky modes may be not sufficient to obtain accurate results. The weight of the PML modes contribution depends on the distance between the inhomogeneity and the transparent cross-section boundaries of the FE model. Therefore, the accuracy of the hybrid method has to be carefully checked by varying the distance of the boundaries and the number of modes involved in the modal expansions. For three-dimensional problems, it can be useful to set the transparent boundaries sufficiently far away from the inhomogeneity in order to avoid the computation of many PML modes.

As a final remark, the near-field behaviour of PML modes may raise feasibility issues for mode-matching methods when applied to open waveguides. Mode-matching methods are based on modal expansions set at the inhomogeneity position (see *e.g.* Ref. [96] in closed waveguides), which may require the computation of a high number of PML modes to achieve accurate results.

Appendices

3.A Axisymmetrical PML waveguide formulation

Let us consider an axisymmetric waveguide. The formulation (3.1) is written in the cylindrical coordinate system $(\tilde{r}, \theta, z)$. The cross-section can be reduced to the radial direction $\tilde{r}$. The core of the waveguide has a radius $\tilde{r} = a$, and can be multilayered. Only axisymmetric solutions are considered, such that $\partial(.)/\partial\theta = 0$ and $\tilde{u}_\theta = 0$. Hence the displacement field in Eq. (3.1) is expressed as $\tilde{\mathbf{u}} = [\tilde{u}_r \ \tilde{u}_z]^{\mathrm{T}}$ and only depends on the variables $\tilde{r}$ and z. The strain field is given by $\tilde{\boldsymbol{\epsilon}} = [\tilde{\epsilon}_{rr} \ \tilde{\epsilon}_{\theta\theta} \ \tilde{\epsilon}_{zz} \ 2\tilde{\epsilon}_{rz}]$.

Using Eq. (3.2), the change of variable (3.3) is applied to Eq. (3.1). In the strain-displacement relation (3.13), the operators $\mathbf{L}_S$ and $\mathbf{L}_z$ are now given by:

$$\mathbf{L}_S = \left(\frac{1}{\gamma} \begin{bmatrix} 1 & 0 \\ 0 & 0 \\ 0 & 0 \\ 0 & 1 \end{bmatrix} \frac{\partial}{\partial r} + \begin{bmatrix} 0 & 0 \\ 1 & 0 \\ 0 & 0 \\ 0 & 0 \end{bmatrix} \frac{1}{\tilde{r}} \right), \mathbf{L}_z = \begin{bmatrix} 0 & 0 \\ 0 & 0 \\ 0 & 1 \\ 1 & 0 \end{bmatrix}. \tag{3.33}$$

Then, a one-dimensional FE discretization is applied along the radial direction, yielding the following interpolation on each element:

$$\mathbf{u}^e(r, \omega) = \mathbf{N}^e_\Sigma(r)\boldsymbol{\Phi}^e. \tag{3.34}$$

$\mathbf{N}^e_\Sigma(r)$ is the matrix of interpolation one-dimensional functions. $\boldsymbol{\Phi}^e(\omega)$ is the vector of nodal displacements. The final eigenproblem is identical to Eq. (3.14), where the element matrices are given by Eq.(3.15) with $\mathrm{d}S = 2\pi r \mathrm{d}r$. Under the assumption used in this appendix, $\mathbf{C}$ is reduced to a four-by-four matrix. For instance, the matrix $\mathbf{C}$ for an isotropic material is:

$$\mathbf{C} = \begin{bmatrix} \lambda + 2\mu & \lambda & \lambda & 0 \\ \lambda & \lambda + 2\mu & \lambda & 0 \\ \lambda & \lambda & \lambda + 2\mu & 0 \\ 0 & 0 & 0 & \mu \end{bmatrix}. \tag{3.35}$$

where λ and μ are Lamé parameters.

3.B Total cross-section power flow

The total-time averaged power flow across the whole cross-section is given by:

$$\Pi_T = \mathrm{Re}(-\frac{\mathrm{j}\omega}{2}\mathbf{U}^*_\Sigma\mathbf{F}_\Sigma), \tag{3.36}$$

$$= \frac{\mathrm{j}\omega}{4}(\mathbf{F}^*_\Sigma\mathbf{U}_\Sigma - \mathbf{U}^*_\Sigma\mathbf{F}_\Sigma). \tag{3.37}$$

Considering the modal expansions of the fields $\mathbf{U}_\Sigma$ and $\mathbf{F}_\Sigma$, one gets:

$$\Pi_T = \frac{\mathrm{j}\omega}{4}\left(\sum_{n=-N}^{N} \alpha^*_n \mathbf{F}^*_n \sum_{m=-N}^{N} \alpha_m \mathbf{U}_m - \sum_{n=-N}^{N} \alpha^*_n \mathbf{U}^*_n \sum_{m=-N}^{N} \alpha_m \mathbf{F}_m \right), \tag{3.38}$$

$$= \frac{\mathrm{j}\omega}{4}\left(\sum_{m=-N}^{N} |\alpha_m|^2 (\mathbf{F}^*_m\mathbf{U}_m - \mathbf{U}^*_m\mathbf{F}_m) + \sum_{m=-N}^{N}\sum_{n\neq m} \alpha^*_n\alpha_m(\mathbf{F}^*_n\mathbf{U}_m - \mathbf{U}^*_n\mathbf{F}_m) \right). \tag{3.39}$$

From the above equation, the modal cross-power $P_{m,n} = \frac{\mathrm{j}\omega}{4}(\mathbf{F}_n^* \mathbf{U}_m - \mathbf{U}_n^* \mathbf{F}_m)$ can be identified. For $m = n$, it can be checked that $P_{m,m} = \frac{\omega}{2}\mathrm{Im}(\mathbf{U}_m^* \mathbf{F}_m) = \mathrm{Re}(P_m)$. Finally, the total-time averaged power flow can then be written:

$$\Pi_T = \sum_{m=-N}^{N} |\alpha_m|^2 \mathrm{Re}(P_m) + \sum_{m=-N}^{N} \sum_{n \neq m} \alpha_n^* \alpha_m P_{m,n}. \tag{3.40}$$

3.C Filtering of PML modes

It can be necessary to filter out PML modes, *e.g.* for the visualization of dispersion curves where only leaky and trapped modes are of interest. In this chapter, we use the filtering criterion proposed in Chap. 2. It is based on the ratio of the imaginary part over the modulus of the kinetic energy, defined from Eq. (3.25) but integrating the whole cross-section (*i.e.* including the PML, so that the overbar has to be discarded in Eq. (3.25)). The modes are retained if they fulfil the following criterion:

$$1 - \frac{\mathrm{Im}(T_m)}{|T_m|} > \eta_{\min}, \tag{3.41}$$

where $0 < \eta_{\min} < 1$ is a user-defined parameter.

Chapter 4

Gradient-based imaging of waveguides using an adjoint approach

4.1 Introduction

The localization and the characterization of unknown obstacles (defects) embedded into a structure from a measure of the scattered field are of great interest for various domains, including NDE. This so-called inverse scattering problem has been studied for a long time in acoustics, electromagnetics and elastodynamics. A number of methods have been thus proposed in the literature. They are often distinguished between quantitative and qualitative methods.

Quantitative methods can give extended information on the obstacles. These methods include approaches based either on linearization techniques [97] or on non-linear optimization procedures [98]. The former relies on strong assumptions seldom verified in practice, which limits its application to practical cases. The latter requires precise *a priori* information to serve as an initial guess, which is not always available in practice. Furthermore, non-linearization optimization procedures are generally based on local iterative algorithms, yielding a high computational cost of the methods.

In this work, we focus on the so-called qualitative sampling techniques [99, 100]. These methods are based on the development of an imaging function which varies on the spatially sampled domain and takes great values at the defect positions, thereby revealing their location. This process is qualitative (only limited information about the obstacle is sought) and non-iterative, which makes these methods interesting for practical applications. Let us mention here the Linear Sampling Method [101] (recently applied to elastic waveguides in Ref. [102]) and the topological imaging method [20, 21]. This chapter focuses on the latter.

The key point of topological imaging is the topological gradient (or topological sensitivity). This function gives the sensitivity of a misfit functional to the inclusion of a vanishing cavity inside a reference medium. It originates from shape optimization in elastostatics [103, 104]. Topological gradient has then been adapted as an imaging function for defect localization in time-domain elastodynamics in Ref. [20]. A mathematical framework has also been developed in the frequency domain [105] and in the time-domain [21]. Subsequent works can be found in Refs. [99, 106] for instance. Besides insightful connections have been drawn out with other methods such as time-reversal in ultrasonics [20], and with methods based on an adjoint approach like the Full-Waveform Inversion in geophysics [20] and the constrained optimization theory [107].

In practice, the first step of topological imaging is the emission of waves and the measurement of the scattered field in a real medium containing defects. Then, two problems are simulated in the reference medium, generally a defect-free medium. In the forward problem, the experimental source is simulated. In the adjoint problem, the source is the time-reversed residue. The latter is the difference between the displacements measured in the forward problem and in the experiments, at the same location. The residue is hence a characteristic of the defects embedded into the real medium. The image is finally constructed by the combination of the forward and adjoint fields, according to the topological gradient formulation specific of the sought defects. It naturally reveals the location of the defects. Let us remark that various simplified formulations of the gradient have been proposed throughout the literature [22, 23, 108] for a faster image processing, which demonstrates the flexibility of the method.

The specific case of waveguides, and particularly of open waveguides, has been barely considered with topological imaging. Contrary to bulk waves, guided waves can be multimodal and dispersive. In case of viscoelasticity or leakage into an embedding medium, waves are also attenuated. Up to our knowledge, only the case of a monomodal, dispersive and non-attenuated wave field in a plate has been treated in the literature (see Ref. [22]). It remains necessary to assess the robustness of the method when a more complex wavefield is emitted.

Besides open waveguides are generally of limited access, which restricts the configuration of measurement to backscattering (reflection) only, and most often at the surface of the waveguide rather than inside its section. Yet large arrays of transducers are generally used in topological imaging to obtain a full-field measurement configuration. For instance, a 128 transducers array is used for a plate in Ref. [22]. In that case, the method accurately locates through-thickness holes with a resolution of one wavelength (the image is a top view of the plate). In this work, we want to investigate the ability of the method to locate one or several defects both along the axis and along the transverse direction (*i.e.* inside the section of the waveguide), so that the image is a cross-section view of the waveguide.

The aim of this chapter is to apply topological imaging to an open waveguide configuration. As for theoretical background, a general framework based on constrained optimization theory is recalled for inverse problems in elastodynamics in Sec. 4.2. The special case of topological imaging method is then considered in Sec. 4.3. The various theoretical and empirical formulations of the topological gradient are recalled. The implementation of the method for waveguide imaging is described. Thanks to the numerical method presented in Chap. 3, a real medium containing defects can be simulated. Moreover, the forward and adjoint fields can be efficiently computed with the numerical method presented in Chap. 2. As a first step, a circular closed waveguide test case is considered in Sec. 4.4. The various simplified formulations of the gradient are compared and discussed. Furthermore, both monomodal and multimodal wavefields are considered using several measurement configurations. The multimodal case is particularly discussed. Different types of defects are simulated to assess the accuracy of the method. Finally, preliminary results are presented for an open waveguide case in Sec. 4.5.

4.2 General framework: a constrained optimization problem

In this section, a general framework based on constrained optimization theory is recalled for inverse problems in elastodynamics. It is further applied to topological imaging in Sec. 4.3.

4.2.1 Description of the minimization problem

Let us consider an elastic medium Ω, which external boundary is $\partial\Omega$. The latter is divided into surfaces S_N and S_D ($\partial\Omega = S_N \cup S_D$) on which Neumann and Dirichlet boundary conditions are applied. The wave field $\mathbf{u}(\mathbf{x}, \mathbf{m}, \omega)$ is the solution of the following equations:

$$\mathbf{A}(\mathbf{x},\mathbf{m},\omega)\mathbf{u}(\mathbf{x},\mathbf{m},\omega) = \mathbf{0}, \quad \forall \mathbf{x} \in \Omega, \tag{4.1}$$

$$\mathbf{u}(\mathbf{x},\mathbf{m},\omega) = \mathbf{u}_D, \quad \forall \mathbf{x} \in S_D, \tag{4.2}$$

$$\sigma\left(\mathbf{u}(\mathbf{x},\mathbf{m},\omega)\right) \cdot \mathbf{n} = \boldsymbol{\sigma}_N, \quad \forall \mathbf{x} \in S_N, \tag{4.3}$$

where $\mathbf{A}(\mathbf{x},\mathbf{m},\omega)\mathbf{u}(\mathbf{x},\mathbf{m},\omega) = \nabla \cdot \sigma\left(\mathbf{u}(\mathbf{x},\mathbf{m},\omega)\right) + \rho\omega^2\mathbf{u}(\mathbf{x},\mathbf{m},\omega)$. The stress tensor is defined by $\sigma = C : \epsilon$, where C is the tensor of material properties and ϵ is the strain tensor. The vector $\mathbf{m}(\mathbf{x})$ describes the values of the model parameters (*e.g.* material properties) at each point $\mathbf{x}$ in the domain Ω. The operator $\mathbf{A}$ then depends on $\mathbf{m}(\mathbf{x})$ and ω, and so does naturally the solution $\mathbf{u}$.

Let us consider a real medium Ω_r in which the properties $\mathbf{m}(\mathbf{x})$ are unknown and to be identified. For given sources (assumed identical to Eqs. (4.2) and (4.3)), the true wavefield $\mathbf{u}_{\text{obs}}$ is measured on the observation surface $S_{\text{obs}} \subseteq S_N$ of Ω_r. Assuming that the medium Ω is perfectly similar to the real medium Ω_r except for the properties to be identified, the inverse problem can be formulated as: find the optimal model parameters $\mathbf{m}$ which minimize the cost-functional,

$$j(\mathbf{m}) = \mathrm{J}(\mathbf{u}) = \frac{1}{2}\int_{\mathbb{R}^+}\int_{S_{\text{obs}}} |\mathbf{u}(\mathbf{x},\mathbf{m},\omega) - \mathbf{u}_{\text{obs}}(\mathbf{x},\omega)|^2 \mathrm{d}S_{\text{obs}}\mathrm{d}\omega, \tag{4.4}$$

where $\mathbf{u}(\mathbf{x},\mathbf{m},\omega)$ is the solution of Eqs. (4.1)–(4.3). If the inverse problem is well-posed, the unknown properties of the real medium are correctly identified at the end of the minimization process.

For the conciseness of notations in Sec. 4.2, calculations will be made at only one angular frequency, so that the functional becomes:

$$j(\mathbf{m}) = \mathrm{J}(\mathbf{u}) = \frac{1}{2}\int_{S_{\text{obs}}} |\mathbf{u}(\mathbf{x},\mathbf{m}) - \mathbf{u}_{\text{obs}}(\mathbf{x})|^2 \mathrm{d}S_{\text{obs}}. \tag{4.5}$$

Several frequencies can be considered by performing a discrete sum or an integral over the frequencies of interest.

4.2.2 Lagrangian formulation of the problem

The minimization problem (4.5) can be conveniently formulated in the framework of constrained optimization, described *e.g.* in Refs. [109–111]. The basic idea is to reformulate the problem as the minimization of Eq. (4.5) while satisfying the constraints given by Eqs. (4.1)–(4.3).

Let us define the Lagrangian associated to the problem:

$$L(\boldsymbol{\xi},\boldsymbol{\lambda}_1,\boldsymbol{\lambda}_2,\boldsymbol{\lambda}_3,\mathbf{m}) = \mathrm{Re}(\mathrm{J}(\boldsymbol{\xi}) + \langle\boldsymbol{\lambda}_1,\mathbf{A}(\mathbf{m})\boldsymbol{\xi}\rangle_\Omega + \langle\boldsymbol{\lambda}_2,\boldsymbol{\xi}-\mathbf{u}_D\rangle_{S_D} + \langle\boldsymbol{\lambda}_3,\sigma(\boldsymbol{\xi})\cdot\mathbf{n}-\sigma_N\rangle_{S_N}). \tag{4.6}$$

The real part must be considered because complex-valued functionals are involved in Eq. (4.6) [109, 112]. The inner product is given by $\langle\mathbf{a},\mathbf{b}\rangle_V = \int_V \bar{\mathbf{a}}\cdot\mathbf{b}\mathrm{d}V$. $\boldsymbol{\xi}(\mathbf{x})$ belongs to the state-variable space and is independent on $\mathbf{m}(\mathbf{x})$, which means that it does not necessarily satisfy Eqs. (4.1)–(4.3) at this stage. The $\boldsymbol{\lambda}_i(\mathbf{x})$ are Lagrange multipliers associated to each constraint.

As detailed hereafter, from the Lagrangian (4.6):

- the differentiation with respect to the state-variable $\boldsymbol{\xi}$ yields the adjoint equations,
- the differentiation with respect to the Lagrange multipliers $\boldsymbol{\lambda}_i$ yields the forward equations,
- the differentiation with respect to each component of the vector of model parameters $\mathbf{m}$ enables to naturally identify the so-called gradients (or Fréchet derivatives [113]) of the cost-functional, denoted $\delta j/\delta \mathbf{m}$. It will be shown that the latter can be expressed as a function of the solutions of the adjoint and forward equations.

The gradient of the cost-functional can then be used as a descent direction in iterative procedures, *e.g.* following the gradient-conjugate method, to minimize the cost-functional and to identify the true value of $\mathbf{m}(\mathbf{x})$.

4.2.3 Derivation of the adjoint equations

The differentiation of the Lagrangian with respect to $\boldsymbol{\xi}$ yields:

$$\begin{aligned} L(\boldsymbol{\xi}+\delta\boldsymbol{\xi},\boldsymbol{\lambda}_1,\boldsymbol{\lambda}_2,\boldsymbol{\lambda}_3,\mathbf{m}) - L(\boldsymbol{\xi},\boldsymbol{\lambda}_1,\boldsymbol{\lambda}_2,\boldsymbol{\lambda}_3,\mathbf{m}) = \mathrm{Re}\Big(& \mathrm{J}(\boldsymbol{\xi}+\delta\boldsymbol{\xi}) - \mathrm{J}(\boldsymbol{\xi}) + \langle \boldsymbol{\lambda}_1, \mathbf{A}\delta\boldsymbol{\xi}\rangle_\Omega \\ & + \langle \boldsymbol{\lambda}_2, \delta\boldsymbol{\xi}\rangle_{S_D} + \langle \boldsymbol{\lambda}_3, \sigma(\delta\boldsymbol{\xi})\cdot\mathbf{n}\rangle_{S_N}\Big). \end{aligned} \tag{4.7}$$

The differentiation of the functional $J(\boldsymbol{\xi})$ is readily given by:

$$\mathrm{J}(\boldsymbol{\xi}+\delta\boldsymbol{\xi}) - \mathrm{J}(\boldsymbol{\xi}) = \mathrm{Re}\Big(\int_{S_{\mathrm{obs}}} \delta\boldsymbol{\xi}\cdot(\overline{\boldsymbol{\xi}-\mathbf{u}_{\mathrm{obs}}})\mathrm{d}S_{\mathrm{obs}}\Big) + O(|\delta\boldsymbol{\xi}|^2). \tag{4.8}$$

where the overline stands for the complex conjugate. As for $\langle \boldsymbol{\lambda}_1, \mathbf{A}\delta\boldsymbol{\xi}\rangle_\Omega$, integrating by parts gives:

$$\langle \boldsymbol{\lambda}_1, \mathbf{A}\delta\boldsymbol{\xi}\rangle_\Omega = \int_{\partial\Omega} \overline{\boldsymbol{\lambda}_1}\cdot(\sigma(\delta\boldsymbol{\xi})\cdot\mathbf{n})\mathrm{d}\partial\Omega - \int_\Omega (\nabla\overline{\boldsymbol{\lambda}_1} : \sigma(\delta\boldsymbol{\xi}) - \rho\omega^2\delta\boldsymbol{\xi}\cdot\overline{\boldsymbol{\lambda}_1})\mathrm{d}\Omega. \tag{4.9}$$

From the symmetry of σ and C, one can write:

$$\begin{aligned} \int_\Omega \nabla\overline{\boldsymbol{\lambda}_1} : \sigma(\delta\boldsymbol{\xi})\mathrm{d}\Omega &= \int_\Omega \epsilon(\overline{\boldsymbol{\lambda}_1}) : \sigma(\delta\boldsymbol{\xi})\mathrm{d}\Omega, && (4.10) \\ &= \int_\Omega \epsilon(\overline{\boldsymbol{\lambda}_1}) : C : \epsilon(\delta\boldsymbol{\xi})\mathrm{d}\Omega, && (4.11) \\ &= \int_\Omega \nabla\delta\boldsymbol{\xi} : \sigma(\overline{\boldsymbol{\lambda}_1})\mathrm{d}\Omega. && (4.12) \end{aligned}$$

Integrating by parts a second time yields finally:

$$\langle \boldsymbol{\lambda}_1, \mathbf{A}\delta\boldsymbol{\xi}\rangle_\Omega = \int_\Omega \delta\boldsymbol{\xi}\cdot(\nabla\cdot\sigma(\overline{\boldsymbol{\lambda}_1}) + \rho\omega^2\overline{\boldsymbol{\lambda}_1})\mathrm{d}\Omega + \int_{\partial\Omega} (\overline{\boldsymbol{\lambda}_1}\cdot(\sigma(\delta\boldsymbol{\xi})\cdot\mathbf{n}) - \delta\boldsymbol{\xi}\cdot(\sigma(\overline{\boldsymbol{\lambda}_1})\cdot\mathbf{n}))\mathrm{d}\partial\Omega. \tag{4.13}$$

Equating Eq. (4.7) to zero for any $\delta\boldsymbol{\xi}$ gives the following equations:

$$\begin{aligned}
\mathbf{A}\overline{\boldsymbol{\lambda}_1} &= \mathbf{0}, \quad \forall \mathbf{x} \in \Omega, && (4.14)\\
\overline{\boldsymbol{\lambda}_1} &= \mathbf{0}, \quad \forall \mathbf{x} \in S_D, && (4.15)\\
\sigma(\overline{\boldsymbol{\lambda}_1}) \cdot \mathbf{n} &= \mathbf{0}, \quad \forall \mathbf{x} \in S_N \backslash S_{\text{obs}}, && (4.16)\\
\sigma(\overline{\boldsymbol{\lambda}_1}) \cdot \mathbf{n} &= \overline{\boldsymbol{\xi} - \mathbf{u}_{\text{obs}}}, \quad \forall \mathbf{x} \in S_{\text{obs}}, && (4.17)\\
\overline{\boldsymbol{\lambda}_2} &= \sigma(\overline{\boldsymbol{\lambda}_1}) \cdot \mathbf{n}, \quad \forall \mathbf{x} \in S_D, && (4.18)\\
\overline{\boldsymbol{\lambda}_3} &= -\overline{\boldsymbol{\lambda}_1}, \quad \forall \mathbf{x} \in S_N. && (4.19)
\end{aligned}$$

These equations are the *adjoint equations*. We recall that the solutions depend on $\mathbf{x}$, ω, and the model parameters $\mathbf{m}$. As a side remark, the introduction of Lagrange multipliers $\boldsymbol{\lambda}_2$ and $\boldsymbol{\lambda}_3$ may be not necessary if Neumann and Dirichlet boundary conditions are accounted for in the definition of the dual space of $\boldsymbol{\lambda_1}$ [110].

4.2.4 Derivation of the forward equations

The differentiation of L with respect to a small variation $\delta\boldsymbol{\lambda}_1$ yields:

$$L(\boldsymbol{\xi}, \boldsymbol{\lambda}_1 + \delta\boldsymbol{\lambda_1}, \boldsymbol{\lambda}_2, \boldsymbol{\lambda}_3, \mathbf{m}) - L(\boldsymbol{\xi}, \boldsymbol{\lambda}_1, \boldsymbol{\lambda}_2, \boldsymbol{\lambda}_3, \mathbf{m}) = \text{Re}\big(\langle \delta\boldsymbol{\lambda}_1, \mathbf{A}\boldsymbol{\xi} \rangle_\Omega\big). \tag{4.20}$$

The differentiation of L with respect to a small variation $\delta\boldsymbol{\lambda}_2$ yields:

$$L(\boldsymbol{\xi}, \boldsymbol{\lambda}_1, \boldsymbol{\lambda}_2 + \delta\boldsymbol{\lambda}_2, \boldsymbol{\lambda}_3, \mathbf{m}) - L(\boldsymbol{\xi}, \boldsymbol{\lambda}_1, \boldsymbol{\lambda}_2, \boldsymbol{\lambda}_3, \mathbf{m}) = \text{Re}\big(\langle \delta\boldsymbol{\lambda}_2, \boldsymbol{\xi} - \mathbf{u}_D \rangle_{S_D}\big). \tag{4.21}$$

The differentiation of L with respect to a small variation $\delta\boldsymbol{\lambda}_3$ yields:

$$L(\boldsymbol{\xi}, \boldsymbol{\lambda}_1, \boldsymbol{\lambda}_2, \boldsymbol{\lambda}_3 + \delta\boldsymbol{\lambda}_3, \mathbf{m}) - L(\boldsymbol{\xi}, \boldsymbol{\lambda}_1, \boldsymbol{\lambda}_2, \boldsymbol{\lambda}_3, \mathbf{m}) = \text{Re}\big(\langle \delta\boldsymbol{\lambda}_3, \sigma(\boldsymbol{\xi}) \cdot \mathbf{n} - \sigma_N \rangle_{S_N}\big). \tag{4.22}$$

Equating these equations to zero for any variations $\delta\boldsymbol{\lambda}_i$ gives:

$$\begin{aligned}
\mathbf{A}\boldsymbol{\xi} &= \mathbf{0}, \quad \forall \mathbf{x} \in \Omega, && (4.23)\\
\boldsymbol{\xi} &= \mathbf{u}_D, \quad \forall \mathbf{x} \in S_D, && (4.24)\\
\sigma(\boldsymbol{\xi}) \cdot \mathbf{n} &= \boldsymbol{\sigma}_N, \quad \forall \mathbf{x} \in S_N. && (4.25)
\end{aligned}$$

These equations are the *forward equations* corresponding to Eqs. (4.1)–(4.3), so that one can write $\boldsymbol{\xi} = \mathbf{u}(\mathbf{x}, \mathbf{m}, \omega)$.

4.2.5 Derivation of the gradient

For $\boldsymbol{\xi} = \mathbf{u}$ (solution of the forward equations), the Lagrangian reduces to the cost-functional:

$$L(\mathbf{u}, \boldsymbol{\lambda}_1, \boldsymbol{\lambda}_2, \boldsymbol{\lambda}_3, \mathbf{m}) = \text{Re}(\text{J}(\mathbf{u})) = j(\mathbf{m}). \tag{4.26}$$

Therefore, the variations of the functional can be calculated as follows:

$$\begin{aligned}
j(\mathbf{m} + \delta\mathbf{m}) - j(\mathbf{m}) &= L(\mathbf{u}, \boldsymbol{\lambda}_1, \boldsymbol{\lambda}_2, \boldsymbol{\lambda}_3, \mathbf{m} + \delta\mathbf{m}) - L(\mathbf{u}, \boldsymbol{\lambda}_1, \boldsymbol{\lambda}_2, \boldsymbol{\lambda}_3, \mathbf{m}), && (4.27)\\
&= \text{Re}\big(\langle \boldsymbol{\lambda}_1, \mathbf{A}(\mathbf{m} + \delta\mathbf{m})\mathbf{u} - \mathbf{A}(\mathbf{m})\mathbf{u} \rangle_\Omega\big). && (4.28)
\end{aligned}$$

For any functional j, the gradient $\frac{\delta j}{\delta \mathbf{m}}$ is defined by: $\langle \delta \mathbf{m}, \frac{\delta j}{\delta \mathbf{m}} \rangle_\Omega = j(\mathbf{m} + \delta \mathbf{m}) - j(\mathbf{m})$. $\frac{\delta j}{\delta \mathbf{m}}(\mathbf{x})$ stands for the sensitivity of the functional with respect to a variation of $\mathbf{m}(\mathbf{x})$. As shown by Eq. (4.28), finding $\frac{\delta j}{\delta \mathbf{m}}$ requires to evaluate the variations $\mathbf{A}(\mathbf{m}+\delta\mathbf{m})\mathbf{u} - \mathbf{A}(\mathbf{m})\mathbf{u}$.

We recall that the quantity $\frac{\delta j}{\delta \mathbf{m}}$ is typically used in iterative process and gradient-like algorithms to minimize the cost-functional. Hence, the medium Ω has to be viewed as the medium of the current iteration (*i.e.* updated from the results of the previous iteration). At the first iteration, the medium corresponds to a reference medium, denoted Ω_0 in the following. It is then necessary to define an arbitrary starting vector of model parameters $\mathbf{m}_0$, yielding the associated adjoint field $\overline{\boldsymbol{\lambda}_1}(\mathbf{x}, \mathbf{m_0}, \omega)$ and the forward field $\mathbf{u}(\mathbf{x}, \mathbf{m}_0, \omega)$.

4.2.5.1 Example of density identification

The determination of the density at each point of an elastic medium requires to derive the gradient of the functional for $\mathbf{m} = [\rho(\mathbf{x})]$.

One gets:

$$\mathbf{A}(\rho + \delta\rho)\mathbf{u} - \mathbf{A}(\rho)\mathbf{u} = \delta\rho\omega^2\mathbf{u}, \tag{4.29}$$

so that the differentiation of the Lagrangian is, from Eq. (4.28),

$$L(\mathbf{u}, \boldsymbol{\lambda}_1, \boldsymbol{\lambda}_2, \boldsymbol{\lambda}_3, \mathbf{m} + \delta\mathbf{m}) - L(\mathbf{u}, \boldsymbol{\lambda}_1, \boldsymbol{\lambda}_2, \boldsymbol{\lambda}_3, \mathbf{m}) = \mathrm{Re}\Big(\int_\Omega \delta\rho\omega^2\overline{\boldsymbol{\lambda}_1}.\mathbf{u}\mathrm{d}\omega\Big). \tag{4.30}$$

One can identify:

$$\frac{\delta j}{\delta \rho}(\mathbf{x}) = \mathrm{Re}\Big(\omega^2\overline{\boldsymbol{\lambda}_1}(\mathbf{x}, \rho(\mathbf{x}), \omega)).\mathbf{u}(\mathbf{x}, \rho(\mathbf{x}), \omega)\Big), \ \forall \mathbf{x} \in \Omega. \tag{4.31}$$

Equation (4.31) expresses the sensitivity of the functional j to small variations of density at each point $\mathbf{x}$ in the domain Ω.

4.2.5.2 Example of Lame's parameter identification in an isotropic medium

We set $\mathbf{m} = [\lambda(\mathbf{x}) \;\; \mu(\mathbf{x})]^{\mathrm{T}}$, where λ and μ are the Lame's parameters of an isotropic medium. The operator $\mathbf{A}$ can be written: $\mathbf{A}(\mathbf{m}) = \nabla \cdot (C(\mathbf{m}) : \epsilon) + \rho\omega^2$. It can be expressed as a function of Lame's parameters as follows: $\mathbf{A}(\lambda, \mu)\mathbf{u} = (\lambda + 2\mu)\nabla(\nabla \cdot \mathbf{u}) - \mu\nabla \times (\nabla \times \mathbf{u}) + \rho\omega^2$. Therefore, one gets:

$$\mathbf{A}(\mathbf{m} + \delta\mathbf{m})\mathbf{u} - \mathbf{A}(\mathbf{m})\mathbf{u} = \delta\lambda\nabla(\nabla \cdot \mathbf{u}) + \delta\mu(2\nabla(\nabla \cdot \mathbf{u}) - \nabla \times (\nabla \times \mathbf{u})) \tag{4.32}$$

The differentiation of L for small variations $\delta\lambda$ and $\delta\lambda$ is:

$$\begin{aligned} L(\mathbf{u}, \boldsymbol{\lambda}_1, \boldsymbol{\lambda}_2, \boldsymbol{\lambda}_3, \mathbf{m} + \delta\mathbf{m}) - L(\mathbf{u}, \boldsymbol{\lambda}_1, \boldsymbol{\lambda}_2, \boldsymbol{\lambda}_3, \mathbf{m}) = \mathrm{Re}\Big(\int_\Omega \overline{\boldsymbol{\lambda}_1} \cdot (\delta\lambda\nabla(\nabla \cdot \mathbf{u}) \\ + \delta\mu(2\nabla(\nabla \cdot \mathbf{u}) - \nabla \times (\nabla \times \mathbf{u}))\mathrm{d}\Omega\Big). \end{aligned} \tag{4.33}$$

One can identify:

$$\frac{\delta j}{\delta \lambda}(\mathbf{x}) = \mathrm{Re}\Big(\overline{\boldsymbol{\lambda}_1}(\mathbf{x}, \lambda(\mathbf{x}), \mu(\mathbf{x})) \cdot \nabla(\nabla \cdot \mathbf{u}(\mathbf{x}, \lambda(\mathbf{x}), \mu(\mathbf{x})))\Big), \tag{4.34}$$

$$\frac{\delta j}{\delta \mu}(\mathbf{x}) = \mathrm{Re}\Big(\overline{\boldsymbol{\lambda}_1}(\mathbf{x}, \lambda(\mathbf{x}), \mu(\mathbf{x})) \cdot (2\nabla(\nabla \cdot \mathbf{u}(\mathbf{x}, \lambda(\mathbf{x}), \mu(\mathbf{x}))) - \nabla \times (\nabla \times \mathbf{u}(\mathbf{x}, \lambda(\mathbf{x})\mu(\mathbf{x})))\Big). \tag{4.35}$$

Equations (4.34) and (4.35) express the sensitivity of the functional j to small variations of Lame's parameters $\lambda(\mathbf{x})$ and $\mu(\mathbf{x})$. Note that Eqs. (4.34) and (4.35) involve second-order derivatives. A more convenient formulation based on first-order derivatives can be obtained using an integration by part before differentiating (see *e.g.* Ref. [113]).

4.2.6 Comments on the adjoint equations

The adjoint field $\boldsymbol{\lambda}_1$ satisfies the relation $\mathbf{A}^\dagger \boldsymbol{\lambda}_1 = 0$, where the adjoint operator $\mathbf{A}^\dagger$ can be determined from the equality $\langle \boldsymbol{\lambda}_1, \mathbf{A}\boldsymbol{\xi} \rangle = \langle \mathbf{A}^\dagger \boldsymbol{\lambda}_1, \boldsymbol{\xi} \rangle$. If the operator is self-adjoint, $\mathbf{A}^\dagger = \mathbf{A}$. However, in case of viscoelastic or PML media, the operator is not self-adjoint and $\mathbf{A}^\dagger \neq \mathbf{A}$.

It is noteworthy that Eqs. (4.14)–(4.19) give the conjugate of the Lagrange multipliers, the operator $\mathbf{A}$ being the same as in the forward equations. This is very convenient, since a single model can then be used to compute the fields $\mathbf{u}$ and $\overline{\boldsymbol{\lambda}_1}$, which are then used to obtain the gradient.

The source boundary condition of the adjoint problem (Eq. (4.17)) is the conjugate of the residue $(\mathbf{u}(\mathbf{x}, \mathbf{m}, \omega) - \mathbf{u}_{\mathrm{obs}}(\mathbf{x}, \omega))$ on S_{obs}. Phase conjugation in the frequency domain corresponds to time-reversal in the time-domain [20]. In the time-domain, the adjoint problem is hence solved backwards in time. Besides, the multiplication in the frequency domain between the forward and the adjoint fields corresponds to a convolution in the time-domain.

4.3 The case of topological imaging

In this section, the inverse problem is a cavity identification problem. The topological gradient is consistently derived based on the general framework recalled in Sec. 4.2. The use of the gradient as an imaging function for the topological imaging method is further presented. The various empirical formulations of the gradient are recalled. The implementation of the method is then detailed in the specific case of waveguide imaging.

4.3.1 The inverse problem

Let us now consider the cavity-modified medium $\Omega = \Omega_0 \setminus B$, where B is a repartition of cavities (defects), bounded by the free surface Γ. The reference medium Ω_0 is called the healthy medium (defect-free). The following equations are satisfied:

$$\mathbf{A}(\mathbf{x},\Omega,\omega)\mathbf{u}(\mathbf{x},\Omega,\omega) = \mathbf{0}, \quad \forall \mathbf{x} \in \Omega, \tag{4.36}$$

$$\mathbf{u}(\mathbf{x},\Omega,\omega) = \mathbf{u}_D, \quad \forall \mathbf{x} \in S_D, \tag{4.37}$$

$$\sigma\left(\mathbf{u}(\mathbf{x},\Omega,\omega)\right) \cdot \mathbf{n} = \boldsymbol{\sigma}_N, \quad \forall \mathbf{x} \in S_N, \tag{4.38}$$

$$\sigma\left(\mathbf{u}(\mathbf{x},\Omega,\omega)\right) \cdot \mathbf{n} = \mathbf{0}, \quad \forall \mathbf{x} \in \Gamma. \tag{4.39}$$

The vector of model parameters $\mathbf{m}$ now describes the repartition of defects in the medium Ω (*i.e.* its topology), which is denoted by the dependence of $\mathbf{u}$ on Ω.

The real media $\Omega_r = \Omega_0 \setminus B_r$ contains the true repartition of defects B_r. The inverse problem becomes: find the repartition of cavities B which minimizes the cost-functional

$$j(\Omega) = \mathrm{J}(\mathbf{u}) = \frac{1}{2}\int_{\mathbb{R}^+}\int_{S_{\mathrm{obs}}} |\mathbf{u}(\mathbf{x},\Omega,\omega) - \mathbf{u}_{\mathrm{obs}}(\mathbf{x},\omega)|^2 \mathrm{d}S_{\mathrm{obs}}\mathrm{d}\omega, \tag{4.40}$$

where $\mathbf{u}_{\mathrm{obs}}$ is measured on the measurement surface $S_{\mathrm{obs}} \subseteq S_N$ of Ω_r. If the problem is well-posed, the true repartition of defects is recovered at the end of the minimization process.

4.3.2 Derivation of the topological gradient

Though it can be used in iterative procedures (see *e.g.* shape optimization in statics [104]), the topological gradient can also be used at the first iteration as an imaging function to obtain qualitative information on defects (here, their positions) [20, 21]. In the remainder, only the first iteration of the minimization process is hence considered. Therefore, the Lagrangian (4.6) is defined on the healthy medium Ω_0, without any *a priori* information on the repartition of the defects. The small change of topology (*i.e.* the variation $\delta\mathbf{m}$) is described by the inclusion of a small trial cavity $B_\epsilon(\mathbf{x})$ centred at $\mathbf{x}$ and of characteristic size $\epsilon \to 0^+$ [99]. The new domain is denoted by $\Omega = \Omega_0 \setminus B_\epsilon(\mathbf{x})$ where $\mathbf{x} \in \Omega_0$.

Let us write the variation

$$\mathbf{A}(\mathbf{m}+\delta\mathbf{m})\mathbf{u} - \mathbf{A}(\mathbf{m})\mathbf{u} = f(\epsilon)\delta\mathbf{A}\mathbf{u}, \quad f(\epsilon) > 0, \tag{4.41}$$

where $f(\epsilon)$ is a function of $B_\epsilon(\mathbf{x})$ which vanishes when $\epsilon \to 0^+$. The differentiation of the Lagrangian with respect to $\mathbf{m}$ is:

$$L(\mathbf{u},\boldsymbol{\lambda}_1,\boldsymbol{\lambda}_2,\boldsymbol{\lambda}_3,\mathbf{m}+\delta\mathbf{m}) - L(\mathbf{u},\boldsymbol{\lambda}_1,\boldsymbol{\lambda}_2,\boldsymbol{\lambda}_3,\mathbf{m}) = \mathrm{Re}\Big(\int_{\mathbb{R}^+}\int_{\Omega_0} f(\epsilon)\overline{\boldsymbol{\lambda}_1}\cdot(\delta\mathbf{A}\mathbf{u})\mathrm{d}\Omega_0\mathrm{d}\omega\Big), \tag{4.42}$$

$$= j(\Omega) - j(\Omega_0), \quad \forall \mathbf{x} \in \Omega_0. \tag{4.43}$$

The topological gradient is defined by [20, 21]:

$$g(\mathbf{x}) = \lim_{\epsilon\to 0^+} \frac{j(\Omega) - j(\Omega_0)}{f(\epsilon)}, \tag{4.44}$$

so that

$$g(\mathbf{x}) = \mathrm{Re}\Big(\int_{\mathbb{R}^+}\int_{\Omega_0} \overline{\boldsymbol{\lambda}_1}\cdot(\delta\mathbf{A}\mathbf{u})\mathrm{d}\Omega_0\mathrm{d}\omega\Big). \tag{4.45}$$

The asymptotic analysis of $\delta\mathbf{Au}$ when $\epsilon \to 0^+$ (*i.e.* the asymptotic analysis of the field scattered by an infinitely small cavity under the Born approximation) yields [21, 99]:

$$g(\mathbf{x}) = \mathrm{Re}\Big(\int_{\mathbb{R}+} \sigma(\mathbf{v}) : (\mathcal{A} : \sigma(\mathbf{u})) - \rho\omega^2 \mathbf{v}.\mathbf{u} \mathrm{d}\omega \Big), \forall \mathbf{x} \in \Omega_0, \tag{4.46}$$

where $\mathbf{u}$ is the forward field, $\mathbf{v}$ $(= \overline{\boldsymbol{\lambda}_1})$ is the adjoint field. $\mathcal{A}$ is the polarization tensor, which is specific of the defect. It depends on the shape of the chosen trial cavity, its orientation, and on the boundary conditions on its edges (here, Neumann boundary conditions have been assumed — see Eq. (4.39)). The polarization tensor can be obtained either analytically or numerically (see *e.g.* the summary of explicit formulations of the polarization tensor in Ref. [99]).

4.3.3 The topological gradient as an imaging function

The topological gradient $g(\mathbf{x})$ gives the sensitivity of the functional $j(\Omega)$ to the inclusion of a small cavity at a point $\mathbf{x}$ of the reference medium Ω_0. For this, the domain Ω_0 is modified by creating a hole $B_\epsilon(\mathbf{x})$ centred at $\mathbf{x}$ and of characteristic size ϵ. This process is global in nature since only two computations (of the forward and adjoint fields) are needed to obtain the gradient in the reference medium with Eq. (4.46), that is to insert fictitious holes and to obtain the sensitivity at all points of the sampled reference medium. Actually $g(\mathbf{x})$ is expected to take the most negative values at points corresponding to real holes, such that the value of the misfit functional $j(\Omega)$ decreases. The spatial representation of $g(\mathbf{x})$ can then reveal the defects embedded in the real medium. However, note that there is no mathematical proof that the gradient indeed gives the true location of the defects though work is in progress (see Ref. [114] in acoustics).

In Eq. (4.46), the integration can be restricted on the frequency range of the transducers and replaced with a discrete summation depending on the sampling frequency. The resultant image depends on the frequency spectrum [106, 115]: at low frequencies (with respect to the size of the defect), the maximum values of the gradient are concentrated inside the defect while they are concentrated at its edges at high frequencies.

Besides, various simplified formulations of the gradient have been proposed in the literature. Neglecting the stress fields contribution and dropping the $\rho\omega^2$ factor, one gets:

$$g_S(\mathbf{x}) = \mathrm{Re}\Big(\int_{\mathbb{R}+} \mathbf{u}(\mathbf{x}, \omega) \cdot \mathbf{v}(\mathbf{x}, \omega) \mathrm{d}\omega \Big), \forall \mathbf{x} \in \Omega_0. \tag{4.47}$$

However, the gradient g_S gives an image which contains spatial oscillations. The latter can be removed by considering the spatial envelope of the gradient, yielding the following formula [23]:

$$g_e(\mathbf{x}) = | \int_{\mathbb{R}+} \mathbf{u}(\mathbf{x}, \omega) \cdot \mathbf{v}(\mathbf{x}, \omega) \mathrm{d}\omega |, \forall \mathbf{x} \in \Omega_0. \tag{4.48}$$

It is also possible to use a deconvolution of the gradient by the direct field (Ref. [22]) such that:

$$g_{de}(\mathbf{x}) = | \int_{\mathbb{R}+} \frac{\mathbf{u}(\mathbf{x}, \omega)\mathbf{v}(\mathbf{x}, \omega)}{|\mathbf{u}(\mathbf{x}, \omega)|^2} \mathrm{d}\omega |, \forall \mathbf{x} \in \Omega_0. \tag{4.49}$$

The gradient g_{de} can increase the resolution of the image. However, the noise might also increase.

It is noteworthy that the polarisation tensor has been neglected in Eqs.(4.47)–(4.49). The equations are thus close to that determined for density identification (see Eq. (4.31)). It means that the simplified gradients given by (4.47)–(4.49) are no longer truly connected to the topology of the medium.

As a side remark, we mention that in the time-domain the so-called topological energy is based on similar simplifications. Time-domain gradient requires to store more data (at each time step) than in the frequency domain [23], which increases the cost of the method.

4.3.4 Implementation of the method for waveguide imaging

This section details the implementation of the topological imaging method in the case of waveguides. On one hand, it is necessary to solve a scattering problem to synthesize the displacement field $\mathbf{u}_{\text{obs}}$ measured in the damaged medium Ω_r. On the other hand, it is necessary to solve a forced response problem to obtain the forward and adjoint fields in the reference medium Ω_0. The reference medium Ω_0 is a healthy waveguide of section S and axis z, such that $\Omega_0 = S \times \mathbb{R}$. $\partial\Omega_0$ is the guiding surface of the waveguide.

First, let us introduce the model of the synthetic damaged medium Ω_r. The waveguide is damaged by a defect B_r of free boundary Γ_r, such that $\Omega_r = \Omega_0 \setminus B_r$. The excitation surface is denoted S_r. The following equations are hence satisfied:

$$\mathbf{A}(\mathbf{x},\omega)\mathbf{u}_{\text{synth}}(\mathbf{x},\omega) = \mathbf{0}, \quad \forall \mathbf{x} \in \Omega_r, \tag{4.50}$$

$$\sigma\left(\mathbf{u}_{\text{synth}}(\mathbf{x},\omega)\right) \cdot \mathbf{n} = \boldsymbol{\sigma}_N, \quad \forall \mathbf{x} \in S_r, \tag{4.51}$$

$$\sigma\left(\mathbf{u}_{\text{synth}}(\mathbf{x},\omega)\right) \cdot \mathbf{n} = \mathbf{0}, \quad \forall \mathbf{x} \in \Gamma_r. \tag{4.52}$$

Note that Dirichlet boundary conditions have been discarded for simplicity ($S_D = \varnothing$).

Second, the forward problem is given in the reference waveguide Ω_0 (without defect) by the equations:

$$\mathbf{A}(\mathbf{x},\Omega_0,\omega)\mathbf{u}(\mathbf{x},\Omega_0,\omega) = \mathbf{0}, \quad \forall \mathbf{x} \in \Omega_0, \tag{4.53}$$

$$\sigma\left(\mathbf{u}(\mathbf{x},\Omega_0,\omega)\right) \cdot \mathbf{n} = \mathbf{0}, \quad \forall \mathbf{x} \in \partial\Omega_0 \setminus S_0, \tag{4.54}$$

$$\sigma\left(\mathbf{u}(\mathbf{x},\Omega_0,\omega)\right) \cdot \mathbf{n} = \boldsymbol{\sigma}_N, \quad \forall \mathbf{x} \in S_0. \tag{4.55}$$

The excitation applied on the surfaces S_0 (forward problem) and S_r (synthetic problem) are the same in practice.

Third, the adjoint problem is given in the reference waveguide by:

$$\mathbf{A}(\mathbf{x},\Omega_0,\omega)\mathbf{v}(\mathbf{x},\Omega_0,\omega) = \mathbf{0}, \quad \forall \mathbf{x} \in \Omega_0, \tag{4.56}$$

$$\sigma\left(\mathbf{v}(\mathbf{x},\Omega_0,\omega)\right) \cdot \mathbf{n} = \mathbf{0}, \quad \forall \mathbf{x} \in \partial\Omega_0 \backslash S_{\text{obs}}, \tag{4.57}$$

$$\sigma\left(\mathbf{v}(\mathbf{x},\Omega_0,\omega)\right) \cdot \mathbf{n} = \overline{\mathbf{u}(\mathbf{x},\Omega_0,\omega) - \mathbf{u}_{\text{synth}}(\mathbf{x},\omega)}, \quad \forall \mathbf{x} \in S_{\text{obs}}. \tag{4.58}$$

The excitation is the conjugate residue, that is the conjugate of the difference between the solutions of Eqs. (4.53)–(4.55) and Eqs. (4.50)–(4.52) on $S_{\text{obs}} \subseteq \partial\Omega_0$.

As for numerical methods, the forward and the adjoint problems are solved by the method presented in Chap. 2 while the synthetic scattering problem is solved with the method of Chap. 3. In order to avoid the inverse crime [98], modes are actually computed with different FE meshes for the synthetic scattering problem on one hand, and for the forward and the adjoint problems on the other hand.

From Chap. 2, the discretized forward displacement is expanded on the modes as follows:

$$\mathbf{U}(z,\omega) = \sum_{m=1}^{M} \mathbf{E}_m(\omega)\hat{\mathbf{F}}_u(k_m(\omega))\mathrm{e}^{\mathrm{j}k_m(\omega)z}, \ z > z_S. \tag{4.59}$$

$\mathbf{U}(z,\omega)$ is the displacement at each point of an imaging sampling grid of Ω_0, defined by the FE discretization along the section of the waveguide and by an arbitrary (thin enough) discretization along the direction of propagation z ($z > z_S$, where z_S is the source position). Similarly, the discretized adjoint displacement is given by:

$$\mathbf{V}(z,\omega) = \sum_{m=1}^{M} \mathbf{E}_m(\omega)\hat{\mathbf{F}}_v(k_m(\omega))\mathrm{e}^{\mathrm{j}k_m(\omega)z}, \ z > z_S. \tag{4.60}$$

The same modal basis is used in Eqs. (4.59) and (4.60). Thanks to the modal formalism, modes are computed only once which then enables to obtain very quickly the forward and adjoint fields at any point of the imaging sampling grid.

In Eqs. (4.59) and (4.60), $\hat{\mathbf{F}}_u(k_m(\omega))$ and $\hat{\mathbf{F}}_v(k_m(\omega))$ are the sources of the forward and adjoint problems, expressed after discretization and a spatial Fourier transform as nodal forces on the cross-section of the waveguide. In Secs. 4.4 and 4.5, point sources will be applied at the surface of the waveguide. The exact expression of the nodal forces is given in that case in the following.

Assuming that the forward source is a point source oriented in the z direction, and concentrated at $z = z_S$, the source of the discretized forward problem can be written:

$$\mathbf{F}_u(z,\omega) = \mathbf{F}_u f(\omega)\delta(z - z_s), \tag{4.61}$$

where the vector of nodal forces $\mathbf{F}_u = [0 \dots 0 \ 1 \ 0 \dots 0]^{\mathrm{T}}$ is nonzero only at the dof in z direction of the node corresponding to the source position. $f(\omega)$ is the spectrum of the excitation. After a spatial Fourier transform, the source of the forward problem is finally given by:

$$\hat{\mathbf{F}}_u(k) = \mathbf{F}_u f(\omega)e^{\mathrm{j}kz_S}. \tag{4.62}$$

Besides, the observation surface $S_{\text{obs}} \subset \partial\Omega_0$ is restricted to a set of N point transducers at the surface of the waveguide. We recall that these transducers act both as receivers (for the measurement of residue), and as sources (for the adjoint problem). Therefore, the source of the discretized adjoint problem can be written:

$$\mathbf{F}_v(z,\omega) = \sum_{i=1}^{N} \mathbf{F}_{vi}(\omega)\delta(z - z_i), \tag{4.63}$$

where $z_i \leq z_S$ is the position of the i-th transducer along z. For the i-th transducer, let us define $f_{vix}(\omega)$ (resp. $f_{viy}(\omega)$, $f_{viz}(\omega)$) as the conjugate residue obtained from Eq. (4.58) measured in the x direction (resp. y, z) direction. The vector of nodal forces $\mathbf{F}_{vi}$ is not null at the dofs of the node corresponding to the transducer position, such that $\mathbf{F}_{vi}(\omega) = [0 \dots 0 \ f_{vix}(\omega) \ f_{viy}(\omega) \ f_{viz}(\omega) \ 0 \dots 0]^{\mathrm{T}}$. After a spatial Fourier transform, the source of the adjoint problem is finally given by:

$$\hat{\mathbf{F}}_v(k) = \sum_{i=1}^{N} \mathbf{F}_{vi}(\omega)e^{\mathrm{j}kz_i}. \tag{4.64}$$

Material	ρ (kg m^{-3})	c_l (m s^{-1})	c_s (m s^{-1})	η_l (Np wavelength^{-1})	η_s (Np wavelength^{-1})
Steel	7932	5960	3260	0.003	0.008
Cement grout	1600	2810	1700	0.043	0.1

Table 4.1 – Material properties

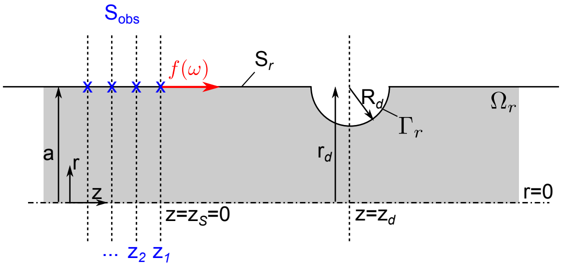

Figure 4.1 – Sketch of the synthetic scattering problem in the damaged closed waveguide Ω_r excited by a point source at $z = z_S$ (2D axisymmetric representation). Blue crosses: position of the transducers at the measurement surface S_{obs}.

Considering the synthetic displacement, it is not necessary to compute it at each point of the damaged waveguide. Indeed, the displacement $\mathbf{u}_{\text{synth}}$ is measured only on S_{obs}. A hybrid model of the defect and its vicinity is used (see Chap. 3). The input modal coefficients are determined from the modal decomposition of the source (similar to Eq. (4.59), but with a modal basis computed from a different FE mesh). The modal coefficients are then subsequently propagated and enforced to the input boundary of the hybrid model. The solution of the hybrid system gives the outgoing (diffracted) modal coefficients, which are then propagated to S_{obs} (at each $z = z_i$) to measure the diffracted field.

4.4 Application to closed waveguides

This section aims to evaluate the influence of the various formulations and parameters of the topological imaging approach. For simplicity, an axisymmetric circular closed waveguide is considered. The objective is to unequivocally locate one or several defects, along the axis of the waveguide, and in the section (*i.e.* along the radial direction).

Advantages and drawbacks of the different imaging functions recalled in Sec. 4.3.3 are discussed. Two configurations are considered: a monomodal but dispersive wave field, and a multimodal wave field. As an important issue from an experimental point of view, the required number of transducers for scattered field measurement is evaluated. In view of open waveguide imaging, a restricted configuration of measurement is chosen: due to the limited access to the structure, the data are measured in a backscattering configuration only (reflection), and at the guiding surface of the structure (rather than in the section).

4.4.1 Description of the test case

The healthy waveguide Ω_0 is a closed waveguide, with a circular section of radius $a = 10$ mm. For clarity, the guiding surface $\partial\Omega_0$ is now given by $r = a$. The waveguide is made of viscoelastic steel (see Tab. 4.1).

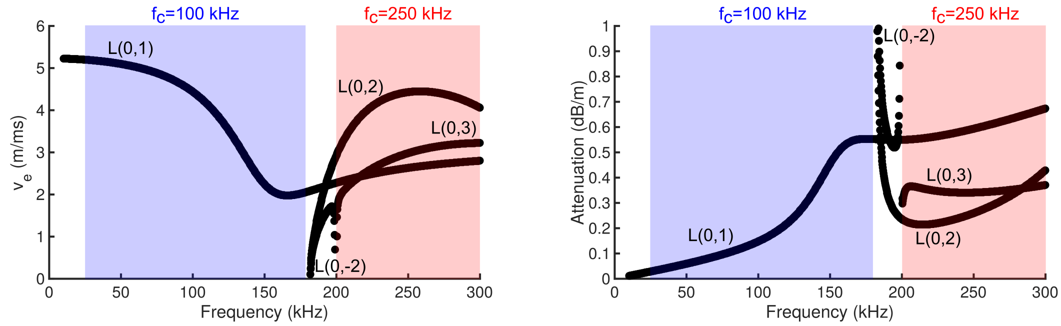

(a) (b)

Figure 4.2 – Dispersion curves for (a) the energy velocity and (b) the attenuation (viscoelastic steel axisymmetrical circular waveguide, radius $a = 10$ mm). Blue region: monomodal source. Red region: multimodal source.

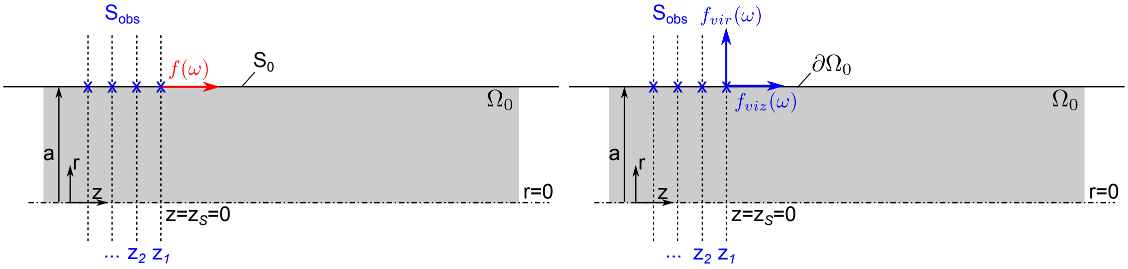

(a) (b)

Figure 4.3 – Sketch in the reference closed waveguide Ω_0 (2D axisymmetric representation) of: (a) the forward propagation problem; (b) the adjoint propagation problem. Blue crosses: position of the transducers at the surface S_{obs}.

In the damaged waveguide Ω_r, the defect is located at (r_d, z_d) in the (r, z) frame and has a radius R_d — see Fig. 4.1. The defect is assumed to be axisymmetric, and is therefore annular (no information on its angular localization in the waveguide is needed). Equations (4.50)–(4.52) written in cylindrical coordinates are satisfied. In the following, only axisymmetric wave fields are considered. Therefore, the solution $\mathbf{u}_{\text{synth}} = [u_{\text{synth},r}\ u_{\text{synth},z}]$ depends only on r and z. The source of the synthetic problem is an annular force applied at the surface of the waveguide on S_r (*i.e.* $r = a$), in z direction, and concentrated at $z_S = 0$. Hence only longitudinal modes propagate (see dispersion curves in Fig. 4.2).

The same source is considered in the forward problem (*i.e.* in the healthy waveguide), depicted in Fig. 4.3a. The forward problem satisfies Eqs. (4.53)–(4.55) written in cylindrical coordinates and accounting for axisymmetry.

Similarly, the adjoint problem (see Fig. 4.3b) satisfies Eqs. (4.56)–(4.58). For clarity, S_{obs} corresponds to a set of N annular transducers at the surface of the waveguide ($r = a$), where z_i gives the position of the i-th transducer along the axis z. In Eq. (4.63), the conjugate residue is now given by two components $f_{vir}(\omega)$ and $f_{viz}(\omega)$. Note that because the waveguide is infinite along z, the residue corresponds to the field diffracted by the defect.

Considering the numerical models, there is no PML because there is no embedding medium. The synthetic scattering problem is solved with a hybrid finite-element model (see

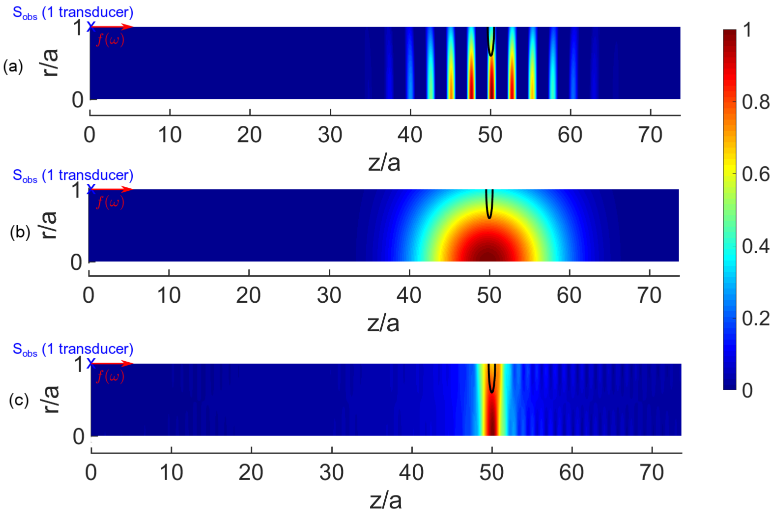

Figure 4.4 – Normalized image for a defect of radius $R_d = 0.4a$ and centered at point $(a, 50a)$ in a closed waveguide. The wavefield is monomodal. The residue is measured with a single transducer. Image obtained with an integration between 20 kHz and 180 kHz (f_c = 100 kHz, 640 frequencies), applying: (a) Eq. (4.47); (b) Eq. (4.48); (c) Eq. (4.49). The true location of the defect is identified by the black curve.

Chap. 3) involving roughly 800 dofs (six-nodes triangular elements), with $N = 15$ modes on the cross-section boundaries (for 40 dofs). The forward and adjoint fields are obtained at any point of the imaging sampling grid of Ω_0 applying Eqs. (4.59)–(4.64), with $M = 15$ modes (for 30 dofs on the cross-section). The axial spacing of the imaging grid is set to $0.05a$. The radial spacing corresponds to the size of finite elements, here $0.07a$.

4.4.2 Results

4.4.2.1 Preliminary results: monomodal imaging

To obtain a monomodal wave field, the source is a sinus of centre frequency $f_c = 100$ kHz modulated by a 10 cycle Hanning window. The solution is computed between 20 kHz and 180 kHz with 640 frequency steps. In that case, only the L(0,1) fundamental guided mode propagates. In this frequency range, the mode is strongly dispersive (see the blue region in Fig. 4.2). It is noteworthy that the sampling frequency and the frequency range are chosen according to the Nyquist-Shannon's theorem to avoid aliasing in the image.

In this section, the defect is centred at the surface of the waveguide ($r_d = a$), at a distance $z_d/a = 50$ to the source, and its radius is $R_d = 0.4a$. The defect is represented on each image with a black curve. The images obtained with various imaging functions are displayed in Fig. 4.4. In each case, the image is normalized by dividing the value of the imaging function at each point by the amplitude of its global maximum.

The distance of the defect to the source is well identified along the z axis, as shown by the location of points of greatest amplitude in Fig. 4.4. It confirms that dispersion does not affect the image, provided that it is correctly known as an *a priori* data for the forward and adjoint problems [22].

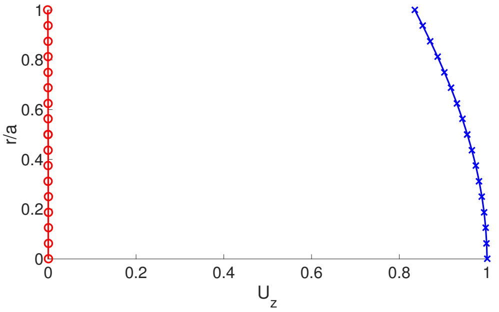

Figure 4.5 – Normalized longitudinal mode shape $\mathbf{U}_z$ of the L(0,1) mode in a viscoelastic steel waveguide of radius $a = 10$ mm at centre frequency $f_c = 100$ kHz. Blue crossed line: $\text{Re}(\mathbf{U}_z)$. Red circled line: $\text{Im}(\mathbf{U}_z)$.

However, the defect is not correctly located along the radial direction of the waveguide. This is not surprising because the image is the product of two monomodal wave fields in the healthy waveguide (see Eqs. (4.47)–(4.49)). When the wave fields are in phase (*i.e.* at the defect position), the image is then by construction the product of the mode shape by itself. Here in Fig. 4.4, the spots are centred at the centre of the waveguide rather than at the surface, which is consistent with the longitudinal mode shape of the L(0,1) mode, displayed at $f_c = 100$ kHz in Fig. 4.5 (the radial displacement is much lower in that case and is not shown).

We point out that only one transducer is necessary to obtain images in Fig. 4.4. Numerical tests have shown that increasing the number of transducers does not improve the image.

Now let us discuss the influence on the image of the imaging function. The image displayed in Fig. 4.4a (gradient Eq. (4.47)) contains several oscillations of decreasing amplitude on both sides of the spot centered on the defect. Oscillations can lead to a misinterpretation of the results since each of them can be seen as additional defects embedded into the waveguide. On the contrary, the use of Eq. (4.48) enables to obtain a single spot, although larger (Fig. 4.4b). As expected from the results of Ref. [23], this spot corresponds to the spatial envelope of oscillations observed in Fig. 4.4a. Another possibility is to use Eq. (4.49), which indeed increases the resolution of the image (see Ref. [22]), as shown by the smaller width of the spot in Fig. 4.4c compared to Fig. 4.4b. However, the noise increases because the deconvolution by the forward field gives the same weight to the integrand of Eq. (4.49) at each frequency. Frequency components which are not or little insonified are then artificially enhanced although they contain only poor information.

4.4.2.2 Multimodal imaging

Let us now consider a multimodal propagation. The source is a sinus of centre frequency $f_c = 250$ kHz modulated by a 20 cycle Hanning window. The solution is computed between 200 kHz and 300 kHz with 400 frequency steps (the cut-off frequency of the modes is avoided). Three modes (L(0,1), L(0,2) and L(0,3)) propagate with different velocities and attenuations (see red region in Fig. 4.2).

In this section, we consider the same defect as in the monomodal case. The image obtained with the imaging function (4.48) is displayed in Fig. 4.6a (only one transducer has been used to measure the diffracted field). Several spots of great amplitude prevent the

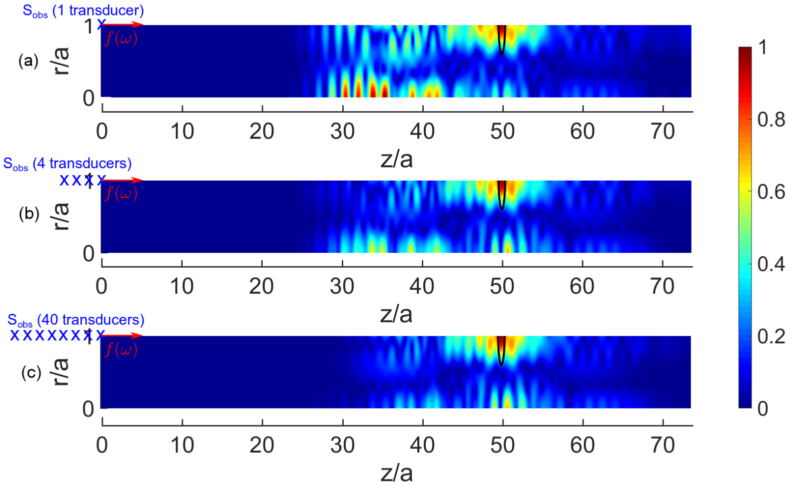

Figure 4.6 – Normalized image for a defect of radius $R_d = 0.4a$ centered at point $(a, 50a)$ in a closed waveguide. The wave field is multimodal. Imaging function: Eq. (4.48) integrated between 200 kHz and 300 kHz (f_c = 250 kHz, 400 frequencies). Surface S_{obs}: (a) 1 transducer at $z_1 = 0$; (b) 4 transducers with a spacing of 0.46a ($z_i \in [-1.84a,\ 0]$, $i = 1 \ldots 4$); (c) 40 transducers with a spacing of 0.46a ($z_i \in [-18.4a,\ 0]$, $i = 1 \ldots 40$). The true location of the defect is identified by the black curve.

unambiguous localization of the defect. Most of these spots are artefacts. Their origin is discussed later in Sec. 4.4.2.3.

When the number of transducers increases, the quality of the image improves (the spacing of the transducer is an important parameter as well, also discussed later in Sec. 4.4.2.3). This is shown in Figs. 4.6b and 4.6c, where 4 and 40 transducers have been respectively used. The amplitude of the artefacts decreases. One spot of great amplitude remains, giving the correct axial distance between the source and the defect, and also its correct location in the radial direction. It is noteworthy that there is only a slight difference between Figs. 4.6b and 4.6c, so that 4 transducers appear to be sufficient to obtain an acceptable image in this case. This is promising from an experimental point of view.

In practice owing to transducers specifications, the measurement of the diffracted field can be limited to only one component of the displacement field. Figure 4.7a displays the image obtained with one transducer when only the radial component is measured (in Eq. (4.63), $f_{vir} \neq 0$, $f_{viz} = 0$). Figure 4.7b displays the image when only the axial component is measured (in Eq. (4.63), $f_{vir} = 0$, $f_{viz} \neq 0$). In the former case (Fig. 4.7a), it can be observed that the defect is no longer accurately located. Measuring only one component of the displacement field can then lead to a significant degradation of the image. In the latter case (Fig. 4.7b), the image is close to that in Fig. 4.6a, although of slightly lower quality.

The resolution of the image decreases when the distance between the defect and the transducer increases. As observed in Fig. 4.8b (defect at $z_d/a = 250$) a spreading of the spot identifying the defect can be observed compared to Fig. 4.6a (defect at $z_d/a = 50$). It has been checked that this effect is strongly reduced with a purely elastic material. The spreading of the spot can then be related to the attenuation of the waves. Actually, in Ref. [20], the authors have assumed that topological imaging may work in viscoelastic media, but with a spreading of energy around the focusing point. Our results then confirm

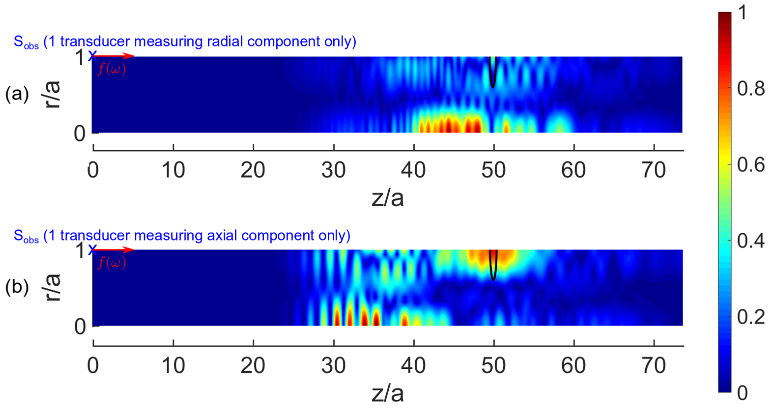

Figure 4.7 – Normalized image for a defect of radius $R_d = 0.4a$ centered at point $(a, 50a)$ in a closed waveguide. The wave field is multimodal. Imaging function: Eq. (4.48) integrated between 200 kHz and 300 kHz ($f_c = 250$ kHz, 400 frequencies). Surface S_{obs}: (a) 1 transducer at $z_1 = 0$ measuring radial component only; (b) 1 transducer at $z_1 = 0$ measuring axial component only.

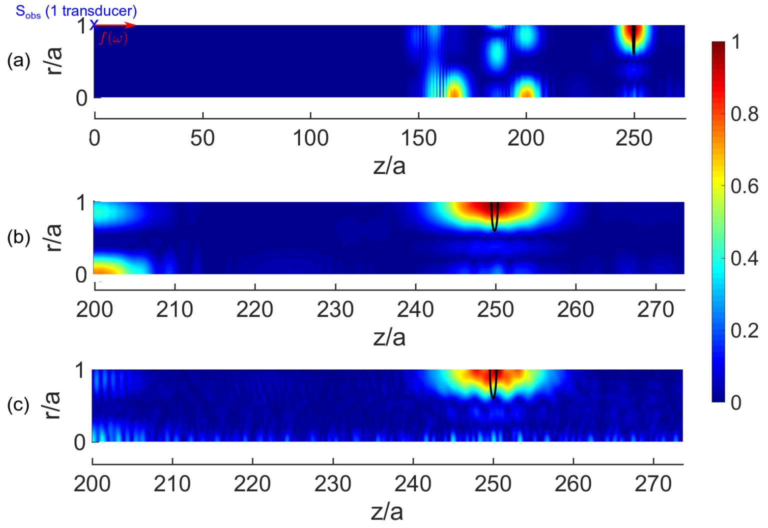

Figure 4.8 – Normalized image for a defect of radius $R_d = 0.4a$ centered at point $(a, 250a)$ in a closed waveguide. The wave field is multimodal. Imaging function: Eq. (4.48) integrated between 200 kHz and 300 kHz ($f_c = 250$ kHz, 400 frequencies). Surface S_{obs}: 1 transducer at $z_1 = 0$. (a) Image obtained; (b) Same as (a) but with a zoom between $z/a = 200$ and $z/a = 270$; (c) Image obtained between $z/a = 200$ and $z/a = 270$ removing the attenuation of modes L(0,1), L(0,2) and L(0,3) in the forward and the adjoint problems. The true location of the defect is identified by the black curve.

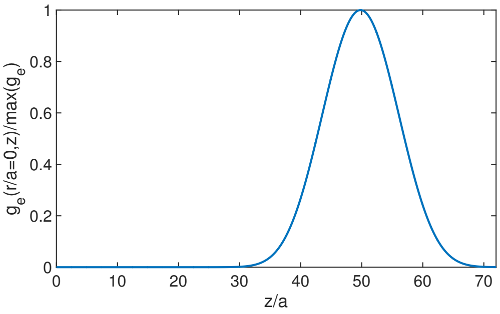

(a)

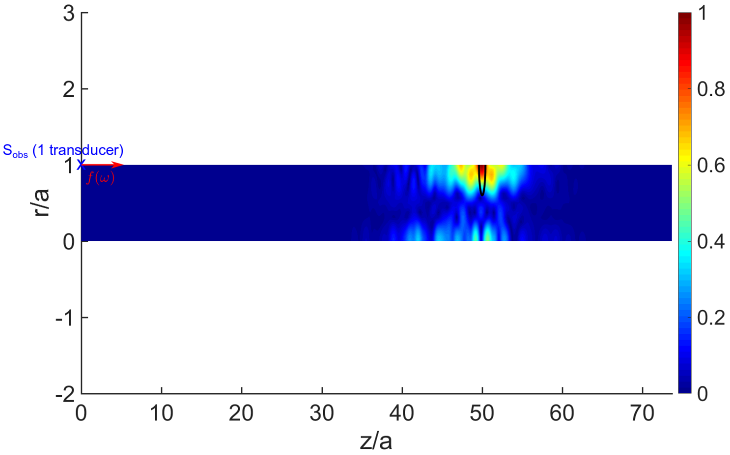

(b)

Figure 4.9 – Post-processing of the artefacts. (a) Post-processing profile: normalized value of $g_e(r = 0, z/a)$ extracted from the monomodal image in Fig. 4.4b; (b) Post-processed image in the multimodal test case: multiplication of Fig. 4.6a by the post-processing profile.

their assumption.

The modal formalism used to compute the forward and adjoint field offers a convenient way to artificially remove the attenuation when constructing the image. In Eqs. (4.59) and (4.60), the modal wavenumber is complex-valued. The real part of the wavenumber is related to the travelling velocity of the mode while its imaginary part is related to the attenuation of the mode. Retaining only the real part of the modal wavenumber in Eqs. (4.59) and (4.60) then enables to compute the forward and adjoint fields without any attenuation. Let us point out that it is not equivalent to consider a lossless reference medium because the travelling modal velocities are those of modes in a lossy medium. Furthermore, the proposed correction does not enable to compensate the losses in the real medium. Thereby, the measurement still suffers from viscoelasticity in the synthetic problem. The image after attenuation removal is displayed in Fig. 4.8c. The attenuation has been removed for propagating modes only (here the L(0,1), L(0,2) and L(0,3) modes). A slight narrowing of the spot can be observed compared to Fig. 4.8b. The effect of attenuation and its removal will be illustrated more clearly in the open waveguide test case (Sec. 4.5), where radiation losses can occur.

Note that in Fig. 4.8a the artefacts still occur but at greater distances to the defect position than in Fig. 4.6a (see at $z_d/a = 160$ or $z_d/a = 200$ in Fig. 4.8a). Conversely others numerical tests have shown that for a smaller distance between the defect and the transducer, the artefacts get closer to the spot. With several transducers at various distances to the defect, the artefacts will then occur at different positions in the image. But, the contribution of each transducer will also superpose at the defect position, thus increasing the amplitude of this spot compared with those of the artefacts. This is further explained in Sec. 4.4.2.3.

Finally, let us propose a simple post-processing method to remove most of the artefacts from a multimodal image. The idea is to multiply the monomodal image, which gives the correct position of the defect along the z axis (see Sec. 4.4.2.1), and the multimodal image. More precisely, the value of the monomodal imaging function is extracted along z for a given value of r. It enables to post-process the multimodal image in the axis direction only. As an example, Figure 4.9a displays the value of $g_e(z)$ at the centre of the waveguide ($r = 0$), obtained from Fig. 4.4b. This defines a monodimensional post-processing profile. The latter is then applied to the multimodal image, in Fig. 4.6a. As a result, Fig. 4.9b shows that most of the artefacts have been removed from the image, thus allowing the identification of the defect.

4.4.2.3 Origin of the artefacts in the multimodal configuration

This section aims to explain the origin of the artefacts observed in the image with a multimodal configuration (see *e.g.* Fig. 4.6a). To do so, it is convenient to study the construction of the image in the time domain. The various gradients proposed in Sec. 4.3.3 can be reduced in essence to the product $\int_{\mathbb{R}} \mathbf{u}(\mathbf{x},\omega)\cdot\mathbf{v}(\mathbf{x},\omega)\mathrm{d}\omega$, where $\mathbf{v}(\mathbf{x},\omega) = \overline{\boldsymbol{\lambda}}_1(\mathbf{x},\omega)$ satisfies Eqs. (4.14)–(4.17) in the reference waveguide. In the time-domain, $\overline{\boldsymbol{\lambda}}_1(\mathbf{x},t) = \mathbf{v}(\mathbf{x},T-t)$ (the adjoint problem is read backwards in time — see Sec. 4.2.6). Thereby, applying Plancherel theorem yields:

$$\int_{\mathbb{R}} \mathbf{u}(\mathbf{x},\omega)\cdot\overline{\boldsymbol{\lambda}}_1(\mathbf{x},\omega)\mathrm{d}\omega = \int_0^T \mathbf{u}(\mathbf{x},t)\cdot\overline{\boldsymbol{\lambda}}_1(\mathbf{x},t)\mathrm{d}t, \tag{4.65}$$

$$= \int_0^T \mathbf{u}(\mathbf{x},t)\cdot\mathbf{v}(\mathbf{x},T-t)\mathrm{d}t, \tag{4.66}$$

where T is the duration of the signal. In the following, we then study the value of Eq. (4.66) at various positions $\mathbf{x}$. For sake of clarity, the analysis is restricted to a monodimensional case ($\mathbf{x} = z$), with only two modes propagating. Besides, both the source (in the forward and synthetic problems) and the transducer (in the adjoint problem) are located at the same point, at $z = z_S = z_1$.

First, let us detail the construction of the source of the adjoint problem. In the forward and synthetic transient problems, the source signal (displayed in Fig. 4.10a) is emitted and measured at $z = z_S$. In the synthetic medium, two wave packets labelled 1 and 2 reach the defect at $t = t_1$ and $t = t_2$ — see Fig. 4.10c. Both modes are reflected and also converted by the defect. The converted modes are labelled 12 and 21, where the first number gives the incident mode and the last number gives the reflected mode, and coloured in green (see Fig. 4.10d). The residue is the difference of signals (b) and (d), and corresponds then to the diffracted field. The time-reversed residue yields the source signal of the adjoint problem, shown in Fig. 4.10e.

In the adjoint problem, the source signal (Fig. 4.10e) contains three packets. Each of them naturally generates the two propagating modes, that reach an arbitrary position

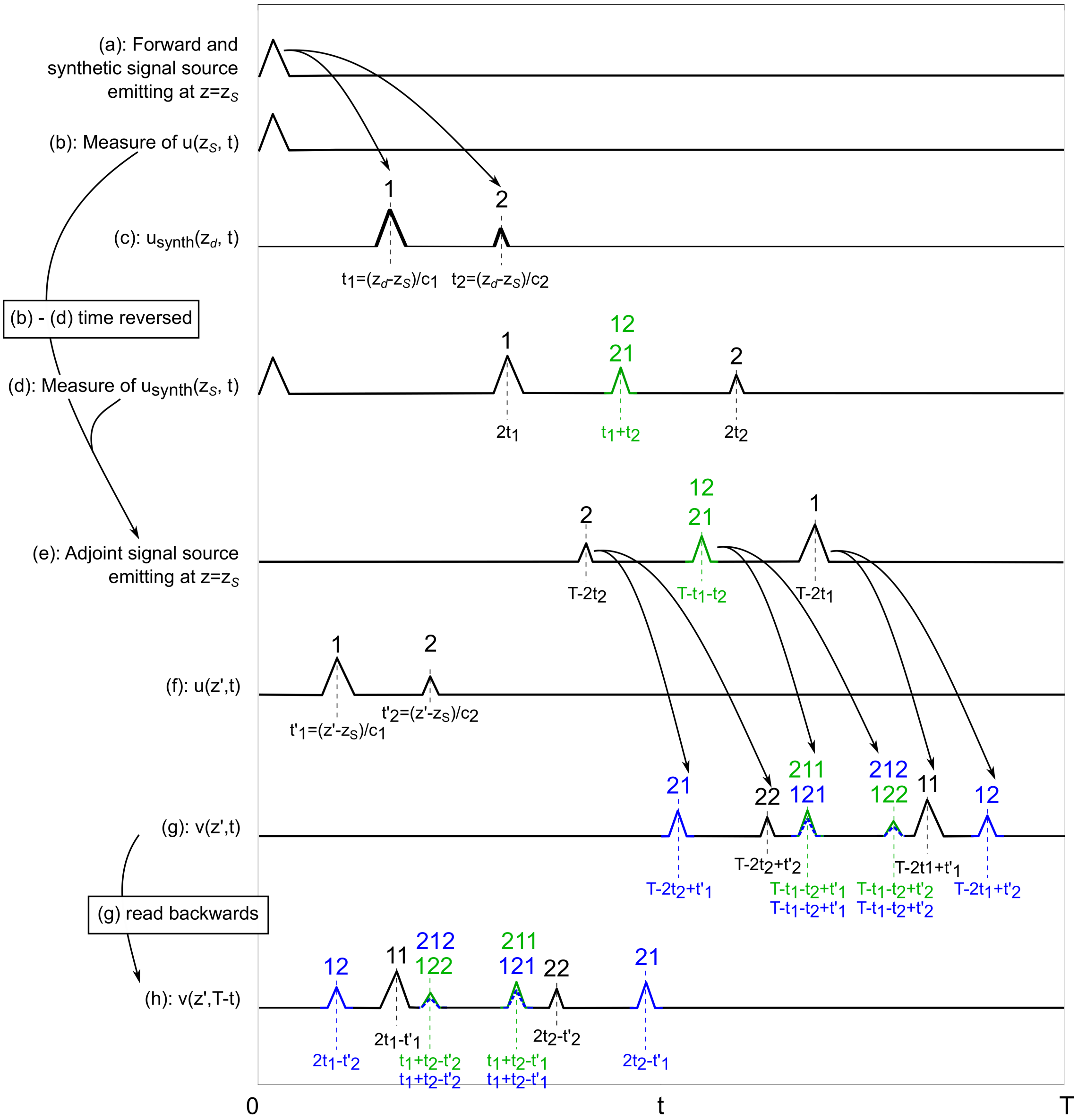

Figure 4.10 – Signals in a 1D medium in which two modes propagate, with source and transducer at the same position $z = z_S = z_1$. (a) Source signal emitted at $z = z_S$ in the forward and synthetic problems; (b) Measured forward signal $u(z_S, t)$ in the reference medium; (c) Synthetic signal $u_{\text{synth}}(z_d, t)$ at the defect position; (d) Measured synthetic signal $u_{\text{synth}}(z_S, t)$ in the damaged medium; (e) Source signal emitted at $z = z_S$ in the adjoint problem; (f) Forward signal $u(z', t)$ at an arbitrary position $z' > z_S$ in the reference medium; (g) Adjoint signal $v(z', t)$ in the reference medium; (h) Adjoint signal $v(z, T - t)$ read backwards in time in the reference medium. Colours and labels are explained in the text.

$z' > z_S$ after time-of-flight t'_1 and t'_2 respectively. The adjoint signal $v(z', t)$ in Fig. 4.10g contains hence eight wave packets. It must be read backwards in time to obtain $v(z', T-t)$ (Fig. 4.10h), further multiplied with the forward signal $u(z', t)$ at the same position (see Fig. 4.10f), as calculated by Eq. (4.66). In Fig. 4.10h, the signal $v(z', T-t)$ then travels from the right to the left as z' increases.

In the adjoint signals, the modes are labelled with the following convention: the last number identifies the mode (1 or 2) which is generated by the source packet indicated by the first numbers (that is, 1, 2, 12 or 21). Two cases have to be distinguished. If the generated mode (Fig. 4.10g) is the same as the source wave packet (Fig. 4.10e), the mode is consistently coloured in black or in green. Otherwise, if the generated mode is different from the source wave packet, the mode is coloured in blue. That is, "blue packets" originate from modal conversions by the adjoint source.

Figure 4.10 shows that the product in Eq. (4.66) is in general equal to zero, except at some positions z' associated to specific values of t'_1 and t'_2.

Focusing on the defect. Let us consider the case when $t'_1 = t_1$ and $t'_2 = t_2$ (Fig. 4.11). In this specific case, z' corresponds to the defect location z_d. It can be observed that both packets 1 and 2 of the forward signal (Fig. 4.11a) match in particular with "black packets" 11 and 22 of the adjoint signal (Fig. 4.11b). Thereby, Eq. (4.66) takes a significant value at z_d, which explains how topological imaging enables defect localization.

Artefacts due to modal conversion by the adjoint source. When $t'_2 = t_1$ (see Fig. 4.12),

$$z' = \frac{c_2}{c_1}(z_d - z_S) + z_S = z_b, \tag{4.67}$$

where $z_b < z_d$. The packet 2 in the forward signal (Fig. 4.12a) matches with the "blue packet" 12 in the adjoint signal (Fig. 4.12b). Therefore, Eq. (4.66) is not null, which subsequently creates an artefact at z_b. Actually, artefacts are created whenever a packet of the forward signal matches with a "blue packet" of the adjoint signal (*e.g.* at $t'_1 = t_2$ between packets 1 and 21 or at $t'_2 = (t_1 + t_2)/2$ between packets 2 and 212 (see Fig. 4.13), and so on). This shows that artefacts can appear because of modal conversion by the adjoint source. Indeed to avoid these artefacts, it is necessary to generate only "black" and "green" modes in the adjoint signal. Such a pure modal generation is difficult to achieve in practice. The modal selectivity can be improved by acting on the measurement configuration, that is on the choice of the observation surface S_{obs}. In this example, S_{obs} corresponds to a single point of measurement, which is the worst configuration.

Artefacts due to modal conversion by the defect. When $t'_2 = (t_1 + t_2)/2$ (see Fig. 4.13),

$$z' = \frac{c_2 + c_1}{2c_1}(z_d - z_S) + z_S = z_c, \tag{4.68}$$

where $z_c < z_d, z_c \neq z_b$. The packet 2 in the forward signal (Fig. 4.13a) matches with the "green packet" 122 in the adjoint signal (Fig. 4.13b). Hence, Eq. (4.66) is not null and another artefact is created at z_c. Artefacts are also created at other positions every time a packet of the forward signal matches with a "green packet" in the adjoint signal. For instance, it is also the case at $t'_1 = (t_1 + t_2)/2$ between packets 1 and 211. This shows

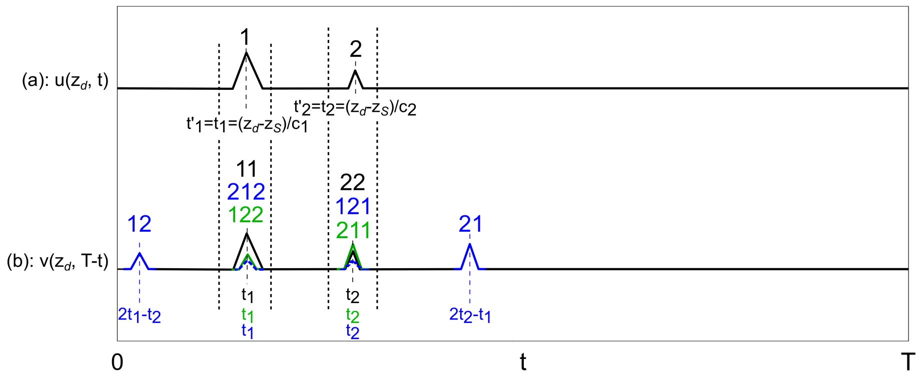

Figure 4.11 – $z = z_d$: signals focusing at the defect position. (a) Forward signal $u(z_d, t)$; (b) Adjoint signal $v(z_d, T - t)$. Dashed lines: matching parts of the signals such as the product $u(z_d, t)v(z_d, T - t)$ is not null. Colours and labels are explained in the text.

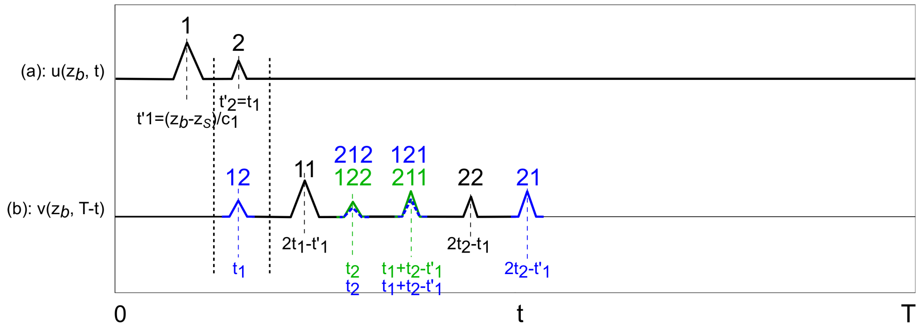

Figure 4.12 – $z' = z_b$: signals creating an artefact due to modal conversion by the adjoint source. (a) Forward signal $u(z_b, t)$; (b) Adjoint signal $v(z_b, T - t)$. Dashed lines: matching parts of the signals such as the product $u(z_b, t)v(z_b, T - t)$ is not null. Colours and labels are explained in the text.

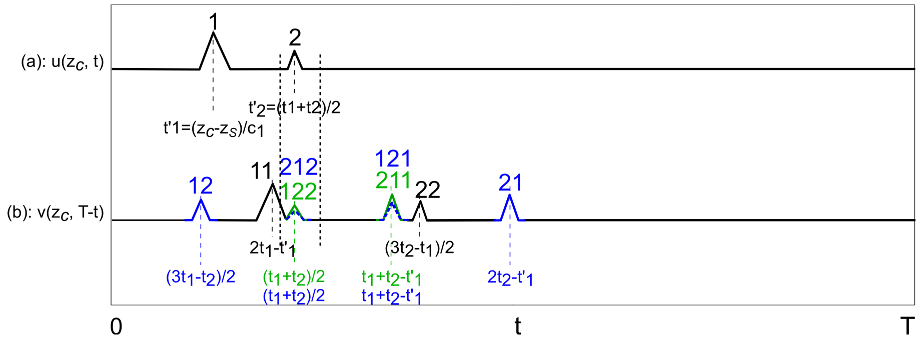

Figure 4.13 – $z' = z_c$: signals creating an artefact due to modal conversion by the defect. (a) Forward signal $u(z_c, t)$; (b) Adjoint signal $v(z_c, T - t)$. Dashed lines: matching parts of the signals such as the product $u(z_c, t)v(z_c, T - t)$ is not null. Colours and labels are explained in the text.

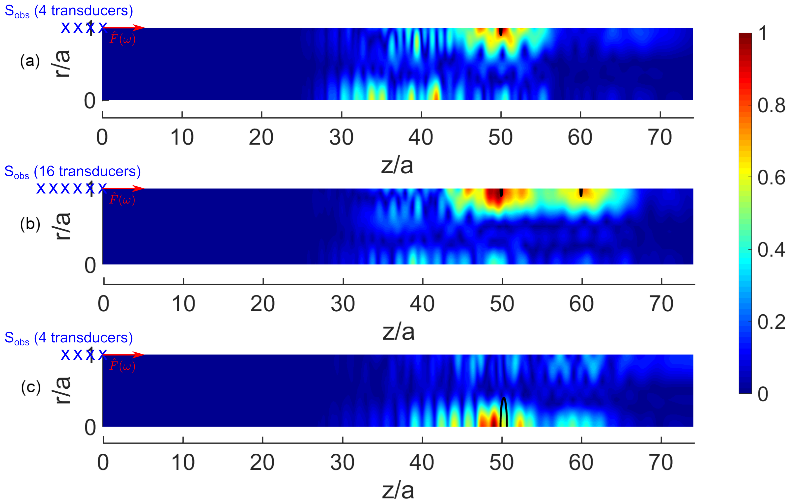

Figure 4.14 – Normalized image for a multimodal wave field. Imaging function: Eq. (4.48) integrated between 200 kHz and 300 kHz ($f_c = 250$ kHz, 400 frequencies). Type of defects: (a) one defect of radius $R_d = 0.1a$ centered at point $(a, 50a)$ (measurement surface: 4 transducers with a spacing of 0.46a); (b) two defects of radius $R_d = 0.1a$ centered at points $(a, 50a)$ and $(a, 60a)$ (measurement surface : 16 transducers with a spacing of 0.46a); (c) a defect of radius $R_d = 0.1a$ centered at point $(0, 50a)$ (measurement surface : 4 transducers with a spacing of 0.46a). The true location of the defect(s) is identified by the black curve.

that artefacts can appear because of modal conversion by the defect. Modal conversion is intrinsic to the defect. Thereby, this type of artefacts cannot be avoided.

One can notice in Eqs. (4.67) and (4.68), that the positions of the artefacts z_b and z_c depend on the distance $(z_d - z_S)$ between the defect and the adjoint source (we recall that $z_S = z_1$ in this example). This has also been observed in Fig. 4.8a. On the contrary, the correct focusing at the defect position, described by Fig. 4.11, does not depend on the distance between the defect and the adjoint source. Thereby, using several transducers at different positions enables to superpose several contributions at the defect location, while spreading the artefacts at different positions. It then favourably increases the amplitude of the image at the defect location in comparison to the amplitude of the artefacts. This is confirmed by Figs. 4.6b and 4.6c: the artefacts are not cancelled but their amplitude is strongly reduced.

Similarities between topological imaging and time-reversal procedures clearly appear in this section. The phenomenon of artefacts is actually analogous to the additional wavefronts observed during time-reversal of P and SV waves in an elastic media (see Ref. [116]), and also to sidelobes created by time-reversal of Lamb waves [117].

4.4.2.4 Influence of defect parameters in the multimodal configuration

Let us now reduce the radius of the defect to $R_d = 0.1a$ — see Fig. 4.14a. A comparison with Fig. 4.6b ($R_d = 0.4a$) shows that the defect remains rather accurately identified.

Then, Fig. 4.14b shows that two successive small defects can be also roughly located, provided that the first one is not too reflective. Here the number of transducers (16) has

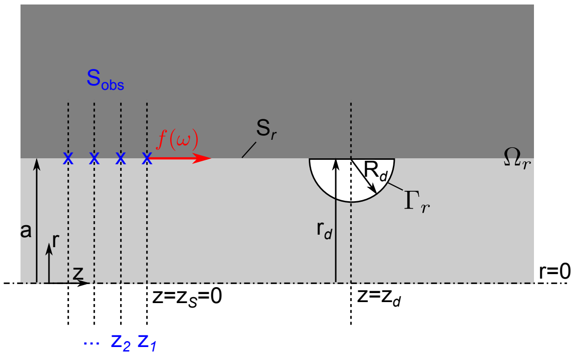

Figure 4.15 – Sketch of the synthetic scattering problem in the damaged open waveguide Ω_r excited by a point source at $z = z_S$, $r = a$ (2D axisymmetric representation). Blue crosses: position of the transducers at the measurement surface S_{obs}.

been increased to reduce the amplitude of artefacts generated by the second defect onto the spot identifying the first defect. Although not shown for conciseness, our numerical tests have shown that if the two defects are replaced with an elongated one covering the same length, only the beginning of the defect is visible, which is not surprising with a backscattering measurement configuration.

Finally, internal defects can also be located, as observed in Figure 4.14c. Although the localization of the defect appears to be less accurate along the z axis in this example, this result confirms that a multimodal configuration helps to locate a defect in the cross-section of the waveguide.

4.5 An open waveguide example

This section briefly gives an example of topological imaging applied to open waveguides, with a defect included into the core of the waveguide. The influence of leakage attenuation on the image is outlined.

4.5.1 Description of the test case

The damaged waveguide Ω_r is an axisymmetrical circular closed waveguide, of radius $a = 10$ mm and made of viscoelastic steel, embedded into cement grout (materials properties are given in Tab. 4.1). The core of the damaged waveguide Ω_r contains an axisymmetric defect of radius $R_d = 0.4a$, centred at point $(a, 50a)$ — see Fig. 4.15. The point source is located at the interface S_r between the core and the surrounding medium ($r = a$). The synthetic displacement field is measured in backscattering at the interface — see S_{obs} in Fig. 4.15.

As for forward and adjoints fields, the reference domain Ω_0 is an undamaged open waveguide. The forward field (see Fig. 4.16a) satisfies Eqs. (4.53) and (4.55) and the adjoint field (see Fig. 4.16b) satisfies Eqs. (4.56) and (4.58).

The synthetic scattering problem is solved with a PML hybrid model (Chap. 3), involving about 4500 dofs (six-nodes triangle elements), with $M = 15$ modes on each transparent boundaries for 82 dofs. The PML parameters are: $d = 0.1a$, $h = 2a$, $\hat{\gamma} = 2 + 4\mathrm{j}$. The

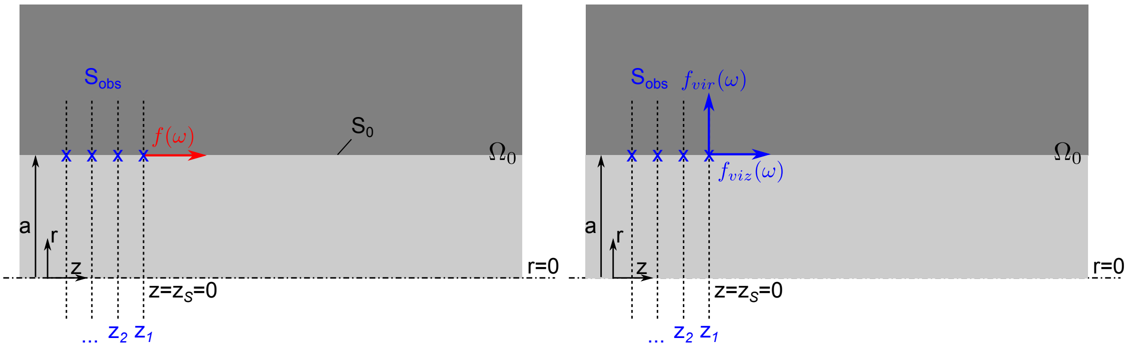

(a) (b)

Figure 4.16 – Sketch in the reference open waveguide Ω_0 (2D axisymmetric representation) of: (a) the forward propagation problem; (b) the adjoint propagation problem. Blue crosses: position of the transducers at the surface S_{obs}.

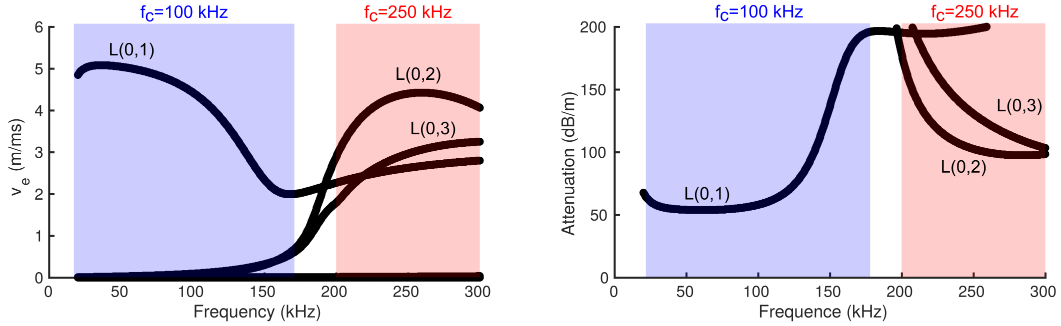

(a) (b)

Figure 4.17 – Dispersion curves for (a) the energy velocity and (b) the attenuation (circular waveguide in viscoelastic steel embedded into viscoelastic cement grout, radius $a = 10$ mm). Blue region: monomodal source. Red region: multimodal source.

forward and adjoint fields are obtained at any point of the imaging sampling grid of Ω_0 applying Eqs. (4.59)–(4.64), with $N = 50$ modes (for 94 dofs on the cross-section). The number of required modes in the modal expansions is higher for the forward and adjoint problems because the solutions must be accurate at any point of the medium, including the near-field of the source. On the contrary, in the synthetic problem, only the diffracted far-field is of interest, which allows reducing the number of modes. The axial spacing of the imaging grid is set to $0.05a$. The radial spacing corresponds to the size of finite elements, here $0.07a$.

4.5.2 Results

First, a monomodal wave field is emitted in the waveguide (the parameters are the same as in Sec. 4.4.2.1). In that case, only the L(0,1) leaky mode propagates (see the blue region in Fig. 4.17). Note that the attenuation of the mode due to leakage losses (Fig. 4.17b) is much stronger than that of the L(0,1) guided mode in a viscoelastic closed waveguide (Fig. 4.2b, the attenuation is roughly 500 times lower).

The image obtained applying Eq. (4.48) is displayed in Fig. 4.18a. A single spot, shifted

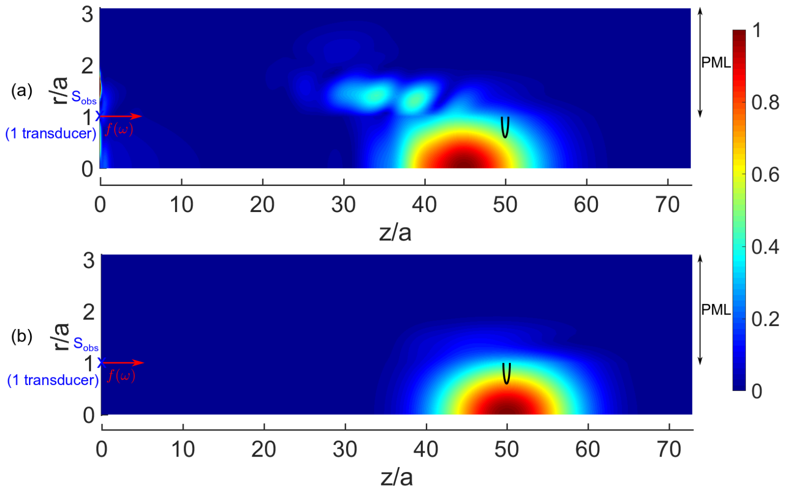

Figure 4.18 – Normalized image for a defect of radius $R_d = 0.4a$ centered at point $(a, 50a)$ and a monomodal wave field. Imaging function: Eq. (4.48) integrated between 20 kHz and 180 kHz (f_c = 100 kHz, 640 frequencies). Measurement surface S_{obs}: 1 transducer at $z_1 = 0$. Image obtained: (a) including the attenuation of the L(0,1) leaky mode in the forward and adjoint problems; (b) removing the attenuation of the L(0,1) leaky mode in the forward and adjoint problems. The true location of the defect is identified by the black curve.

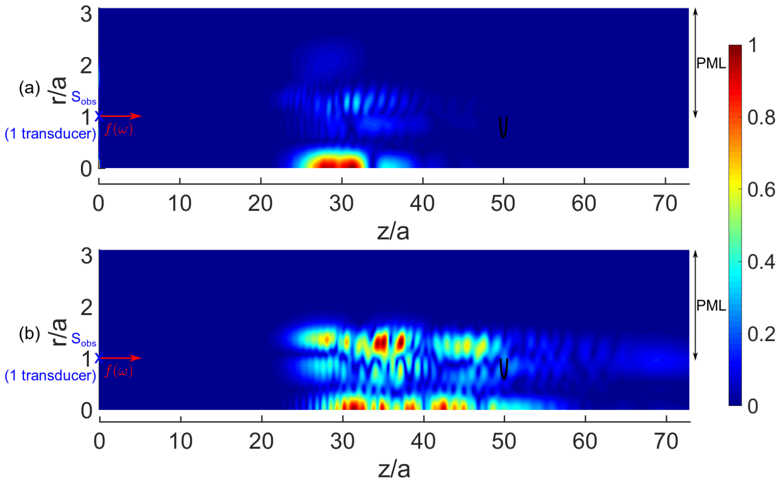

Figure 4.19 – Normalized image for a defect of radius $R_d = 0.4a$ centered at point $(a, 50a)$ and a monomodal wave field. Imaging function: Eq. (4.48) integrated between 200 kHz and 300 kHz (f_c = 250 kHz, 400 frequencies). Measurement surface S_{obs}: 1 transducer at $z_1 = 0$. Image obtained: (a) including the attenuation of the L(0,1), L(0,2) and L(0,3) leaky modes in the forward and adjoint problems; (b) removing the attenuation of the L(0,1), L(0,2) and L(0,3) leaky modes in the forward and adjoint problems. The true location of the defect is identified by the black curve.

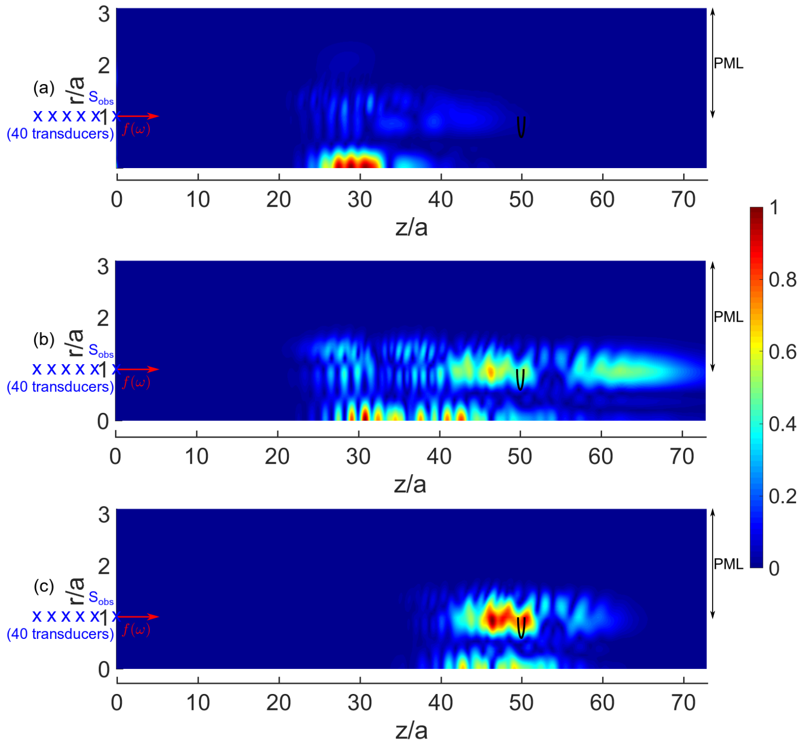

Figure 4.20 – Normalized image for a defect of radius $R_d = 0.4a$ centered at point $(a, 50a)$ and a monomodal wave field. Imaging function: Eq. (4.48) integrated between 200 kHz and 300 kHz (f_c = 250 kHz, 400 frequencies). Measurement surface S_{obs}: 40 transducers with a spacing of 0.46a ($z_i \in [-18.4a,\ 0]$, $i = 1 \dots 40$). Image obtained: (a) including the attenuation of the L(0,1), L(0,2) and L(0,3) leaky modes in the forward and adjoint problems; (b) removing the attenuation of the L(0,1), L(0,2) and L(0,3) leaky modes in the forward and adjoint problems; (c) same as (b) with post-processing from the monomodal image Fig. 4.18b (see Sec. 4.4.2.2). The true location of the defect is identified by the black curve.

before the defect position, is observed. It shows that a high level of attenuation can perturb the correct localization of the defect. Removing the attenuation of the leaky mode in the forward and adjoint problems, as proposed for viscoelastic closed waveguides (Sec. 4.4.2.2), enables to recentre the spot on the defect position in the axis direction (Fig. 4.18b). In that case, the modal formalism appears to be very convenient to carry out this operation. However, the position of the defect along the transverse direction of the waveguide cannot be identified with a monomodal wave field, as already found for a closed waveguide.

Second, a multimodal wave field is emitted such that the L(0,1), L(0,2) and L(0,3) modes propagate (see the red region in Fig. 4.17). The images obtained with a single transducer are shown in Fig. 4.19. Despite the attenuation removal in the forward and adjoint problems (Fig. 4.19b), the defect cannot be located even along the axial direction. Numerous spots of great amplitude can be observed before the defect, reminding the artefacts observed previously in Sec. 4.4.2.2. Actually, it has been checked with a modal analysis of the synthetic problem that the behaviours of the source and the defect are different from those in the closed waveguide case. Particularly, modal conversions by the defect are more significant.

The image obtained with 40 transducers is shown in Fig. 4.20. In Fig. 4.20b (after attenuation removal), the amplitude of the artefacts is lower than in Fig. 4.19b and a spot is visible at the interface of the core and the embedding medium, slightly before the defect position. As proposed for closed waveguides (Sec. 4.4.2.1), the image in Fig. 4.20b can be multiplied by the value of the gradient (4.48) obtained with a monomodal wave field, extracted along z for $r = 0$ in the image in Fig. 4.18b. The post-processed image is shown in Fig. 4.20c. The identification of the defect position is acceptable, both along the axial and transverse directions.

4.6 Conclusion

A general framework has been recalled for inverse problems in elastodynamics, including topological imaging. Thanks to numerical methods based on a modal formalism (Chaps. 2 and 3), efficient and fast simulations of topological imaging of waveguides have then been done. In view of practical open waveguides imaging, a restricted measurement configuration (in reflection and at the surface of the waveguide only) has been considered. Promising preliminary results have been obtained.

The various empirical formulations of the gradients have been compared to understand their influence on the quality of the image. These formulations are not truly related to the topology of the defect, but still enables a correct localization of the defect.

The first test in a closed waveguide has shown that a monomodal wave field allows locating a defect along the axis of the waveguide only. The image can be related to the shape of the mode. To obtain a better resolution along the transverse direction of the waveguide, a multimodal field must be emitted. However, artefacts appear in the image. Using several transducers enables to reduce the amplitude of the artefacts, which improves the quality of the image. In addition, we have proposed to combine the images obtained with monomodal and multimodal wave fields, in order to easily reduce the artefacts and then to enhance the quality of multimodal images.

In an open waveguide, the results have shown that a strong leakage attenuation can shift the image out of the defect position. The modal formalism offers an efficient way to remove the attenuation in the forward and adjoint problems, while keeping travelling velocities accurate. It enables to recentre the image towards the defect position.

The results presented in this chapter are a first step towards practical topological imaging of waveguides. Further works are needed. Propositions are made in the conclusion of this manuscript.

Conclusion

In this work, we have developed numerical methods to obtain the forced response and the diffracted wavefield in elastic open waveguides. The first step is to write the PML waveguide formulation of the source-free problem. It yields a linear eigenvalue problem, which solutions are the modes. Modal expansions are then used to solve the forced response problem, and also performed at the boundaries of a finite-element volume enclosing a defect for the diffraction problem (hybrid method). The wavefield can be finally computed analytically at any point of the waveguide. These methods remain valid for viscoelastic materials and for any waveguide geometry.

In addition to dispersion curves, the numerical results of this thesis provide a better understanding of leaky modes behaviour for NDE. The forced response method provides the excitability of leaky modes. Furthermore, the sensitivity of a leaky mode to any type of defect can be assessed with the help of the modal scattering coefficients (at least if mode coupling remains negligible). Solutions can also be obtained at high-frequencies corresponding to the minimum attenuation of leaky modes.

Throughout this thesis, a special attention has been given to the contribution of leaky modes and PML modes to the solutions.

In Chap. 1, we have shown that the modification of the surrounding medium by an infinite PML naturally reveals leaky modes into the modal basis. Trapped modes are left unchanged. Furthermore, two continua of PML modes (*i.e.* radiation modes inside the PML) are defined. With numerical methods, the continua of PML modes are discretized because of the PML truncation to a finite thickness. Two discrete sets of PML modes (non-intrinsic to the physics) are thus included in the numerical modal basis.

As shown in Chap. 2, trapped modes, leaky modes and discrete PML modes are orthogonal. The orthogonality relation actually corresponds to the discrete version of Auld's real biorthogonality relation. It guarantees the uniqueness of modal expansions on the whole cross-section including the PML. However, these modes are not power orthogonal (Chap. 3). Mode coupling can occur and should then be considered for the physical analysis of the results.

Modal expansion with only discrete PML modes (exponentially decaying) enables to reconstruct the bulk wave contribution (geometrically decaying) propagating in a homogeneous medium (Chap. 2). The accuracy of the solution depends on the number of PML modes retained in the expansion and on the PML thickness. The latter must be increased (and so does the computational cost) when the distance to the source increases to get accurate results. Although this case has little interest in practice, it allows clarifying the contribution of PML modes.

Similarly the contribution of discrete PML modes must be retained to observe long-term diffraction phenomenon in open waveguides (Chap. 2). Indeed, long-term diffraction occurs at great distances from the source when most of the energy has leaked from the core into the surrounding medium, such that a geometric decay of the waves (analogous to bulk waves) can be observed. However, the leaky mode contribution dominates the solution in a wide range of distance inside the core and not too far from the source. This region is the most interesting for NDE, which requires that a major part of energy remains in the core. Thereby, leaky modes are expected to be sufficient to obtain a good approximation of the solution for NDE applications based on guided waves (Chap. 2). In the very near-field, PML modes can also have a significant influence on the accuracy of the solutions (Chap. 3). The weight of the PML mode contribution depends on the distance between the cross-section on which the modal expansion is performed and the inhomogeneity.

It is noteworthy that the leaky mode contribution gives a good approximation of the solution in a restricted region of the waveguide. This conclusion is similar to that theoretically found (without PML) when approximating the continua of radiation modes with leaky modes using the steepest descent method (see *e.g.* Refs. [11, 16]). Here, this region of approximation is limited transversely by the PML because the solution is not physically correct inside this artificial layer. Furthermore, this region is limited axially both by the long-term diffraction and by the near-field effect, where PML modes might have a significant contribution.

The leaky mode approximation is particularly important for our numerical methods. Indeed the computation of many PML modes can be very expensive, especially at high frequencies or in three-dimensional waveguides. Neglecting the PML mode contribution generally enables to reduce the thickness of the PML, thus reducing also the computational cost. For the hybrid method, it can be convenient to set the transparent boundaries sufficiently far away from the inhomogeneity. Therefore, in practice, the accuracy of the solutions has to be carefully checked by varying the distance between the modal expansion boundaries and the defect, the number of modes involved in the modal expansions and the PML complex thickness.

The numerical methods have then been used to simulate the topological imaging method applied to waveguides in Chap. 4. The topological imaging method takes place in a constrained optimization framework, restricted to the first iteration only. The key point is the evaluation of the topological gradient, which is used as an imaging function to reveal the position of defects. The gradient depends on two simulations in a reference medium, which gives the forward and adjoint fields. The latter requires a prior measurement of the diffracted field in the real medium, limited in this thesis to the reflected field at the surface of the core. In this study, practical simplified versions of the topological gradient have been used. These formulations of the gradients are not truly connected to the topology of the defect. They can be rather related to variations of density inside the medium. Yet the results show that they are suitable for defect localization in waveguides.

Both closed waveguide and open waveguide imaging have been investigated. The reflected field in a damaged waveguide have been synthesized thanks to the hybrid method presented in Chap. 3. Besides, the forward and adjoint problems have been solved by the method presented in Chap. 2, which enables to obtain quickly both fields at any point of the reference medium.

We have shown that the emission of a monomodal wavefield enables to locate the defect along the axis of the waveguide only. Indeed, in that case, the image is in essence the product of the mode shape by itself. Besides, topological imaging naturally handles modal dispersion, provided that it is accurately computed with the numerical methods.

A multimodal wavefield must be emitted to obtain a better resolution along the cross-section of the waveguide, but it creates artefacts in the image. Artefacts originate from modal conversion by the adjoint source and by the defect. We have shown that the positions of artefacts in the image depend on the distance between the defect and the transducer. Thereby, the relative amplitude of the artefacts in the image can be reduced using several transducers. We have also proposed a simple post-processing method to remove most of the artefacts, based on a mono-dimensional profile extracted from the monomodal image.

In the open waveguide case, the results have shown that a strong modal attenuation (in that case due to radiation losses) can shift the image out of the defect position. In the forward and adjoint fields, losses can be easily cancelled thanks to modal formalism, considering only the real part of the wavenumber in the modal expansions (this gives the correct travelling modal velocities in the lossy medium but without attenuation). This convenient procedure enables to recentre the image on the defect position.

It is noteworthy that in Chaps. 2 and 3, numerical methods are proposed to better understand specific modal behaviours and to facilitate the interpretation of NDE results. On the contrary, the topological imaging method intends to use the whole complexity of guided wave propagation as a black box, provided that accurate models based on known *a priori* data are available. This may lead to a significant improvement of NDE techniques.

Finally, from dispersion curves to topological imaging, this thesis shows that starting from a single eigenvalue problem, numerical methods based on modal formalism can cover a wide variety of problems with a low computational cost.

Future works are proposed hereafter.

Definition of the energy velocity. We have highlighted in Chap. 2 the arbitrariness of the energy velocity definition (integrated on the core of the waveguide only in practice). Indeed, the energy velocity of trapped modes should be integrated on the whole cross-section because they decay in the transverse direction. As a matter of fact, a recent study has also shown that the whole cross-section should be considered for leaky waves of backward type [70]. This interesting physical question thus remains open.

Numerical benchmark. Several others waveguide formulations have been proposed for the computation of trapped and leaky modes (see the introduction of Chap. 2). A numerical benchmark with the PML waveguide formulation would be interesting, considering the computation of dispersion curves. Note that the PML technique and the absorbing layer technique have already been compared in the thesis [9].

Eigenvalue solver. The PML waveguide formulation yields a linear eigenproblem which is solved in this thesis with the ARPACK library [77]. A user-defined number of modes that are the closest in absolute value to a user-defined shift is computed. Instead, for instance, it could be interesting to solve the eigenvalue problem by setting a maximum imaginary part to the eigenvalues (*i.e.* a maximum modal attenuation of interest). The SLEPc library [118] seems to offer this possibility.

Investigation of the PML parameterization. In this thesis, the PML has always a parabolic attenuation profile which does not depend on the frequency. In Ref. [31] a

PML with an exponential attenuation profile has been used to compute the modes and seems more efficient at low frequencies. More generally, the attenuation profile depends on the position, the thickness and the average attenuation of the PML. Finding the correct values of the parameters for a given FE mesh can be difficult, which is a drawback of the method. "Parameter-free" PML have been recently proposed in the literature [119, 120]. However, these PML formulations depend on frequency. Their influence on mode computation should then be investigated. It has been shown in Ref. [121] in scalar acoustics that a frequency dependent PML simplifies the choice of PML parameters and the identification of spurious eigenvalues. However, it leads to a polynomial eigenvalue problem which is difficult to solve with a standard eigensolver.

Application of methods to complex geometries. The proposed numerical methods can be extended to various geometries of waveguides, provided translational invariance is preserved along one direction. For instance, the forced response and the diffraction problems could be solved in the case of helical multi-wire cables, for which a PML waveguide formulation has already been derived [13]. Besides, a series of sources and scatterers could be considered with several combinations of the forced response method and the hybrid method. An example based on scattering matrix formalism can be found in Ref. [122] for closed waveguide. In topological imaging, such models could be used to compute the forward and adjoint fields in complex reference domains, including several *a priori* known scatterers.

Energy balance in open waveguides. The energy balance can be verified with a proper computation on a given volume (to be determined) of input power, output power (including leakage losses), kinetic energy, strain energy and dissipated energy [123]. It could be a convenient tool to assess the accuracy of the solutions computed with the hybrid method.

Topological gradient formulations. Further comparisons of the empirical versions of the gradient are needed, particularly with the theoretical formulation related to the topology of the defect. The derivation of specific empirical formulations for waveguides may also be investigated.

Ideal configuration for topological imaging. The best imaging quality of waveguides is expected to be achieved with a full-scattering measurement configuration, that is in reflection, transmission and in the section of the waveguide. This configuration could be then simplified step by step towards a more realistic one, thus pointing out loss of information and defining the expected efficiency of the method in practice. The sensitivity of the method to noise and to errors on *a priori* data could also be studied. Besides, to improve the resolution of the image in the cross-section, it could be necessary to increase the number of modes, that is to generate higher-order modes having a strong oscillating behaviour along the transverse direction. On this subject, it is noteworthy that the linear sampling method in elastic waveguides gives better results with a lot of modes [102]. It would be of great interest to observe whether the amplitude of artefacts is significantly lowered in that case.

Imaging of open waveguide with a junction. In Chap. 4, the open waveguide case is not truly representative of a practical configuration, in which the diffracted field is generally measured in the protruding part of the waveguide (that is, without embedding medium). In that case, the reference healthy domain should account for the presence of the junction between the closed region and the open region of the waveguide, considered as a known scatterer in order to not appear as a defect in the image.

Experimental tests. The topological imaging method could then be applied experimentally to waveguides. In a first step, an important work of experimental validation is required. For instance, it could be interesting to check the accuracy of the forward field simulation to ensure that the residue (*i.e.* the adjoint source) is mainly the signature of the defects included in the real medium. Thereby, it could provide an experimental validation of the numerical models.

References

[1] R. N. Thurston, Elastic waves in rods and clad rods, *Journal of the Acoustical Society of America* 64 (1978), pp. 1–37, DOI: 10.1121/1.381962.

[2] D. Marcuse, *Theory of Dielectric Optical Waveguides*, ed. by Elsevier, Academic Press, 1991.

[3] P. Malischewsky, *Surface Waves and Discontinuities*, Elsevier, Berlin, 1987.

[4] B. N. Pavlakovic, M. J. S. Lowe, and P. Cawley, High-frequency low-loss ultrasonic modes in imbedded bars, *Journal of Applied Mechanics - Transactions of the ASME* 68 (2001), pp. 67–75, DOI: 10.1115/1.1347995.

[5] V. Maupin, The radiation modes of a vertically varying half-space: a new representation of the complete Green's function in terms of modes, *Geophysical Journal International* 126 (1996), pp. 762–780, DOI: 10.1111/j.1365-246X.1996.tb04701.x.

[6] A. C. Hladky-Hennion, P. Langlet, and M. de Billy, Conical radiating waves from immersed wedges, *Journal of the Acoustical Society of America* 108 (2000), pp. 3079–3083, DOI: 10.1121/1.1322569.

[7] T. Vogt, M. Lowe, and P. Cawley, The scattering of guided waves in partly embedded cylindrical structures, *Journal of the Acoustical Society of America* 113 (2003), pp. 1258–1272, DOI: 10.1121/1.1553463.

[8] B. Goursaud, Mathematical and numerical study of non uniform open waveguides, modal approach, PhD Thesis, Ecole Polytechnique X, 2010.

[9] K. L. Nguyen, Modélisation numérique de la propagation des ondes élastiques dans les guides enfouis, PhD thesis, Ecole Centrale de Nantes, 2014.

[10] R. E. Collin, *Field theory of guided waves*, IEEE Press, Wiley, 1991.

[11] T. Tamir and A. A. Oliner, Guided complex waves. Part 1: Fields at an interface, *Proceedings of the Institution of Electrical Engineers* 110 (1963), pp. 310–324, DOI: 10.1049/piee.1963.0044.

[12] F. Treyssède, K. L. Nguyen, A.-S. Bonnet-BenDhia, and C. Hazard, Finite element computation of trapped and leaky elastic waves in open stratified waveguides, *Wave Motion* 51 (2014), pp. 1093–1107, DOI: 10.1016/j.wavemoti.2014.05.003.

[13] K. L. Nguyen and F. Treyssede, Numerical investigation of leaky modes in helical structural waveguides embedded into a solid medium, *Ultrasonics* 57 (2015), pp. 125–134, DOI: 10.1016/j.ultras.2014.11.002.

[14] K. Aki and P. G. Richards, *Quantitative Seismology, Theory and Methods*, ed. by Freeman, vol. 1, 1980.

[15] F. Olyslager, Discretization of Continuous Spectra Based on Perfectly Matched Layers, *SIAM Journal on Applied Mathematics* 64 (2004), pp. 1408–1433, DOI: 10.1137/S0036139903430197.

[16] J. Hu and C. R. Menyuk, Understanding leaky modes: slab waveguide revisited, *Advances in Optics and Photonics* 1 (2009), pp. 58–106, DOI: 10.1364/AOP.1.000058.

[17] B. N. Pavlakovic, Leaky Guided Ultrasonic Waves in NDT, PhD thesis, University of London - Imperial College of Science, Technology and Medicine, 1998.

[18] V. Baronian, A. S. Bonnet-Ben Dhia, and E. Luneville, Transparent boundary conditions for the harmonic diffraction problem in an elastic waveguide, *Journal of Computational and Applied Mathematics* 234 (2010), 8th International Conference on Mathematical and Numerical Aspects of Waves, Univ Reading, Reading, England, JUL 23-27, 2007, pp. 1945–1952, DOI: 10.1016/j.cam.2009.08.045.

[19] F. Benmeddour, F. Treyssède, and L. Laguerre, Numerical modeling of guided wave interaction with non-axisymmetric cracks in elastic cylinders, *International Journal of Solid and Structures* 48 (2011), pp. 764–774, DOI: 10.1016/j.ijsolstr.2010.11.013.

[20] N. Dominguez, V. Gibiat, and Y. Esquerre, Time domain topological gradient and time reversal analogy: an inverse method for ultrasonic target detection, *Wave Motion* 42 (2005), pp. 31–52, DOI: 10.1016/j.wavemoti.2004.09.005.

[21] M. Bonnet, Topological sensitivity for 3D elastodynamic and acoustic inverse scattering in the time domain, *Computer Methods in Applied Mechanics and Engineering* 195 (2006), pp. 5239–5254, DOI: 10.1016/j.cma.2005.10.026.

[22] S. Rodriguez, M. Deschamps, M. Castaings, and E. Ducasse, Guided wave topological imaging of isotropic plates, *Ultrasonics* 54 (2014), 1880–1890, DOI: 10.1016/j.ultras.2013.10.001.

[23] S. Rodriguez, P. Sahuguet, V. Gibiat, and X. Jacob, Fast topological imaging, *Ultrasonics* 52 (2012), pp. 1010–1018, DOI: 10.1016/j.ultras.2012.08.002.

[24] P. D. Wilcox, M. J. S. Lowe, and P. Cawley, Mode and transducer selection for long range lamb wave inspection, *Journal of Intelligent Materiel System and Structures* 12 (2001), pp. 553–565.

[25] W. T. Thomson, Transmission of elastic waves through a stratified solid medium, *Journal of applied Physics* 21 (1950), pp. 89–93.

[26] N. A. Haskell, The dispersion of surface waves on multilayered media, *Bulletin of the Seismological Society of America* 43 (1953), pp. 17–34.

[27] E. Kausel and J. M. Roësset, Stiffness matrices for layered soils, *Bulletin of the Seismological Society of America* 71 (1981), pp. 1743–1761.

[28] B. Pavlakovic, M. Lowe, D. Alleyne, and P. Cawley, Disperse: A General Purpose Program for Creating Dispersion Curves, in: *Review of Progress in Quantitative Nondestructive Evaluation: Volume 16A*, ed. by D. O. Thompson and D. E. Chimenti, Boston, MA: Springer US, 1997, pp. 185–192, DOI: 10.1007/978-1-4615-5947-4_24.

[29] A. Marzani, E. Viola., I. Bartoli, F. L. di Scalea, and P. Rizzo, A semi-analytical finite element formulation for modeling stress wave propagation in axisymmetric damped waveguides, *Journal of Sound and Vibration* 318 (2008), pp. 488–505, DOI: 10.1016/j.jsv.2008.04.028.

[30] V. Damljanovic and R. L. Weaver, Forced response of a cylindrical waveguide with simulation of the wavenumber extraction problem, *Journal of the Acoustical Society of America* 115 (2004), pp. 1582–1591, DOI: 10.1121/1.1675818.

[31] W. Duan, R. Kirby, P. Mudge, and T.-H. Gan, A one dimensional numerical approach for computing the eigenmodes of elastic waves in buried pipelines, *Journal of Sound and Vibration* 384 (2016), pp. 177–193, DOI: 10.1016/j.jsv.2016.08.013.

[32] F. Treyssède, Spectral element computation of high-frequency leaky modes in three-dimensional solid waveguides, *Journal of Computational Physics* 314 (2016), pp. 341–354, DOI: 10.1016/j.jcp.2016.03.029.

[33] K. L. Nguyen, F. Treyssède, and C. Hazard, Numerical modeling of three-dimensional open elastic waveguides combining semi-analytical finite element and perfectly matched layer methods, *Journal of Sound and Vibration* 344 (2015), pp. 158–178, DOI: 10.1016/j.jsv.2014.12.032.

[34] P. Zuo and Z. Fan, SAFE-PML approach for modal study of waveguides with arbitrary cross sections immersed in inviscid fluid, *Journal of Sound and Vibration* 406 (2017), pp. 181–196.

[35] M. Mazzotti, I. Bartoli, A. Marzani, and E. Viola, A coupled SAFE-2.5D BEM approach for the dispersion analysis of damped leaky guided waves in embedded waveguides of arbitrary cross-section, *Ultrasonics* 53 (2013), pp. 1227–1241, DOI: 10.1016/j.ultras.2013.03.003.

[36] H. Gravenkamp, C. Birk, and C. Song, Numerical modeling of elastic waveguides coupled to infinite fluid media using exact boundary conditions, *Computers & Structures* 141 (2014), pp. 36–45, DOI: 10.1016/j.compstruc.2014.05.010.

[37] M. Castaings and M. Lowe, Finite element model for waves guided along solid systems of arbitrary section coupled to infinite solid media, *Journal of the Acoustical Society of America* 123 (2008), pp. 696–708, DOI: 10.1121/1.2821973.

[38] A. Marzani, Time-transient analysis response for Ultrasonic Guided waves propagating in damped cylinders, *International Journal of Solid and Structures* 45 (2008), pp. 6347–6368, DOI: 10.1016/j.ijsolstr.2008.07.028.

[39] F. Treyssède, Mode propagation in curved waveguides and scattering by inhomogeneities: Application to the elastodynamics of helical structures, *Journal of the Acoustical Society of America* 129 (2011), pp. 1857–1868, DOI: 10.1121/1.3559682.

[40] B. A. Auld, *Acoustic fields and waves in solids*, vol. 2, A Wiley-Interscience publication, 1973.

[41] M. Gallezot, F. Treyssède, and L. Laguerre, Contribution of leaky modes in the modal analysis of unbounded problems with perfectly matched layers, *Journal of the Acoustical Society of America* 141 (2017), EL16–EL21, DOI: 10.1121/1.4973313.

[42] M. Gallezot, F. Treyssède, and L. Laguerre, A numerical method for the scattering by defects in axisymmetrical open elastic waveguides, *Procedia Engineering* 199 (2017), pp. 1527–1532.

[43] M. Gallezot, F. Treyssède, and L. Laguerre, A modal approach based on perfectly matched layers for the forced response of elastic open waveguides, *Journal of Computational Physics* 356 (2018), pp. 391–409, DOI: 10.1016/j.jcp.2017.12.017.

[44] M. Gallezot, F. Treyssède, and L. Laguerre, Numerical modelling of wave scattering by local inhomogeneities in elastic waveguides embedded into infinite media, *Journal of Sound and Vibration* (2018), DOI: 10.1016/j.jsv.2018.11.044.

[45] M. Gallezot, L. Laguerre, and F. Treyssede, *Excitation d'un guide d'onde 2D enfoui*, 2016, DOI: 10.25578/SZAE-ED71.

[46] M. Gallezot, L. Laguerre, and F. Treyssede, *Excitation d'un guide d'onde 2D enfoui avec PML*, 2016, DOI: 10.25578/17AE-YZ30.

[47] S. Kim and J. E. Pasciak, The computation of resonances in open systems using a perfectly matched layer, *Mathematics of Computation* 78 (2009), pp. 1375–1398.

[48] H. Derudder, F. Olyslager, D. D. Zutter, and S. V. den Berghe, Efficient mode-matching analysis of discontinuities in finite planar substrates using perfectly

matched layers, *IEEE Transactions on Antennas and Propagation* 49 (2001), pp. 185–195, DOI: 10.1109/8.914270.

[49] W. C. Chew and W. H. Weedon, A 3D perfectly matched medium from modified Maxwells equations with stretched coordinates, *Microwave and Optical Technology Letters* 7 (1994), pp. 599–604, DOI: 10.1002/mop.4650071304.

[50] A. Kurkjian, Numerical computation of individual far-field arrivals excited by an acoustic source in a borehole, *Geophysics* 50 (1985), pp. 852–866, DOI: 10.1190/1.1441961.

[51] E. Becache, S. Fauqueux, and P. Joly, Stability of perfectly matched layers, group velocities and anisotropic waves, *Journal of Computational Physics* 188 (2003), pp. 399–433, DOI: 10.1016/S0021-9991(03)00184-0.

[52] R. Nelson, S. Dong, and R. Kalra, Vibrations and waves in laminated orthotropic circular cylinders, *Journal of Sound and Vibration* 18 (1971), pp. 429–444.

[53] B. Aalami, Waves in prismatic guides of arbitrary cross section, *Journal of Applied Mechanics* 40 (1973), pp. 1067–1072.

[54] E. Kausel, *An explicit solution for the Green functions for dynamic loads in layered media*, MIT Research Report R81-13, Department of Civil Engineering, School of Engineering, Massachusetts Institute of Technology, 1981.

[55] J. Park, Wave motion in finite and infinite media using the thin-layer method, PhD thesis, Massachusetts Institute of Technology, 2002.

[56] G. Liu and J. Achenbach, Strip element method to analyze wave scattering by cracks in anisotropic laminated plates, *Journal of Applied Mechanics-Transactions of the ASME* 62 (1995), pp. 607–613, DOI: 10.1115/1.2895989.

[57] H. Gravenkamp, C. Song, and J. Prager, A numerical approach for the computation of dispersion relations for plate structures using the Scaled Boundary Finite Element Method, *Journal of Sound and Vibration* 331 (2012), pp. 2543–2557, DOI: 10.1016/j.jsv.2012.01.029.

[58] H. Gravenkamp, H. Man, C. Song, and J. Prager, The computation of dispersion relations for three-dimensional elastic waveguides using the scaled boundary finite element method, *Journal of Sound and Vibration* 332 (2013), pp. 3756–3771.

[59] M. Mazzotti, I. Bartoli, and A. Marzani, Ultrasonic leaky guided waves in fluid-coupled generic waveguides: hybrid finite-boundary element dispersion analysis and experimental validation, *Journal of Applied Physics* 115 (2014), p. 143512.

[60] M. Mazzotti, A. Marzani, and I. Bartoli, Dispersion analysis of leaky guided waves in fluid-loaded waveguides of generic shape, *Ultrasonics* 54 (2014), pp. 408–418, DOI: 10.1016/j.ultras.2013.06.011.

[61] T. Hayashi and D. Inoue, Calculation of leaky Lamb waves with a semi-analytical finite element method, *Ultrasonics* 54 (2014), pp. 1460–1469, DOI: 10.1016/j.ultras.2014.04.021.

[62] D. Inoue and T. Hayashi, Transient analysis of leaky Lamb waves with a semi-analytical finite element method, *Ultrasonics* 62 (2015), pp. 80–88, DOI: 10.1016/j.ultras.2015.05.004.

[63] H. Gravenkamp, C. Birk, and C. Song, Computation of dispersion curves for embedded waveguides using a dashpot boundary condition, *Journal of the Acoustical Society of America* 135 (2014), pp. 1127–1138, DOI: 10.1121/1.4864303.

[64] A. C. Hladky-Hennion, P. Langlet, R. Bossut, and M. De Billy, Finite element modelling of radiating waves in immersed wedges, *Journal of Sound and Vibration* 212 (1998), pp. 265–274, DOI: 10.1006/jsvi.1997.1408.

[65] A. V. Astaneh and M. N. Guddati, Dispersion analysis of composite acousto-elastic waveguides, *Composites Part B: Engineering* 130 (2017), pp. 200–216.

[66] E. Kausel, Physical interpretation and stability of paraxial boundary conditions, *Bulletin of the Seismological Society of America* 82 (1992), pp. 898–913.

[67] Z. Fan, M. J. S. Lowe, M. Castaings, and C. Bacon, Torsional waves propagation along a waveguide of arbitrary cross section immersed in a perfect fluid, *Journal of the Acoustical Societe of America* 124 (2008), pp. 2002–2010, DOI: 10.1121/1.2968677.

[68] P. Zuo, X. Yu, and Z. Fan, Numerical modeling of embedded solid waveguides using SAFE-PML approach using a commercially available finite element package, *NDT & E International* 90 (2017), pp. 11–23, DOI: 10.1016/j.ndteint.2017.04.003.

[69] J. M. de Oliveira Barbosa, J. Park, and E. Kausel, Perfectly matched layers in the thin layer method, *Computer methods in applied mechanics and engineering* 217 (2012), pp. 262–274.

[70] I. Nedospasov, V. Mozhaev, and I. Kuznetsova, Unusual energy properties of leaky backward Lamb waves in a submerged plate, *Ultrasonics* 77 (2017), pp. 95–99, DOI: 10.1016/j.ultras.2017.01.025.

[71] L. Margerin, Generalized eigenfunctions of layered elastic media and application to diffuse fields, *Journal of the Acoustical Society of America* 125 (2009), pp. 164–174, DOI: 10.1121/1.3021312.

[72] R. Sammut and A. W. Snyder, Leaky modes on a dielectric waveguide: orthogonality and excitation; erratum, *Applied Optics* 15 (1976), pp. 2953–2953, DOI: 10.1364/AO.15.002953.

[73] S.-L. Lee, Y. Chung, L. A. Coldren, and N. Dagli, On leaky mode approximations for modal expansion in multilayer open waveguides, *IEEE Journal of Quantum Electronics* 31 (1995), pp. 1790–1802, DOI: 10.1109/3.466054.

[74] F. Tisseur and K. Meerbergen, The quadratic eigenvalue problem, *SIAM Review* 43 (2001), pp. 235–286.

[75] F. Treyssède and L. Laguerre, Numerical and analytical calculation of modal excitability for elastic wave generation in lossy waveguides, *Journal of the Acoustical Society of America* 133 (2013), pp. 3287–3837.

[76] A. Bernard, M. J. S. Lowe, and M. Deschamps, Guided waves energy velocity in absorbing and non-absorbing plates, *Journal of the Acoustical Society of America* 110 (2001), pp. 186–196, DOI: 10.1121/1.1375845.

[77] R. B. Lehoucq, D. C. Sorensen, and C. Yang, *ARPACK users' guide: solution of large-scale eigenvalue problems with implicitly restarted Arnoldi methods*, vol. 6, Siam, 1998.

[78] P. D. Wilcox, M. Lowe, and P. Cawley, The effect of dispersion on long-range inspection using ultrasonic guided waves, *NDT & E International* 34 (2001), pp. 1–9, DOI: 10.1016/S0963-8695(00)00024-4.

[79] L. Laguerre and F. Treyssede, Non destructive evaluation of seven-wire strands using ultrasonic guided waves, *European Journal of Environmental and Civil Engineering* 15 (2011), pp. 487–500, DOI: 10.1080/19648189.2011.9693342.

[80] M. Beard, M. J. S. Lowe., and P. Cawley, Ultrasonic Guided Waves for Inspection of Grouted Tendons and Bolts, *Journal of Materials in Civil Engineering* 15 (2003), pp. 212–218, DOI: 10.1061/(ASCE)0899-1561(2003)15:3(212).

[81] M. D. Beard and M. J. S. Lowe, Non-destructive testing of rock bolts using guided ultrasonic waves, *International Journal of Rock Mechanics and Mining Sciences* 40 (2003), pp. 527–536, DOI: 10.1016/S1365-1609(03)00027-3.

[82] E. Leinov, M. J. S. Lowe, and P. Cawley, Investigation of guided wave propagation in pipes fully and partially embedded in concrete, *Journal of the Acoustical Society of America* 140 (2016), pp. 4528–4539, DOI: 10.1121/1.4972118.

[83] W. Duan, X. Niu, T.-H. Gan, J. Kanfoud, and H.-P. Chen, A Numerical Study on the Excitation of Guided Waves in Rectangular Plates Using Multiple Point Sources, *Metals* 7 (2017), p. 552.

[84] Y. Cho and J. Rose, A boundary element solution for a mode conversion study on the edge reflection of Lamb waves, *Journal of the Acoustical Society of America* 99 (1996), pp. 2097–2109, DOI: 10.1121/1.415396.

[85] N. Rattanawangcharoen, W. Zhuang, A. Shah, and S. Datta, Axisymmetric guided waves in jointed laminated cylinders, *Journal of Engineering Mechanics-ASCE* 123 (1997), pp. 1020–1026, DOI: 10.1061/(ASCE)0733-9399(1997)123:10(1020).

[86] J. Galan and R Abascal, Numerical simulation of Lamb wave scattering in semi-infinite plates, *International Journal for Numerical Methods in Engineering* 53 (2002), pp. 1145–1173, DOI: 10.1002/nme.331.

[87] A.-S. B.-B. Dhia, C. Chambeyron, and G. Legendre, On the use of perfectly matched layers in the presence of long or backward propagating guided elastic waves, *Wave Motion* 51 (2014), pp. 266–283.

[88] M. V. Predoi, M. Castaings, and L. Moreau, Influence of material viscoelasticity on the scattering of guided waves by defects, *Journal of the Acoustical Society of America* 124 (2008), pp. 2883–2894, DOI: 10.1121/1.2977604.

[89] B. Hosten, L. Moreau, and M. Castaings, Reflection and transmission coefficients for guided waves reflected by defects in viscoelastic material plates, *Journal of the Acoustical Societe of America* 121 (2007), pp. 3409–3417, DOI: 10.1121/1.2723652.

[90] A. Gunawan and S. Hirose, Mode-exciting method for lamb wave-scattering analysis, *Journal of the Acoustical Society of America* 115 (2004), pp. 996–1005, DOI: 10.1121/1.1639330.

[91] A. W. Snyder, Coupled-Mode Theory for Optical Fibers, *Journal of the Optical Society of America* 62 (1972), pp. 1267–1277, DOI: 10.1364/JOSA.62.001267.

[92] D. F. Williams and F. Olyslager, Modal cross power in quasi-TEM transmission lines, *IEEE Microwave and Guided Wave Letters* 6 (1996), pp. 413–415, DOI: 10.1109/75.541457.

[93] M. D. Beard, M. J. S. Lowe, and P. Cawley, Inspection of steel tendons in concrete using guided waves, in: *AIP Conference Proceedings*, vol. 657, 1, AIP, 2003, pp. 1139–1147.

[94] C. W. Chan and P. Cawley, Lamb waves in highly attenuative plastic plates, *The Journal of the Acoustical Society of America* 104 (1998), pp. 874–881, DOI: 10.1121/1.423332.

[95] E. Manconi and S. Sorokin, On the effect of damping on dispersion curves in plates, *International Journal of Solids and Structures* 50 (2013), pp. 1966–1973, DOI: 10.1016/j.ijsolstr.2013.02.016.

[96] E. Le Clézio, M. Castaings, and B. Hosten, The interaction of the S0 Lamb mode with vertical cracks in an aluminum plate, *Ultrasonics* 40 (2002), pp. 187–192.

[97] N. Bleistein, *Mathematical methods for wave phenomena.* Ed. by Elsevier, Academic Press, 1984, DOI: 10.1016/C2009-0-21864-2.

[98] D. Colton and R. Kress, *Inverse acoustic and electromagnetic scattering theory*, vol. 93, Springer Science & Business Media, 2012.

[99] C. Bellis, Qualitative Methods for Inverse Scattering in Solid Mechanics, PhD thesis, Ecole Polytechnique X, 2010.

[100] F. Cakoni and D. Colton, *Qualitative methods in inverse scattering theory. An Introduction.* 1st ed., Interaction of Mechanics and Mathematics, Springer-Verlag Berlin Heidelberg, 2006, DOI: 10.1007/3-540-31230-7.

[101] D. Colton and A. Kirsch, A simple method for solving inverse scattering problems in the resonance region, *Inverse Problems* 12 (1996), pp. 383–393, DOI: 10.1088/0266-5611/12/4/003.

[102] A. Recoquillay, Méthodes d'échantillonnage appliquées à l'imagerie de défauts dans un guide d'ondes élastiques, PhD thesis, Paris Saclay, 2018.

[103] H. A. Eschenauer, V. Kobelev, and A. Schumacher, Bubble method for topology and shape optimization of structures, *Structural Optimization* 8 (1994), pp. 42–51, DOI: 10.1007/BF01742933.

[104] S. Garreau, P. Guillaume, and M. Masmoudi, The topological asymptotic for PDE systems: The elasticity case, *Siam Journal on Control and Optimisation* 39 (2001), pp. 1756–1778.

[105] B. B. Guzina and M. Bonnet, Topological derivative for the inverse scattering of elastic waves, *The Quarterly Journal of Mechanics and Applied Mathematics* 57 (2004), p. 161, DOI: 10.1093/qjmam/57.2.161.

[106] R. Tokmashev, A. Tixier, and B. B. Guzina, Experimental validation of the topological sensitivity approach to elastic-wave imaging, *Inverse Problems* 29 (2013), DOI: 10.1088/0266-5611/29/12/125005.

[107] G. R. Feijoo, A new method in inverse scattering based on the topological derivative, *Inverse Problems* 20 (2004), p. 1819.

[108] V. Gibiat and P. Sahuguet, Wave guide imaging through Time Domain Topological Energy, *Ultrasonics* 50 (2010), Selected Papers from ICU 2009, pp. 172–179, DOI: 10.1016/j.ultras.2009.09.029.

[109] R. E. Plessix, A review of the adjoint-state method for computing the gradient of a functional with geophysical applications, *Geophysical Journal International* 167 (2006), pp. 495–503, DOI: 10.1111/j.1365-246X.2006.02978.x.

[110] G. Chavent, *Nonlinear least squares for inverse problems: theoretical foundations and step-by-step guide for applications*, Springer Science & Business Media, 2010.

[111] P. G. Ciarlet, *Introduction à l'analyse numérique matricielle et à l'optimisation*, ed. by Dunod, 5th ed., 2007.

[112] M. Bonnet and B. Guzina, Sounding of finite solid bodies by way of topological derivative, *International Journal for Numerical Methods in Engineering* 61 (2004), pp. 2344–2373, DOI: 10.1002/nme.1153.

[113] J. Tromp, C. Tape, and Q. Y. Liu, *Seismic tomography, adjoint methods, time reversal and banana-doughnut kernels*, 2005, DOI: 10.1111/j.1365-246X.2004.02453.x.

[114] C. Bellis, M. Bonnet, and F. Cakoni, Acoustic inverse scattering using topological derivative of far-field measurements-based L-2 cost functionals, *Inverse Problems* 29 (2013), p. 075012, DOI: 10.1088/0266-5611/29/7/075012.

[115] B. B. Guzina and F. Pourahmadian, *Proceedings of the Royal Society A-Mathematical Physical and Engineering Sciences* 471 (2015), p. 20150187, DOI: 10.1098/rspa.2015.0187.

[116] C. Draeger, D. Cassereau, and M. Fink, Theory of the time-reversal process in solids, *Journal of the Acoustical Society of America* 102 (1997), pp. 1289–1295, DOI: 10.1121/1.420094.

[117] H. W. Park, S. B. Kim, and H. Sohn, Understanding a time reversal process in Lamb wave propagation, *Wave Motion* 46 (2009), pp. 451–467, DOI: 10.1016/j.wavemoti.2009.04.004.

[118] J. E. Roman, C. Campos, E. Romero, and A. Tomas, *SLEPc Users Manual*, tech. rep., Universitat Politecnica de Valencia, 2018, DOI: http://slepc.upv.es.

[119] A. Bermudez, L. Hervella-Nieto, A. Prieto, and R. Rodriguez, An optimal perfectly matched layer with unbounded absorbing function for time-harmonic acoustic scattering problems, *Journal of Computational Physics* (2007).

[120] R. Cimpeanu, A. Martinsson, and M. Heil, A parameter-free perfectly matched layer formulation for the finite-element-based solution of the Helmholtz equation, *Journal of Computational Physics* 296 (2015), pp. 329–347, DOI: 10.1016/j.jcp.2015.05.006.

[121] L. Nannen and M. Wess, Computing scattering resonances using perfectly matched layers with frequency dependent scaling functions, *BIT Numerical Mathematics* (2018), pp. 1–23.

[122] V. Baronian, A. Lhemery, and K. Jezzine, Hybrid SAFE/FE simulation of inspections of elastic waveguides containing several local discontinuities or defects, in: *Review of progress in quantitative nondestructive evaluation, Vols 30A and 30B*, ed. by D. Thompson and D. Chimenti, vol. 1335, AIP Conference Proceedings, 37th Annual Review of Progress in Quantitative Nondestructive Evaluation (QNDE), San Diego, CA, Jul. 18-23, 2010, 2011, pp. 183–190, DOI: 10.1063/1.3591855.

[123] J. M. Carcione and F. Cavallini, Energy-balance and fundamental relations in anitropic-viscoelastic media, *Wave Motion* 18 (1993), pp. 11–20, DOI: 10.1016/0165-2125(93)90057-M.

UNIVERSITE
BRETAGNE SCIENCES
LOIRE POUR L'INGENIEUR

CENTRALE
NANTES

Titre : Simulation numérique du contrôle non-destructif des guides d'ondes enfouis

Mots clés : guide ouvert, élément fini, couche parfaitement adaptée, contrôle non-destructif, modes à fuite, réponse forcée, diffraction, imagerie

Résumé : De nombreux éléments de structures de génie civil sont élancés et partiellement enfouis dans un milieu solide. Les ondes guidées sont souvent utilisées pour le contrôle non destructif (CND) de ces éléments. Ces derniers sont alors considérés comme des guides d'ondes ouverts, dans lesquels la plupart des ondes sont atténuées par des fuites dans le milieu environnant. D'autre part le problème est non borné, ce qui le rend difficile à appréhender sur le plan numérique. La combinaison d'une approche par éléments finis semi-analytique (SAFE) et de la méthode des couches parfaitement adaptées (PML) a été utilisée dans une thèse antérieure pour calculer numériquement trois types de modes (modes piégés, modes à fuite et modes de PML). Seuls les modes piégés et à fuite sont utilisés pour la représentation des courbes de dispersion. Les modes de PML sont non intrinsèques à la physique. L'objectif premier de cette thèse est d'obtenir, par superposition modale sur les modes calculés, les champs émis et diffracté dans les guides d'ondes ouverts. Nous montrons dans un premier temps que les trois types de modes appartiennent à la base modale. Une relation d'orthogonalité est obtenue dans la section du guide (incluant la PML) pour garantir l'unicité des solutions. La réponse forcée du guide peut alors être calculée rapidement par une somme sur les modes en tout point du guide. Des superpositions modales sont également utilisées pour construire des frontières transparentes au bord d'un petit domaine élément fini incluant un défaut, permettant ainsi de calculer le champ diffracté. Au cours de ces travaux, nous étudions les conditions d'approximation des solutions par des superpositions modales, limitées seulement aux modes à fuite, ce qui permet de réduire le coût des calculs. De plus, la généralité des méthodes proposées est démontrée par des calculs hautes fréquences (intéressantes pour le CND) et sur des guides tridimensionnels. Le deuxième objectif de cette thèse est de proposer une méthode d'imagerie pour la localisation de défauts. La méthode de l'imagerie topologique est appliquée aux guides d'ondes. Le cadre théorique général, de type optimisation sous contrainte, est rappelé. Le formalisme modal permet un calcul rapide de l'image. Nous l'appliquons pour simuler un guide d'onde endommagé, et nous montrons l'influence du type de champ émis (monomodal, dispersif, multimodal) ainsi que des configurations de mesure sur la qualité de l'image obtenue.

Title : Numerical modelling of non-destructive testing of buried waveguides

Keywords : open waveguide, finite element, perfectly matched layer, non-destructive evaluation, leaky mode, forced response, diffraction, imaging

Abstract : Various elements of civil engineering structures are elongated and partially embedded in a solid medium. Guided waves can be used for the non-destructive evaluation (NDE) of such elements. The latter is therefore considered as an open waveguide, in which most of waves are attenuated by leakage losses into the surrounding medium. Furthermore, the problem is difficult to solve numerically because of its unboundedness. In a previous thesis, it has been shown that the semi-analytical finite-element method (SAFE) and perfectly matched layers (PML) can be coupled for the numerical computation of modes. It yields three types of modes: trapped modes, leaky modes and PML modes. Only trapped and leaky modes are useful for the post-processing of dispersion curves. PML modes are non-intrinsic to the physics. The major aim of this thesis is to obtain the propagated and diffracted fields, based on modal superpositions on the numerical modes. First, we show that the three types of modes belong to the modal basis. To guarantee the uniqueness of the solutions an orthogonality relationship is derived on the section including the PML. The forced response can then be obtained very efficiently with a modal expansion at any point of the waveguide. Modal expansions are also used to build transparent boundaries at the cross-sections of a small finite-element domain enclosing a defect, thereby yielding the diffracted field. Throughout this work, we study whether solutions can be obtained with modal expansions on leaky modes only, which enables to reduce the computational cost. Besides, solutions are obtained at high frequencies (which are of interest for NDE) and in tridimensional waveguides, which demonstrates the generality of the methods. The second objective of this thesis is to propose an imaging method to locate defects. The topological imaging method is applied to a waveguide configuration. The general theoretical framework is recalled, based on constrained optimization theory. The image can be quickly computed thanks to the modal formalism. The case of a damaged waveguide is then simulated to assess the influence on image quality of the emitted field characteristics (monomodal, dispersive or multimodal) and of the measurement configuration.